INFORMATION TO USERS

This manuscript has been reproduced from the microfilm master. UMI films the text directly from the original or copy submitted. Thus, some thesis and dissertation copies are in typewriter face, while others may be from any type of computer printer.

The quality of this reproduction is dependent upon the quality of the copy submitted. Broken or indistinct print, colored or poor quality illustrations and photographs, print bleedthrough, substandard margins, and improper alignment can adversely affect reproduction.

In the unlikely event that the author did not send UMI a complete manuscript and there are missing pages, these will be noted. Also, if unauthorized copyright material had to be removed, a note will indicate the deletion.

Oversize materials (e.g., maps, drawings, charts) are reproduced by sectioning the original, beginning at the upper left-hand corner and continuing from left to right in equal sections with small overlaps.

Photographs included in the original manuscript have been reproduced xerographically in this copy. Higher quality 6" x 9" black and white photographic prints are available for any photographs or illustrations appearing in this copy for an additional charge. Contact UMI directly to order.

Bell & Howell Information and Learning
300 North Zeeb Road, Ann Arbor, MI 48106-1346 USA
800-521-0600

UMI®

Reproduced with permission of the copyright owner. Further reproduction prohibited without permission.

Reproduced with permission of the copyright owner. Further reproduction prohibited without permission.

Development of Wide Bandgap II-VI Materials for Visible Lasers and Light Emitting Diodes

a) Bipolar doping and electroluminescence of ZnMgCdSe Structures

b) Hexagonal ZnSe-based structures

By

Wei-Cheng Lin

A dissertation submitted to the Graduate Faculty in Physics in partial fulfillment of the requirements for the degree of Doctor of Philosophy, The City University of New York

2000

Reproduced with permission of the copyright owner. Further reproduction prohibited without permission.

UMI Number: 9959201

Copyright 2000 by
Lin, Wei-Cheng Wilson

All rights reserved.

UMI®

UMI Microform 9959201

Copyright 2000 by Bell & Howell Information and Learning Company.
All rights reserved. This microform edition is protected against
unauthorized copying under Title 17, United States Code.

Bell & Howell Information and Learning Company
300 North Zeeb Road
P.O. Box 1346
Ann Arbor, MI 48106-1346

Reproduced with permission of the copyright owner. Further reproduction prohibited without permission.

© 2000

Wei-Cheng Lin

All Rights Reserved

Reproduced with permission of the copyright owner. Further reproduction prohibited without permission.

This manuscript has been read and accepted for the Graduate Faculty in Physics in satisfaction of the dissertation requirement for the degree of Doctor of Philosophy.

1/12/00
Date

Chair of Examining Committee

1/18/00
Date

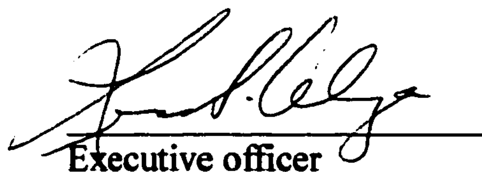
Executive officer

Prof. Y. C. Chen
Dr. B. J. Fitzpatrick
Prof. F. H. Pollak
Prof. F. W. Smith

Supervisory Committee

The City University of New York

Reproduced with permission of the copyright owner. Further reproduction prohibited without permission.

Abstract

Development of Wide Bandgap II-VI Materials

for Visible Lasers and LEDs:

a) Bipolar doping and electroluminescence of ZnMgCdSe structures

b) Hexagonal ZnSe-based structures

By

Wei-Cheng Lin

Adviser: Professor Maria C. Tamargo

Wide bandgap $Zn_{1-x-y}Mg_xCd_ySe$ system grown on InP substrates has potential for making visible light emitting devices. Bipolar doping of $Zn_{1-x-y}Mg_xCd_ySe$ (cladding and waveguide layers) and growth of lattice-matched p-type contact layer ($ZnSe_{0.53}Te_{0.47}$) are essential. The n-type doping of $Zn_{1-x-y}Mg_xCd_ySe$ has been achieved by using chlorine with the maximum free electron concentrations in the range of 10^{18} cm^{-3} and mobilities of about 300 cm^2/Vs. p-type doping of $Zn_{1-x-y}Mg_xCd_ySe$ has been performed using a

Reproduced with permission of the copyright owner. Further reproduction prohibited without permission.

radio frequency (rf) discharge N plasma source. The net acceptor (N_A-N_D) level is currently limited to 1 x 10^{16} cm^{-3}. p-type doping of ZnSe, $Zn_{1-x}Mg_xSe$ and $Zn_{1-y}Cd_ySe$ was studied separately. The results suggest that Mg and Cd both hinder the p-type doping of $Zn_{1-x-y}Mg_xCd_ySe$. Delta (δ)-doping techniques are applied to enhance the p-type doping level of ZnSe. In particular, by using a novel triple (N+Te)δ-doping, the (N_A-N_D) level is dramatically increased from 3 x 10^{17} to 6 x 10^{18} cm^{-3}. Based on these results, we propose a way to increase the p-type doping of the quaternary involving modulation doping.

MBE growth of high quality $ZnSe_{1-x}Te_x$ alloys and their nitrogen doping were studied as a function of Te concentration. In particular, N doped $ZnSe_{0.53}Te_{0.47}$ lattice-matched to InP substrates can have a free hole concentration as high as 2 x 10^{19} cm^{-3}. The I-V characteristics between two Au contacts on the highly N doped $ZnSe_{0.53}Te_{0.47}$ layer show ohmic behavior. This demonstrates that the $ZnSe_{0.53}Te_{0.47}$ layer can be used as an ideal p-type ohmic contact layer for the ZnCdSe/ZnMgCdSe QW lasers and LEDs. Full-color LEDs have been fabricated by combining these accomplishments.

MBE growth of ZnSe single layers and ZnCdSe/ZnSe QW structures and nitrogen doping of ZnSe have also been performed on novel hexagonal $Zn_xMg_{1-x}S_ySe_{1-y}$ II-VI substrates. Cross-sectional transmission electron

Reproduced with permission of the copyright owner. Further reproduction prohibited without permission.

microscopy (TEM) analysis demonstrates that hexagonal ZnSe has been achieved by using these hexagonal substrates. Photoluminescence studies suggest that nitrogen atoms have introduced acceptor levels in these hexagonal ZnSe samples and these samples were heavily doped (or highly compensated). We propose to optimize the N source conditions or use different growth planes for a more reasonable N incorporation in these hexagonal ZnSe.

Reproduced with permission of the copyright owner. Further reproduction prohibited without permission.

Acknowledgements

I gratefully thank Professor Maria C. Tamargo, from the bottom of my heart, who took great time and effort to educate me the science of semiconductor materials by molecular beam epitaxy and kept me productive throughout the course of this thesis.

Many thanks go to my colleagues, Dr. A. Cavus, Dr. B. X. Yang, Dr. S. P. Guo, Ms. Y. Y. Luo, and Mr. A. Elmoumni for their significant assistance. I also thank my committee members Professor Y. C. Chen, Dr. B. J. Fitzpatrick, Professor V. Petricevic, Professor F. H. Pollak and Professor F. W. Smith for interesting discussions and education.

Special thanks go to my wife Dale Liao and my mother Li-Zon Huang for supporting me over the years. In addition thanks to many special and important friends for keeping me sane, among them, J. Familton, Y. K. Kuo, J. Ton, A. Chen, A. Ton, W. I. Tien, and S. Ho.

Reproduced with permission of the copyright owner. Further reproduction prohibited without permission.

Table of Contents

Abstract iv

Acknowledgments vii

List of Figures xi

List of Tables xxiii

1. Introduction 1

2. Background

2-1 Molecular beam epitaxy technique 10

2-2 MBE growth of $Zn_{1-x-y}Mg_xCd_ySe$ alloys lattice-matched to InP substrates 15

2-3 Radio frequency discharge nitrogen plasma source 19

2-4 Material characterization techniques

2-4-1 Photoluminescence 26

2-4-2 Single and double crystal x-ray diffraction 28

2-4-3 Hall effect measurements 31

2-4-4 Electrical and electrochemical capacitance-voltage profiling 38

3. Bipolar Doping of Zn1-x-yMgxCdySe Alloys

Reproduced with permission of the copyright owner. Further reproduction prohibited without permission.

3-1 n-type doping of $Zn_{0.47}Cd_{0.53}Se$ and $Zn_{1-x-y}Mg_xCd_ySe$ alloys

lattice-matched to InP using $ZnCl_2$ 52

3-2 Conventional p-type doping of $Zn_{1-x-y}Mg_xCd_ySe$ using

an rf discharge nitrogen plasma source 62

3-3 p-type doping issues of Se-based II-VI materials 67

3-4 p-type doping of ZnSe using an rf discharge Nitrogen

plasma source 81

3-5 Modulation doping techniques

3-5-1 Conventional δ-doping with Nitrogen 89

3-5-2 Single (N+Te)δ-doping technique 95

3-5-3 (N+Te)δ^3-doping technique 100

3-6 p-type doping of $Zn_{1-x}Mg_xSe$ and $Zn_{1-y}Cd_ySe$ alloys 108

4. p-type Ohmic Contact Layer: ZnSe0.53Te0.47 Alloy

Lattice-matched to InP

4-1 MBE growth of ZnSe1-xTex alloys on InP substrates 117

Reproduced with permission of the copyright owner. Further reproduction prohibited without permission.

4-2 p-type doping of ZnSe1-xTex alloys using an rf discharge Nitrogen plasma source 126

5. ZnCdSe/ZnMgCdSe Quantum Well Light Emitting Diodes

5-1 MBE growth of full-color LEDs 132

5-2 Characteristics of ZnMgCdSe-based LEDs 136

6. MBE Growth of II-VI Materials on Novel Hexagonal $Zn_xMg_{1-x}S_ySe_{1-y}$ Bulk Substrates

6-1 Introduction 142

6-2 Growth and characteristics of hexagonal $Zn_xMg_{1-x}S_ySe_{1-y}$ bulk substrates 149

6-3 MBE growth of hexagonal ZnSe epilayers and ZnCdSe/ZnSe QW structures on hexagonal $Zn_xMg_{1-x}S_ySe_{1-y}$ bulk substrates 163

6-4 p-type doping of hexagonal ZnSe using an rf discharge Nitrogen plasma source 169

Publications 178

References 182

Reproduced with permission of the copyright owner. Further reproduction prohibited without permission.

List of Figures

Chapter 1

Figure 1 Schematic diagram of the ZnCdSe/ZnCdMgSe QW laser structure. 5

Chapter 2

Figure 1 Schematic diagram of MBE process. 10

Figure 2 Bandgap vs percent lattice-mismatch to InP for ZnMgCdSe quaternary layers grown on InP substrates. 15

Figure 3 Laser emission from three photo-pumped ZnCdSe/ZnCdMgSe layer structures. 16

Figure 4 Schematic setup diagram of an rf-discharge Nitrogen plasma source mounted on UHV MBE chamber. The detector is used to characterize N plasma emission. 20

Figure 5 Characteristic molecular emission spectrum recorded from the N plasma which typically produce a net acceptor level of 7×10^{17} cm^{-3}. 22

Figure 6 Schematic setup diagram of photoluminescence. 26

Figure 7 Schematic setup diagram of single crystal (SCXRD) and double crystal (DCXRD) x-ray diffraction. 28

Figure 8 Schematic setup of Hall effect measurement. 31

Figure 9 Van der Pauw Hall sample. 34

Reproduced with permission of the copyright owner. Further reproduction prohibited without permission.

Figure 10 (a) Schematic diagrams of n-type and p-type contact-semiconductor Schottky barrier. **(b)** Schematic diagram of the contact-Semiconductor interface region while a reverse bias is applied. 39

Figure 11 Schematic diagram of the band structure of a ZnSe:N sample grown on p^+ GaAs for C-V measurement. 42

Figure 12 (a) Schematic cross-sectional view of the ZnSe:N device for C-V measurements. The arrows indicate a flow of current in the ZnSe:N region. **(b)** Equivalent circuit for modeling the device in (a). 43

Figure 13 Capacitance-voltage and $1/C^2$–V curves of a ZnSe:N sample measured with 3.2 kHz ac frequency. 46

Figure 14 Schematic diagram of the electrochemical cell showing the Pt, saturated calumel electrode (SEC), carbon electrode, and the pump used to agitate the electrolyte and disperse bubbles on the semiconductor surface. 47

Chapter 3

Figure 1(a) Free electron concentration of Cl doped $Zn_{0.51}Cd_{0.49}Se$ grown with and without an InGaAs:Be buffer layer as a function of $ZnCl_2$ cell temperature. The solid line is the $ZnCl_2$ vapor pressure in arbitrary units. **(b)** Hall mobility of Cl doped $Zn_{0.51}Cd_{0.49}Se$ grown with and without InGaAs:Be

Reproduced with permission of the copyright owner. Further reproduction prohibited without permission.

buffer layer as a function of $ZnCl_2$ cell temperature. Both (a) and (b) are measured at room temperature. 55

Figure 2 Comparison of the free electron concentration of Cl-doped $Zn_{1-x-y}Mg_xCd_ySe$ (with a 77 K bandgap of 2.74 eV) as a function of the reciprocal of $ZnCl_2$ cell temperature with that of Cl-doped ZnCdSe. Both sets of samples are grown with InGaAs:Be buffer layers. 58

Figure 3 Hall mobility of ZnCdSe:Cl and ZnMgCdSe:Cl (with a 77 K bandgap of 2.74 eV) as a function of free electron concentration. Hall measurements were performed at room temperature. 59

Figure 4 Dependence of maximum free-carrier concentration on the 77K bandgap for Cl-doped $Zn_{1-x-y}Mg_xCd_ySe$ quaternary layers. 60

Figure 5 Photoluminescence spectra measured at 10 K for Cl-doped ZnCdSe and for two Cl-doped $Zn_{1-x-y}Mg_xCd_ySe$ layers of different compositions. All samples are lattice matched to InP and have a carrier concentration of 3 x 10^{18} cm^{-3}. 61

Figure 6 Photoluminescence spectrum of N doped ZnMgCdSe quaternary at 7K. The dominant peak at 2.588 eV is assigned to the near bandedge emission while the broad band at 2.491 eV is related to the Nitrogen incorporation. 64

Reproduced with permission of the copyright owner. Further reproduction prohibited without permission.

Figure 7 Capacitance-voltage (C-V) plot for a ZnMgCdSe quaternary layer with bandgap of 2.5 eV doped with Nitrogen. The $(N_A\text{-}N_D)$ level is 7 x 10^{15} cm^{-3}. 65

Figure 8 (a) Ideal bond structure of N-doped ZnSe. **(b)** Proposed model of impurity-host bond breaking. The bond between a substitutional Nitrogen and Zn host may be broken due to the lattice relaxation as shown by the dashed square. **(c)** Model of host-host bond breaking. Two Zn-Se bonds (with common Zn), nearest to a substitutional Nitrogen atom, may break as shown by the dashed squares and form a Se-Se dimer (red line). This bond-breaking complex works as a single donor. 75

Figure 9 Free electron concentration vs CBM position on an absolute energy scale. Points represent those highest reported free electron concentrations of various n-type doped II-VI materials. The solid curve represents the predicted value by the model. The dashed line suggests that some compensation effect is observed but the δ-doping technique can overcome it (blue triangle). 78

Figure 10 Depth-dependent $(N_A\text{-}N_D)$ level of a uniformly doped ZnSe:N, measured by electrochemical C-V profiling. The sample was grown with the optimum discharge Nitrogen condition. 83

Reproduced with permission of the copyright owner. Further reproduction prohibited without permission.

Figure 11 Schematic diagram of impurity levels and the transitions associated with each level in Nitrogen doped ZnSe. E_c and E_V represent the CBM and VBM positions, respectively. D^s, D^d and **A** represent the shallow donor, deep donor, and acceptor levels, respectively. **F** represents a free carrier. These arrows represent various transitions between different levels. For example, **EX** indicates the excitonic transitions. 84

Figure 12 (a) PL spectra of uniformly Nitrogen doped ZnSe [$(N_A$-$N_D)$~3 x 10^{17} cm^{-3}] at 9.5 and 60 K. Each peak, except the peak at 2.78~2.79 eV, has been assigned to different transition which is shown in Figure 11. The broad peak at around 2.75~2.76 eV is the LO-replica of the I_1 emission. **(b)** PL spectrum of the same sample at 110 K. The FA emission and its LO-replicas become dominant in the spectrum suggesting thermal ionization of shallow donors to the conduction band at this temperature. **(c)** 300 K PL spectrum of another uniformly Nitrogen doped ZnSe [$(N_A$-$N_D)$~8 x 10^{16} cm^{-3}]. The dominant peak was assigned to shallow donor-to-free hole transition as shown in Figure 11. The appearance of this peak suggests a thermal ionization of acceptor to the valance band. 86

Figure 13 Schematic diagram of a typical δ-doped structure. The dopant-concentrated atomic layer is inserted among several undoped atomic layers (spacers). 90

Reproduced with permission of the copyright owner. Further reproduction prohibited without permission.

Figure 14 Shutter control sequence of the conventional δ-doping technique with pure Nitrogen alone. 91

Figure 15 Depth-dependent (N_A-N_D) levels of conventional δ-doped ZnSe:N samples using low (a) and high (b) Nitrogen conditions. In (a), the (N_A-N_D) level is dramatically increased to 8 x 10^{17} cm^{-3} from 8 x 10^{16} cm^{-3} using the conventional δ-doping technique while the level remains around 5 x 10^{17} cm^{-3}. 92

Figure 16 Depth-dependent (N_A-N_D) level of a single (N+Te)δ-doped ZnSe. The cap layer (first 50nm) and the buffer layer were uniformly doped ZnSe:N. The (N+Te)δ-doping can increase the p-type doping level up to 1 x 10^{18} cm^{-3}. 96

Figure 17 Ideal bond structure of a single (N+Te)δ-doped ZnSe. Those 4 group VI sites (blue balls), on the same (001) plane of the substitutional Nitrogen atom (yellow ball) would be occupied by Te atoms while other 8 VI sites might be Se. 98

Figure 18(a) Schematic diagram of a (N+Te)δ^3-doped structure. **(b)** Ideal bond structure of the (N+Te)δ^3-doped ZnSe, as indicated on the dashed square of (a). Those 12 VI sites around a substitutional Nitrogen atom of the middle (N+Te)-concentrated plane might be all occupied by Te atoms. 100

Figure 19 Shutter control sequence of the (N+Te)δ^3-doping technique. 101

Reproduced with permission of the copyright owner. Further reproduction prohibited without permission.

Figure 20 Depth-dependent (N_A-N_D) level of a (N+Te)δ^3-doped ZnSe. The p-type doping efficiency of ZnSe is dramatically enhanced up to 6 x 10^{18} cm^{-3} by this new doping technique. 102

Figure 21 Contact-contact I-V characteristics of a uniformly and (N+Te)δ^3-doped sample. 103

Figure 22(a) Low-temperature PL spectra of a single (N+Te)δ-doped ZnSe at 8.6 K and 30 K. The peak at 2.652 eV becomes dominant at 30 K suggesting a Te-related peak overlapping with the first phonon-replica of the D^dAP. **(b)** 12K PL spectra of a (N+Te)δ^3-doped ZnSe on an 800nm uniformly doped ZnSe:N buffer. The black spectrum represents a sample with 350nm (N+Te)δ^3-doped region while the dashed curve is for the 150 nm after etching of the same sample. 105

Figure 23 (N_A-N_D) level of $Zn_{1-x}Mg_xSe$:N vs bandgap energy (or Mg concentration). The solid circles represent the uniformly doped ZnMgSe:N while the blue open circles are for the (N+Te)δ- doped samples. The open triangle is for (N+Te)δ^3-doped ZnSe as a reference point. 112

Figure 24 (N_A-N_D) level of $Zn_{1-y}Cd_ySe$:N vs Cd concentration. The solid circles represent the uniformly doped sample while those open circles are for the (N+Te)δ-doped samples. 113

Reproduced with permission of the copyright owner. Further reproduction prohibited without permission.

Chapter 4

Figure 1 Se concentration in $ZnSe_{1-x}Te_x$ alloys as a function of Se/Zn BEP ratio used during MBE growth. The dashed line shows near proportional relation determined by a least-squares fit. 120

Figure 2 **(a)** Single crystal x-ray diffraction spectrum of the $ZnSe_{0.62}Te_{0.38}$ alloy. **(b)** Double crystal x-ray rocking curve of the sample in (a) taken at two different regions of the wafer. The top scan is intentionally shifted by 250 arcsec for clarity. **(c)** Single crystal scan of a $ZnSe_{0.53}Te_{0.47}$ layer. **(d)** Double crystal rocking curve for the sample in (c). 122

Figure 3 **(a)** 5K PL spectrum of the Nitrogen doped $ZnSe_{0.50}Te_{0.50}$ alloy. The arrow indicates the position of the calculated 5K bandgap for this alloy. **(b)** Energy of 5K PL peak of $ZnSe_{1-x}Te_x$ alloys as a function of Te content (x). (Points at x=0, 0.35, 0.85 and 1 represent undoped samples, the rest are Nitrogen doped). The solid curve represents the 5K bandgap of $ZnSe_{1-x}Te_x$ alloys calculated from the empirical formula of Ref. 7. 123

Figure 4 Free hole concentrations for $ZnSe_{1-x}Te_x$ alloys doped with N under two different N plasma source conditions (circles). The triangles represent the net acceptor concentration of $ZnSe_{1-x}Te_x$ alloys measured by ECV for samples grown under condition II. The dashed lines are drawn to aid the eye.

Reproduced with permission of the copyright owner. Further reproduction prohibited without permission.

The square represents the value for N doped ZnTe reported by I.W. Tao, et al.[11] 127

Figure 5 Current-voltage characteristics between two contacts on a lattice-matched $ZnSe_{0.53}Te_{0.47}$:N sample. The linear behavior between I and V suggests an ohmic contact. 130

Chapter 5

Figure 1 Schematic diagrams of the LED structures made from ZnCdSe/ ZnMgCdSe QW system. 134

Figure 2 Current-Voltage (I-V) characteristics of a ZnMgCdSe-based LED structure with Au contact. The top contact is an Au dot (~0.3 mm^2). 137

Figure 3 Surface electroluminescence (EL) spectra for an LED structure with a thick (100 nm) $ZnSe_{0.53}Te_{0.47}$ p^+ contact layer (solid curve). The dashed line represents the EL for the same structure after etching the top $ZnSe_{0.53}Te_{0.47}$ layer to 15 nm. The broad red emission in the as-grown structure originates from the $ZnSe_{0.53}Te_{0.47}$ cap layer and not from the QW. 138

Figure 4 Surface electroluminescence (EL) spectra for three LED structures that differ only in the QW thickness and /or composition used. Emission throughout the visible range is observed. 140

Reproduced with permission of the copyright owner. Further reproduction prohibited without permission.

Chapter 6

Figure 1 Image of birefringence test of the 12% Mg substrate. The multi-color bands represents the boundaries of twins suggesting that the substrate is a highly twinned hexagonal. 152

Figure 2 Schematic setup diagram of uniaxiality test. 152

Figure 3 Interference figure of uniaxiality of the 16% Mg crystal. The directions of the isogyre cross are those of the polarizer and analyzer. This interference demonstrates that the 16% Mg crystal is pure hexagonal. 153

Figure 4 (a) Cross sectional TEM image of a ZnMgSSe crystal with 16% Mg. 156

Figure 4 (b) A (0001) diffraction pattern from this sample. 157

Figure 5 Cross sectional TEM image of a ZnCdSe/ZnSe QW structure grown on a ZnMgSSe substrate with 12% Mg content. The inset shows the $(10\bar{1}0)$ diffraction pattern of this sample. 158

Figure 6(a) Photoluminescence at 77K of the 12% and 16% Mg crystals. The emissions at 2.93 eV and 3.06 eV are the near bandgap emissions for the 12% Mg crystal and the 16% Mg crystals, respectively. Spectra (a)-(d) show the temperature-dependent PL of the 12% Mg crystal. The assignment

Reproduced with permission of the copyright owner. Further reproduction prohibited without permission.

of the bandgap emission at 2.82 eV for the 12% Mg crystal at 300K has been confirmed by ellipsometry measurements. 160

Figure 7 Single crystal x-ray diffraction spectrum (θ-2θ scan) of the 12% Mg crystal. 163

Figure 8(a) 77K PL spectrum of hexagonal ZnSe on a hexagonal ZnMgSSe substrate. The inset on (a) represents a 77K PL spectrum of a substrate that has similar deep level emission at around 2.3 eV. **(b)** 6K PL spectrum of the sample on (a). The spectrum shows no defect-related Y-line emission at around 2.60 eV. 165

Figure 9 77K PL spectrum of the $Zn_{0.7}Cd_{0.3}Se/ZnSe$ QW structure. 167

Figure 10 Double crystal x-ray rocking curve from the (11$\bar{2}$0) plane for a ZnCdSe/ZnSe QW structure grown on the 12% Mg quaternary substrate. 168

Figure 11 7K PL spectra of h-ZnSe:N with rf power of 400 W (solid), 300 W (dashed), and 200 W (dotted). The excitation intensity of all samples is 3 x 10^{-4} I_0. 171

Figure 12 schematic diagram of the perturbed bands and impurity levels. The solid arrows represent the carrier recombination from the lowest electron states to the highest hole states in the impurity levels, thus reducing the energy of transition (the red shift). 172

Reproduced with permission of the copyright owner. Further reproduction prohibited without permission.

Figure 13 Excitation-dependent PL spectra of the h-ZnSe:N samples with rf powers of 400 W (a), 300 W (b), and 200 W (c). All of the samples show strong blue shifts as the excitation intensity increases. 173

Reproduced with permission of the copyright owner. Further reproduction prohibited without permission.

List of Tables

Chapter 2

Table 1 Sequence of voltage measurement for determination of resistivity. 35

Table 2 Sequence of voltage measurement for determination of Hall coefficient. 36

Table 3 List of measured (N_A-N_D) levels for several nitrogen-doped samples grown on GaAs. The levels were determined by the C-V curves using different ac frequencies. 44

Chapter 3

Table 1 Proposed compensating defects that limit the p-type doping in Nitrogen doped ZnSe. Those underlined are defects less likely to exist in MBE grown ZnSe:N, based on prior studies. 69

Table 2 Summary table of several significant (N+Te)δ-doped samples with different doping parameters. 97

Chapter 5

Table 1 Materials parameters relevant for LED fabrication of $Zn_{1-x-y}Mg_xCd_ySe$ structures lattice-matched to InP. 133

Reproduced with permission of the copyright owner. Further reproduction prohibited without permission.

Table 2 Parameters for the three LED structures investigated in this section. 136

Reproduced with permission of the copyright owner. Further reproduction prohibited without permission.

Chapter 1
Introduction

Semiconductor lasers and light emitting diodes (LED) that emit in the visible range have potential use in various applications, e.g. optical storage, film marking, photochemical fabrication, cell sorting in medical diagnostics, DNA-taggant fluorescence, pumping small dye lasers, and full color displays. In Japan, red, yellow, and green LEDs fabricated from different material systems have been used as traffic lights that have much longer life time, brighter emission using less power, and less maintenance than the traditional light bulbs. Currently, infrared or red lasers have been used in laser printing and digital recording. By reducing the wavelength to blue, the density of the recording will have a 4-fold increase. Furthermore, high definition and high brightness display panels may benefit from semiconductor laser-based technology. Current semiconductor based full-color displays, using the three primary colors: red, green and blue (R-G-B), rely on different materials grown on different substrates. For example, room temperature cw blue lasers

Reproduced with permission of the copyright owner. Further reproduction prohibited without permission.

made from GaN materials[1] have been reported, while green lasers are made from ZnSe-based materials on GaAs,[2] and red lasers are available from InGaP based III-V materials.[3] The use of different materials and substrates results in a difficulty to integrate the three colors for high resolution displays. Thus, in order to fabricate an integrated system, it is of interest to develop compatible materials that produce the three colors and that may be grown in high quality on a single substrate.

Although blue lasers and LEDs with lifetime of about 10,000 hours have been made from GaN-based III-V materials, it is still limited to only one laboratory (Nichia, Japan) in the world. One of the problems in this material system is the lack of suitable substrates with lattice constants close to those of the nitride epilayers. Substrates, such as SiC, silicon, sapphire, and GaAs, currently used to grow nitride epilayers cause mismatch-induced defects into the epilayers which limit the performance of lasers and LEDs. Therefore, it is of interest to explore other materials which can be used to design a lattice-matched structure emitting light in blue and even throughout the entire visible range.

Reproduced with permission of the copyright owner. Further reproduction prohibited without permission.

Wide bandgap II-VI semiconductors are promising materials for the development of LEDs and laser diodes.[8] Since the first demonstration of the ZnSe-based blue-green laser in 1991, many efforts have been devoted to pseudomorphic structures grown on GaAs.[2] With these materials, SONY has reported a blue-green laser diode with a lifetime of cw operation at room temperature of 500 hours. Although this represents significant advances, device lifetime must be greatly extended for practical device applications. Due to the lack of II-VI bulk substrates, most of II-VI materials were typically grown on III-V substrates such as GaAs. Recent studies have suggested that the strained ZnCdSe active layer in the GaAs-based structures may be responsible for the nonluminescent dark line defects which appear during cw operation.[4]

We have recently developed an entirely lattice-matched material system and have reported photo-pumped ZnCdSe/ZnMgCdSe quantum well lasers on InP substrates with light emission throughout the visible range (red, green, and blue). This was obtained by changing only the thickness and/or composition of the ZnCdSe active layer.[5,6] At present, the optimized $Zn_{1-x-y}Mg_xCd_ySe$ quaternary has a defect density, caused by stacking faults,

Reproduced with permission of the copyright owner. Further reproduction prohibited without permission.

of about mid-10^4 cm^{-2}.[7] The absence of strain in the structure is expected to reduce the degradation problem and thus lengthen the lifetime of the laser diodes. Preliminary results of e-beam induced degradation studies using calthodoluminescence reveal the absence of dark line defects in these lattice-matched quantum well systems.[9]

The major goal of this thesis is to develop II-VI wide bandgap semiconductor materials for LEDs and diode lasers emitting light in the visible range. We have pursued this goal along two directions. In the first part (from Chapter 3 to Chapter 5) the focus was on the bipolar doping and electroluminescence of the $Zn_{1-x-y}Mg_xCd_ySe$ system grown on InP substrates. In the second part (Chapter 6) novel "hexagonal" $Zn_xMg_{1-x}S_ySe_{1-y}$ II-VI bulk substrates, grown at Optical Semiconductors Inc., were investigated and epitaxial growth of hexagonal ZnSe and ZnCdSe/ZnSe quantum well structures on these novel substrates was performed.

For the first part, in order to fabricate light emitting devices from the $Zn_{1-x-y}Mg_xCd_ySe$ system, several requirements have been identified. Figure 1 shows a schematic diagram of a proposed diode laser structure made from this material system. Those requirements are summarized as the following:

Reproduced with permission of the copyright owner. Further reproduction prohibited without permission.

1. *Bipolar doping of the $Zn_{1-x-y}Mg_xCd_ySe$ cladding and waveguide layers,*

2. *The growth of* $ZnSe_{0.53}Te_{0.47}$ *lattice-matched to InP as a contact layer and its p-type doping, and*

3. *Investigation of electrical and electroluminescence properties of LEDs from these materials.*

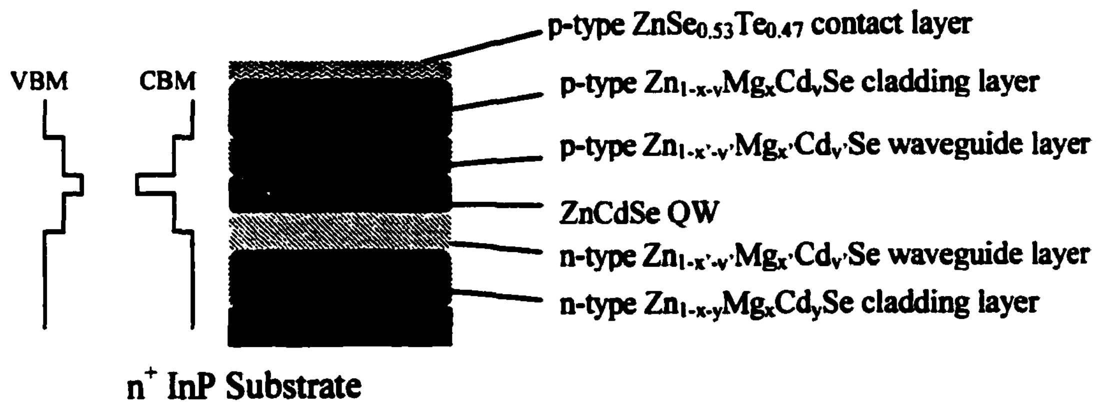

Figure 1 Schematic diagram of the ZnCdSe/ZnCdMgSe QW laser structure

The growth of high quality $Zn_{1-x-y}Mg_xCd_ySe$ alloys with various elemental compositions and bandgap energies (from 2.1 to 3.3 eV) has been developed in our group using molecular beam epitaxy (MBE). A brief introduction about the MBE growth will be given in Chapter 2. The operation of a radio frequency (rf) discharge N source used for doping and

Reproduced with permission of the copyright owner. Further reproduction prohibited without permission.

several material characterization techniques including photoluminescence, x-ray diffraction measurements, Hall effect measurement, and electrical and electrochemical capacitance-voltage profiling will also be briefly described in Chapter 2.

In Chapter 3, the n-type and p-type doping will be investigated. In general, good device performance requires high doping levels (in the range of 10^{17} cm^{-3} or higher). The n-type doping of $Zn_{1-x-y}Mg_xCd_ySe$ alloys using $ZnCl_2$ has been accomplished with free electron concentration in the range of 10^{18} cm^{-3} while the p-type doping level (N_A-N_D) obtained by using an rf discharge N plasma source is limited to about 1 x 10^{16} cm^{-3}. The p-type doping difficulties of the $Zn_{1-x-y}Mg_xCd_ySe$ alloys will also be discussed in this chapter. Several proposed mechanisms that may be responsible for limiting the achievable p-type doping level of N doped ZnSe (ZnSe:N) will be reviewed. Modulation doping techniques, including the conventional δ-doping with N and modified δ-doping with N and Te co-doping, will be investigated to enhance the p-type doping level of ZnSe:N. Then, the p-type doping of $Zn_{1-x}Mg_xSe$ and $Zn_{1-y}Cd_ySe$ ternaries as a function of material concentrations will be studied. Based on these studies, possible p-type

Reproduced with permission of the copyright owner. Further reproduction prohibited without permission.

compensation mechanisms in the $Zn_{1-x-y}Mg_xCd_ySe$ system and an approach for enhancing the achievable p-type doping level of the quaternaries will be proposed.

In Chapter 4, we focus on the second task, the growth of the lattice-matched $ZnSe_{0.53}Te_{0.47}$ contact layer and its p-type doping using an rf-discharge N plasma source. It is difficult to control the compositions of Se and Te in $ZnSe_{1-x}Te_x$ alloys under group VI rich conditions due to the strong preferential incorporation of Se over Te. However, a growth technique was developed to achieve high quality $ZnSe_{0.53}Te_{0.47}$ alloys with excellent compositional control of Se and Te in the solid by adjusting the Se/Zn ratio of the beam equivalent pressure (BEP, proportional to elemental fluxes) under group VI rich conditions. A systematic study of the p-type doping of $ZnSe_{1-x}Te_x$ alloys as a function of Te content will be also presented in this chapter. The $ZnSe_{0.53}Te_{0.47}$ alloy lattice-matched to InP can have a free hole concentration of 2×10^{19} cm^{-3} which leads to the formation of an ohmic contact for device applications.

In Chapter 5, fabrication of three-color LEDs by combining these results is presented. The structures include a high quality n-type

Reproduced with permission of the copyright owner. Further reproduction prohibited without permission.

$Zn_{1-x-y}Mg_xCd_ySe$ ($n \sim 10^{18}$ cm^{-3}), a ZnCdSe QW layer, a p-type $Zn_{1-x-y}Mg_xCd_ySe$ [$(N_A-N_D) \sim 1 \times 10^{16}$ cm^{-3}], and a highly p-type doped and lattice-matched $ZnSe_{0.53}Te_{0.47}$ contact layer. The LED structures show a typical behavior of p-n junction in current-voltage characteristics. An abrupt and low turn-on voltage (< 4 V) was observed for the LEDs. Electroluminescence (EL) emission in the red, yellow, and blue-green has been observed from these LED structures by only adjusting the thickness and/or composition of QW layers, demonstrating the capability to fabricate full color displays.

Chapter 6 will focus on the topic of hexagonal $Zn_xMg_{1-x}S_ySe_{1-y}$ substrates whose lattice constants are matched to that of ZnSe. A combination of x-ray characterization (including single crystal θ-2θ scan and powder diffraction) and optical microscopy (including birefringence and uniaxiality tests) is used to identify the hexagonal structure and determine the lattice constants. Transmission Electron Microscopy (TEM) is also used to confirm the crystal phase. The transition of the substrates between the cubic phase and the hexagonal phase as a function of Mg content has been observed. Hexagonal ZnSe epilayers and ZnCdSe/ZnSe QW structures have

Reproduced with permission of the copyright owner. Further reproduction prohibited without permission.

been grown on these novel hexagonal II-VI substrates. Nitrogen doping has been performed for p-type hexagonal ZnSe using an rf discharge N plasma source. Several photoluminescence measurements at low temperature were also used to study the incorporation of nitrogen for these hexagonal ZnSe samples.

Reproduced with permission of the copyright owner. Further reproduction prohibited without permission.

Chapter 2
Background

2-1 Molecular beam epitaxy technique

Molecular beam epitaxy (MBE) is a versatile technique for depositing semiconductor epilayers or structures. The deposition process is achieved in an ultra-high vacuum (UHV) environment.[1] Figure 1 shows the schematic diagram of the MBE process for ZnCdSe epitaxy. The molecular and atomic beams are provided by thermal Knudsen effusion cells where

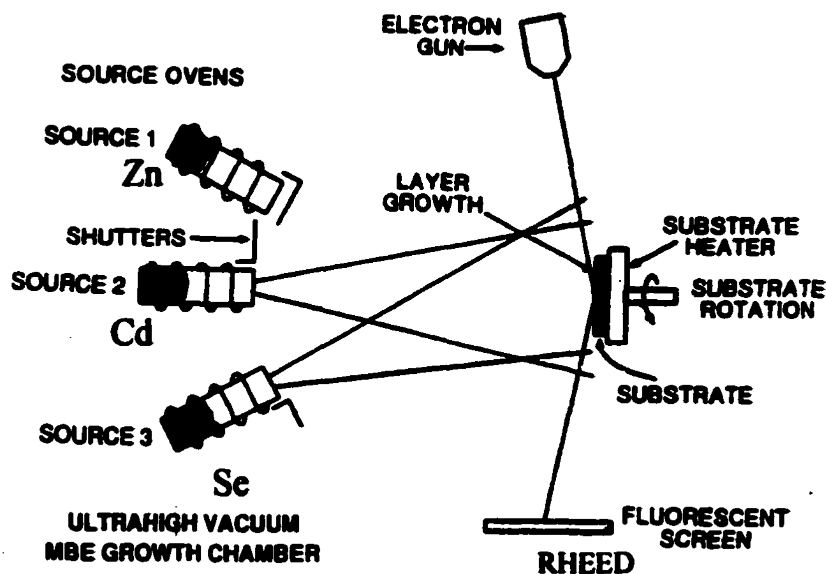

Figure 1 Schematic diagram of MBE process.

Reproduced with permission of the copyright owner. Further reproduction prohibited without permission.

each cell holds a crucible containing the chemical elements with ultra high purity (>99.9999%). The temperature of each cell is controlled by a computer at a suitable point so that the vapor pressure of the material is sufficiently high and stable for generation of a thermal molecular (or atomic) beam by free evaporation. The cells are arranged so that the central portion of the beam flux distribution from each cell intersects on the substrate. The material composition of the desired epilayer is controlled by controlling the flux ratio of elements. The thermal beam fluxes are measured by measuring the beam equivalent pressures (BEP) obtained by a flux gauge placed at the equivalent position of the substrate. Each cell has a mechanical shutter in front of the beam source which is used to interrupt the beam fluxes, i.e., to start and to stop the deposition and/or doping.

Thin films crystallize via reactions between thermal molecular or atomic beams of the constituent elements on a substrate surface which is maintained at a suitable temperature. The composition of the grown epilayer and its doping level depend on the relative arrival rates of the constituent elements and dopants, which in turn depend on the evaporation rates of the appropriate sources. MBE growth is carried out under conditions far from

Reproduced with permission of the copyright owner. Further reproduction prohibited without permission.

thermodynamic equilibrium and is governed mainly by the kinetics of the surface processes occurring when the impinging beams react with the outermost atomic layers of the substrate crystal.[1] This is in contrast to other epitaxial growth techniques, such as liquid phase epitaxy or vapor phase epitaxy, which proceed at conditions near thermodynamic equilibrium and are most frequently controlled by diffusion processes occurring in the crystallizing phase surrounding the substrate crystal.[1]

The typical MBE growth rate of 1 μm/h (~1 monolayer/sec) is low enough that surface migration of the impinging species on the grown surface is ensured. Consequently, the surface of the grown film is very smooth. An in-situ reflection high-energy electron diffraction (RHEED)[2] technique is used as a real-time diagnostic tool for the smoothness of the growing surface. As shown in Figure 1, the high energy electron beam impinges onto the growing surface with a shallow incident angle of ~1° to the sample surface. Due to the small incident angle, the electron beam will generate a diffraction pattern reflecting the lattice structure of the outermost atomic layers and project the diffraction pattern on a fluorescent screen placed on the opposite side of the e-beam source in the MBE chamber. In general, a streaky

Reproduced with permission of the copyright owner. Further reproduction prohibited without permission.

RHEED pattern suggests a smooth surface and a two dimensional growth mode (layer by layer growth) while a spotty one suggests a rough surface and a three dimensional growth mode.[1,2] A three dimensional growth mode induces stacking faults and may even result in polycrystalline formation. In terms of crystalline quality, a layer-by-layer growth (two dimensional growth mode) is strongly preferred for crystalline formation in MBE growth.[1,2]

The experiments for this dissertation were accomplished in a Riber 2300P MBE system. Within the MBE system, there are a III-V and a II-VI growth chambers connected to each other by UHV modules. Eight elemental sources are installed on the III-V chamber including Ga, In, Al, Mn, As, InP (for P flux), Si (for n-type doping), and Be (for p-type doping) and eight sources are in the II-VI growth chamber including Zn, Cd, Mg, Se, Te, Be, $ZnCl_2$ (for n-type doping), and a radio frequency (rf) discharge N source (for p-type doping). These source elements are ultra high purity (from 6N to 8N) to ensure that high purity films are grown. Both growth chambers are cooled by liquid Nitrogen to maintain a clean UHV environment during growth. All the substrate deoxidization and growth of the III-V buffer layers are

Reproduced with permission of the copyright owner. Further reproduction prohibited without permission.

performed in the III-V chamber. After that, samples are transferred to the II-VI chamber via the UHV track chamber. Then the II-VI epitaxial growth is performed in the II-VI chamber.

Reproduced with permission of the copyright owner. Further reproduction prohibited without permission.

2-2 MBE growth of $Zn_{1-x-y}Mg_xCd_ySe$ alloys lattice-matched to InP substrates

Wide bandgap $Zn_{1-x-y}Mg_xCd_ySe$ material system has potential use for fabrication of visible light emitting devices. Our group has demonstrated that the $Zn_{1-x-y}Mg_xCd_ySe$ family can be grown lattice-matched to InP substrates.[3] Figure 2 shows the bandgap of this material system as a function of percent lattice mismatch to InP. As shown in Figure 2, the $Zn_{1-x-y}Mg_xCd_ySe$ quaternaries lattice-matched to InP can have bandgap energies from ~2.1 to 3.5 eV so that they can be used as cladding and waveguide layers in diode laser and LED structures. The lattice-matched $Zn_{0.51}Cd_{0.49}Se$ ternary (E_g~ 2.1 eV) can be used as a quantum well (QW) layer and can have light emission in the range from yellow to blue by changing the width of the QW layer. By using a pseudomorphic ZnCdSe layer with more Cd concentration as the QW layer, red

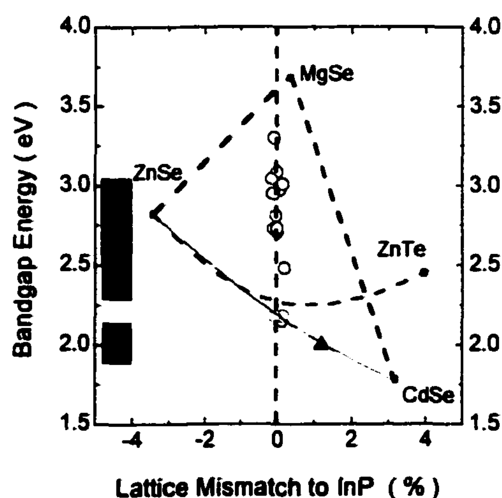

Figure 2 Bandgap vs percent lattice-mismatch to InP for ZnMgCdSe quaternary layers grown on InP substrates.

Reproduced with permission of the copyright owner. Further reproduction prohibited without permission.

emission can be obtained. In fact, photo-pumped lasers made from the ZnCdSe/ZnMgCdSe QW system which emit light in the red, green, and blue colors (R-G-B) have been achieved.[4] Figure 3 shows the above threshold laser emission from three ZnCdSe/ZnMgCdSe QW laser structures grown on InP substrates with emission wavelengths from 497 to 604 nm, covering the range from blue to red. This result demonstrates that this material system could be used to fabricate light emitting devices with light emission covering the entire visible range.

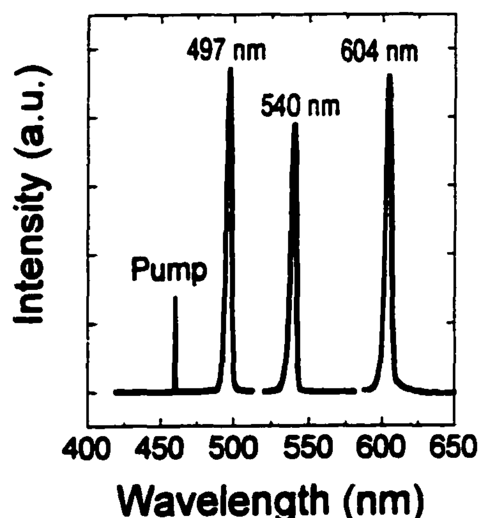

Figure 3 Laser emission from three photo-pumped ZnCdSe/ZnCdMgSe layer structures.

The $Zn_{1-x-y}Mg_xCd_ySe$ samples are grown lattice-matched on (100) InP substrates. Prior to loading the substrate into the UHV chamber, the InP substrates are prepared by ex-situ chemical etching in H_2SO_4:H_2O_2:H_2O (4:1:1) solution. Then the substrate is introduced into the III-V growth chamber followed by an in situ thermal deoxidization at about 500 °C. Arsenic passivation is used during the thermal deoxidization procedure.[3] A

Reproduced with permission of the copyright owner. Further reproduction prohibited without permission.

lattice-matched InGaAs buffer layer is grown at 480 °C after the deoxidization of the substrate, with a thickness of about 80 nm. After the growth of the InGaAs III-V buffer layer, the sample is then transferred to the II-VI growth chamber. Prior to the growth of the II-VI epilayer, the sample is exposed to a Zn flux (Zn irradiation) for 20 sec to suppress the formation of Ga_2Se_3-related complexes on the III-V/II-VI interface.[5] By using this pre-growth treatment, the etch pit density (stacking fault density) of $Zn_{1-x-y}Mg_xCd_ySe$ epilayers can be reduced to the mid 10^4 cm^{-2}.[5]

For the growth of lattice-matched $Zn_{0.51}Cd_{0.49}Se$ on InP, the beam equivalent pressure (BEP) ratio of Cd to Zn is 2 while it is kept at 1.6 for the growth of lattice-matched $Zn_{1-x-y}Mg_xCd_ySe$ quaternaries.[3] The Mg concentration in the quaternaries is controlled by the Mg cell temperature. The ternary and quaternary growths are performed under Se-stabilized conditions with the Se BEP four times larger than the total group II element flux. Under these growth conditions, the lattice mismatch to InP substrate is less than 0.2% for all samples. In order to obtain two-dimensional nucleation of the II-VI materials on InP, it is necessary to start the growth at a temperature lower than 250 °C, which is the optimum growth temperature

Reproduced with permission of the copyright owner. Further reproduction prohibited without permission.

for these materials. In practice, the initial growth temperature is set to 170 °C. A (2 x 1) surface reconstruction develops in the RHEED pattern within few seconds. A low-temperature ZnCdSe buffer is grown for 1 min followed by about 4 min growth interruption during which the substrate temperature is raised to the desired growth temperature of 250 °C. Then the $Zn_{0.51}Cd_{0.49}Se$ or $Zn_{1-x-y}Mg_xCd_ySe$ layers are grown. The growth rate is about 1 μm/hr for both materials.

Reproduced with permission of the copyright owner. Further reproduction prohibited without permission.

2-3 Radio frequency discharge nitrogen plasma source

Atomic nitrogen is used as a p-type dopant for the II-VI materials studied in this thesis. The source is obtained by a radio frequency (rf) discharge N plasma. A nitrogen plasma is generated by inductively coupling 13.56 MHz energy into a small cylindrical pyrolytic boron nitride (PBN) discharge chamber supplied with ultra-pure (99.9999%) nitrogen gas. Figure 4 shows the schematic diagram of the nitrogen source setup. The discharge system (MPD 21R) was manufactured by Oxford Applied Research, UK. The PBN discharge tube is surrounded by a water-cooled rf coil and the N_2 gas is fed into the tube via a leak valve at one end of the tube while at the other end, a PBN disk with one fine hole (0.2 mm in diameter) serves as the exit plate. The fine hole permits a fraction of the active nitrogen species to diffuse out of the discharge chamber towards the substrate inside the MBE growth chamber. The assembly is mounted on a Conflat flange and fits on the MBE growth chamber in place of a conventional effusion source. The rf input power supplied to the discharge chamber in the source can be varied up to 400 W (at 13.56 MHz), the reflected power being < 2 W as established by an automatic tuning network. For the characterization of the emission

Reproduced with permission of the copyright owner. Further reproduction prohibited without permission.

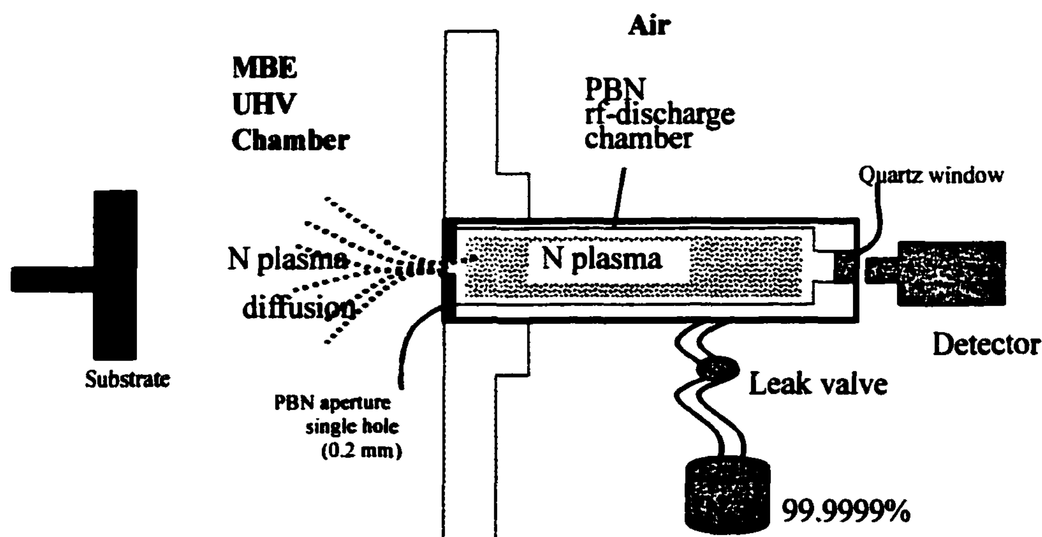

Figure 4 Schematic setup diagram of an rf-discharge Nitrogen plasma source mounted on UHV MBE chamber. The detector is used to characterize N plasma emission.

from the discharge nitrogen plasma, two types of optical detectors, including a Si photodiode and a photodiode array (PDA) detector which is connected with an optical fiber, are alternatively mounted on the air side of the discharge chamber.

For obtaining a discharge nitrogen plasma, a standard operation procedure should be followed. First of all, the discharge PBN chamber should be filled with pure molecular N_2. Then the rf discharge power should be turned on and kept at 200 W. By adjusting the N_2 flow rate, a "low brightness" discharge mode will be first turned on at a specific flow rate,

Reproduced with permission of the copyright owner. Further reproduction prohibited without permission.

consistent with a nitrogen background pressure of high 10^{-6} torr. As soon as the low brightness mode is achieved, the discharge of a high brightness is struck by reducing the N_2 flow rate. The high brightness mode is preferred for better doping efficiency. A higher or lower rf discharge power can be further adjusted depending on the doping level intended. A Si photodiode is used to monitor the overall intensity of the plasma emission. In general, the measured intensity is dependent on both the rf discharge power and the nitrogen flow (or the partial pressure in the growth chamber). The Si photodiode output (the overall plasma emission intensity) is typically maintained at a stable value which is obtained by establishing an equilibrium nitrogen background pressure in the MBE growth chamber. For an optimum doping condition of ZnSe, the plasma emission intensity typically is kept at about 600 mV corresponding to the rf discharge power of 400 W and a nitrogen background pressure of 8 x 10^{-6} torr. These conditions typically produce a net acceptor concentration of high 10^{17} cm^{-3} in uniformly N doped ZnSe.

Dissociated atoms undergoing wall collisions in the discharge chamber exhibit a low recombination coefficient and may also ultimately contribute

Reproduced with permission of the copyright owner. Further reproduction prohibited without permission.

to the radical beam flux. The pressure in the discharge chamber is sufficiently low ($< 10^{-3}$ torr) that atom-gas collisions are minimal over the dimensions of discharge chamber. Fortunately, Wright and Winkler et al[6] have provided a comprehensive review of the characteristic emission spectra that have been observed in active nitrogen plasmas produced by various methods such as microwave and radio frequency inductive coupling and high-voltage discharge techniques. Molecular emission spectroscopy is used to characterize the active nitrogen in the discharge plasma. For this purpose, the Si photodiode is replaced by an optical fiber which directs emission light into a PDA detector. The wavelength sensitivity of the PDA detector is from 400 nm to 1100 nm with resolution of about 5 nm.

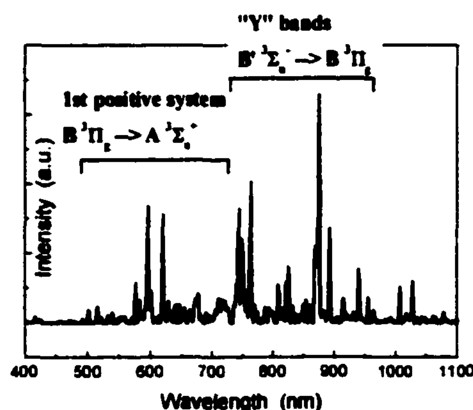

Figure 5 Characteristic molecular emission spectrum recorded from the N plasma which typically produce a net acceptor level of 7×10^{17} cm^{-3}.

The molecular emission spectrum shown in Figure 5 was recorded under the optimum source conditions detailed above. As shown in Figure 5, the spectrum mainly comprises emissions in the

Reproduced with permission of the copyright owner. Further reproduction prohibited without permission.

region between 500 nm and 900 nm. It has been reported and confirmed[6,7] that those emissions are associated with two emission systems involving molecular N_2 transitions identified as the first positive system (B $^3\Pi_g \rightarrow$ A $^3\Sigma_u^+$) and the "Y" band (B' $^3\Sigma_u^- \rightarrow$ B $^3\Pi_g$) of N_2. Emissions between 500 nm and about 700 nm are assigned to the first positive system of N_2 while those between 700 nm and 900 nm are assigned to the "Y" bands as shown in Figure 5.[7] The first positive system transitions are generally thought to occur as a result of the recombination of ground state nitrogen (^{4}S) atoms while the Y system is associated with the recombination of ground state nitrogen atoms and a collision-induced radiationless transition from the $^5\Sigma_g^+$ state of N_2. Emissions from atomic nitrogen are difficult to detect since some of them occur in the region where the first positive bands of N_2 are and some are forbidden by electric dipole selection rules. They do not seem to have been reported in gaseous active nitrogen systems.[6] Since the spectrum shown in Figure 5 is dominated by emission bands which are associated with the first positive system and the Y bands of N_2 (both of which involve N atoms), it is expected that a significant concentration of ground state nitrogen atoms must be present in the discharge nitrogen plasma.

Reproduced with permission of the copyright owner. Further reproduction prohibited without permission.

In contrast, emission bands which could be associated with the presence of nitrogen ions in the plasma which may degrade the doping efficiency and the crystalline quality are not observed. Such bands would appear in the near-UV regime in the range 300-500 nm. Signals above the background noise level were not obvious in this regime. Consistent with that, Hoke et al[8] has shown, by employing a Faraday cup detector, that the ion content in fluxes emanating from such rf discharge nitrogen plasma sources is extremely small (< 0.1%). However, the ion densities can be further reduced by increasing nitrogen flow corresponding to the increase of the plasma pressure in the discharge chamber and by the use of apertures with small holes. Therefore, the way to have an optimum nitrogen source, in terms of more atomic nitrogen without ions, is to use high nitrogen flow and a small hole exit aperture.

By the molecular emission spectrum above, it is believed that the flux emanating from the PBN plasma discharge tube comprises ground state (^4S) nitrogen atoms and N_2 molecules in ground state and various excited states. Since the mean free path in a 10^{-6} torr environment is greater than the source-to-substrate distance, the species effusing from the source will not

Reproduced with permission of the copyright owner. Further reproduction prohibited without permission.

undergo collisions on route to the substrate and will consequently preserve their state.

Although nitrogen doping by means of dissociated molecular species whose dissociation takes place locally at the substrate cannot be completely ruled out, it is believed that the atomic nitrogen content in the flux emanating from the source is responsible for the efficient nitrogen doping of ZnSe during MBE growth. The N_2 (A $^3\Sigma_u^+$) molecule, for instance, would require increasing its internal energy at the substrate by approximately 3.5 eV[6] in order to dissociate and provide two nitrogen atoms for doping. This seems an unlikely possibility at the low substrate temperature involved in the MBE growth of II-VI materials (typically in the 200-300 °C range).

Reproduced with permission of the copyright owner. Further reproduction prohibited without permission.

2-4 Material characterization techniques

2-4-1 Photoluminescence

The schematic diagram of the photoluminescence (PL) setup is shown in Figure 6. Samples for PL measurements are mounted on a cold finger of a Janis Cryogenic system. The system is pumped to vacuum (~ 10^{-5} Torr) before cooling it. For measurements at 77 K, the cold finger is cooled using liquid Nitrogen. For measurements at lower temperatures such as from 5 to 77 K, the cold finger is cooled using liquid Helium. For temperature-

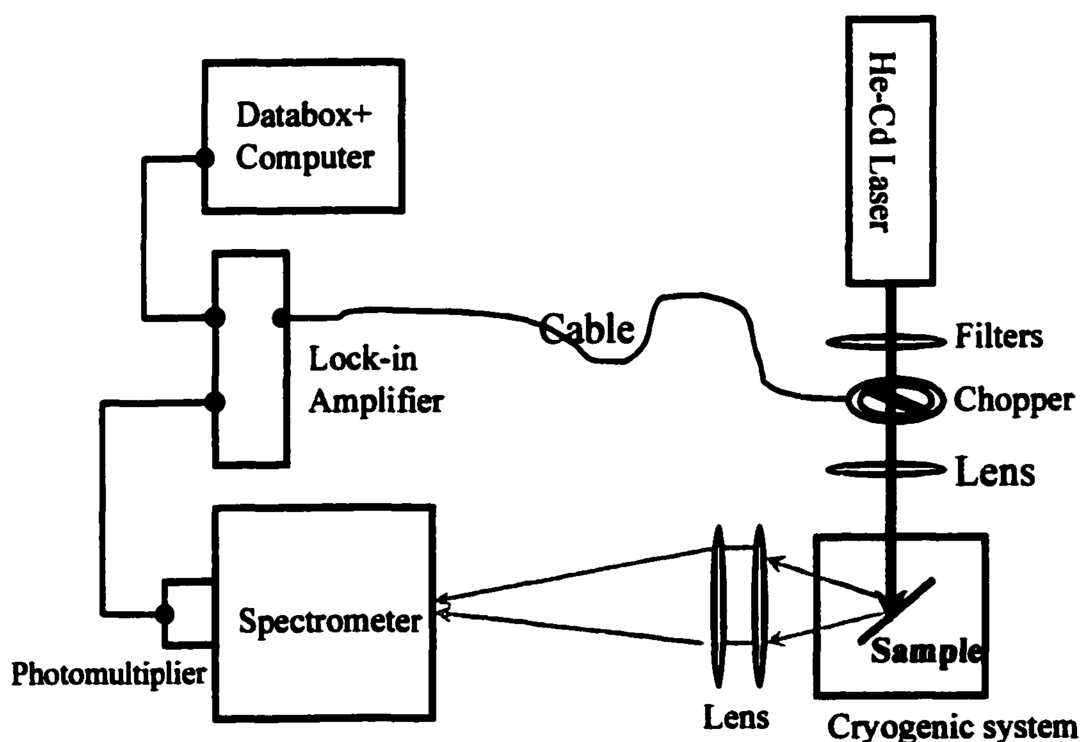

Figure 6 Schematic setup diagram of photoluminescence.

Reproduced with permission of the copyright owner. Further reproduction prohibited without permission.

dependent PL measurements, the temperature of the cold finger is controlled by a temperature controller with a heater installed on the back of the cold finger. A He-Cd laser with the emission wavelength of 325 nm is used as the excitation source. The laser beam passes through a chopper, which converts the dc laser beam to an ac signal, then it is focused by means of lenses onto a small spot on a sample. The luminescence from the sample is focused onto a spot on the front slit of the spectrometer (SPEX 1680-B). The signal from the spectrometer is collected by a photomultiplier and converted to an electrical signal. The ac signal goes to a lock-in amplifier to be amplified. Then a databox (DataScan) collects the amplified signal and the data is plotted as a spectrum by a spectroscopic acquisition and analysis software (SpectraMax). The PL spectrum can provide information about the optical properties of the epilayers such as emissions related to bandgap, donor and/or acceptor states, and deep defect levels.

Reproduced with permission of the copyright owner. Further reproduction prohibited without permission.

2-4-2 Single and double crystal x-ray diffraction

Single and double crystal x-ray diffraction is used to characterize the crystalline quality, lattice constant, crystal structure, and strain of semiconductor materials. The schematic diagram of the setup is shown in Figure 7. The x-ray is generated by a Cu x-ray source producing two lines, $K_{\alpha 1}$ (λ = 1.54056 A) and $K_{\alpha 2}$ (λ = 1.54439 A). The system for the single crystal x-ray diffraction (SCXRD) was manufactured by RIGAKU and that for the double crystal x-ray diffraction (DCXRD) was manufactured by

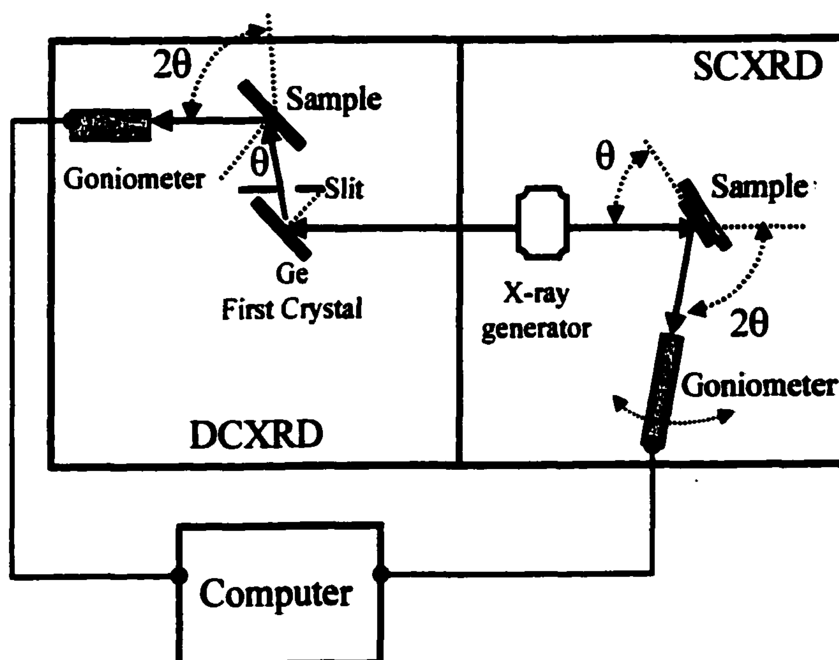

Figure 7 Schematic setup diagram of single crystal (SCXRD) and double crystal (DCXRD) x-ray diffraction.

Reproduced with permission of the copyright owner. Further reproduction prohibited without permission.

Blake Industries, Inc. In both cases, the rotation of the sample holder will change the incident angle θ while rotation of the goniometer will change 2θ.

In SCXRD measurement, the sample (θ) and the goniometer (2θ) are rotated simultaneously. The incident x-ray is not monochromatic ($K_{\alpha 1}$ and $K_{\alpha 2}$) so that the diffraction spectrum for each lattice constant will typically shows two resolved (broad) peaks from $K_{\alpha 1}$ and $K_{\alpha 2}$ lines. Thus this measurement is usually used to roughly estimate the lattice constant and material composition of an epilayer. For a more accurate determination of these material parameters, the measurement of the double crystal x-ray rocking curve is necessary.

In DCXRD measurement, the incident x-ray is *filtered* by the Ge crystal (the first crystal) and the slit after the first crystal (as shown in Figure 7) removes the $K_{\alpha 2}$ reflection line. Thus, only the a more monochromatic $K_{\alpha 1}$ line will reach the second crystal (the sample). The linewidth of the $K_{\alpha 1}$ line depends strongly on the crystalline quality of the first crystal (Ge). In general, a Ge crystal with extremely high quality is used so that the excitation line reaching the second sample is expected to be highly monochromatic. During measurements, the sample is rotated (θ) while the

Reproduced with permission of the copyright owner. Further reproduction prohibited without permission.

goniometer and the first crystal are fixed. This type of measurement is usually called a "*rocking curve*". The linewidth of the $K_{\alpha 1}$ reflection from the second crystal (the sample) reflects the crystalline quality of the sample more accurately. Thus, the linewidth of the double crystal x-ray rocking curve (DCXRC) is typically used to evaluate the relative crystalline quality of semiconductor materials. For epilayers whose lattice constants are nearly lattice-matched to the substrates, DCXRD is a useful way to resolve the reflection peaks from the epilayer and substrate and thus determine their lattice constant and material composition accurately.

Reproduced with permission of the copyright owner. Further reproduction prohibited without permission.

2-4-3 Hall effect measurements

1. Theory

By using Hall effect, we can determine the average resistivity, carrier concentration and mobility and the carrier type in a doped sample. Figure 8 shows the schematic diagram of the Hall effect measurement setup. As shown in the figure, an electric field is applied along the x-axis while a magnetic field is applied along the z-axis. For a p-type sample, the Lorentz force, e***v*** x ***B***, causes an average downward force on the holes, and the downward-directed current causes a piling up of holes at the bottom side of the sample, which in turn gives rise to an electric field ε_y. Since there is no net current along the y direction in the steady state, the electric field along the y axis (Hall field) exactly balances the Lorentz force. The relation between the Hall field (ε_H) and applied current density (J_x) and magnetic field (B_z) can be expressed by[9]

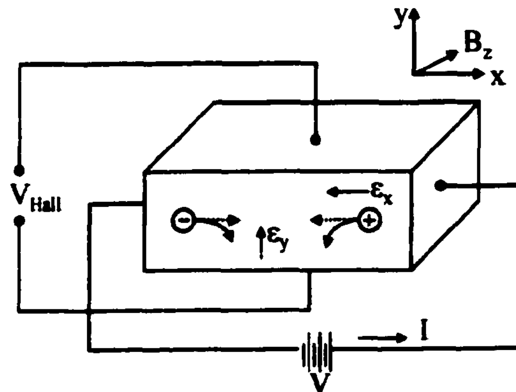

Figure 8 Schematic setup of Hall effect measurement.

Reproduced with permission of the copyright owner. Further reproduction prohibited without permission.

$$\varepsilon_H = R_H J_x B_z \quad (1)$$

where R_H is the Hall coefficient which can be obtained from the given J_x and B_z and the measured ε_H via Eq. (1).

When both holes and electrons are present in compensated samples, the expression that relates the free carriers and the Hall coefficient is:[10]

$$R_H = [(p - b^2 n) + (\mu_n B_z)^2 (p - n)] / e[(p + b n)^2 + (\mu_n B_z)^2 (p - n)], \quad (2)$$

where b is the mobility ratio ($b = \mu_n/\mu_p$), and μ_n and μ_p are electron and hole mobilities, respectively. This expression reveals that the Hall coefficient varies with applied magnetic field. For samples with modest mobility in the 100 to 1000 cm^2/Vs and with mobility ratios of $b \sim 3$ to 10, the Hall mobility coefficient is generally found to vary little with magnetic field.[10] For the case of $\mu_n B_z \ll 1$, Eq.(2) can be simplified to:[10]

$$R_H = (p - b^2 n) / e(p + b n)^2 \quad (3).$$

For highly doped samples without significant compensation effect (i.e. $n \gg p$ for n-type or $p \gg n$ for p-type) and with modest mobility ratios, Eq. (3) can be further simplified to[10]

$$R_H = r / (e\, p), \text{ for p-type} \quad [\text{or} \quad = -r / (e\, n), \text{ for n-type}] \quad (4),$$

where e is the elementary charge, and r is the scattering factor that lies

Reproduced with permission of the copyright owner. Further reproduction prohibited without permission.

between 1 and 2, depending on the scattering mechanisms in the semiconductor. Usually, r is assumed to be unity and this assumption generally introduces an error of less than 30%.[10] Thus, the carrier concentration can be determined via Eq. (4). The carrier type in the sample can be determined from the sign of Hall coefficient; i.e. n-type if R_H is negative and p-type if R_H is positive.

Moreover, the Hall mobility μ_H can also be obtained by[10]

$$\mu_H = |R_H| / \rho \tag{5}$$

where ρ is the resistivity of the sample which can be measured independently.

The magnetic filed (B_z) used for Hall effect measurements in our laboratory is fixed at 2.5 kG (= 0.25 T) and the samples studied in this thesis have relatively low electron mobilities μ_n in the range of 100 cm^2/Vs. This results in $\mu_n B_z \sim 10^{-3} - 10^{-2} << 1$ and thus Eq. (3) should be valid. For highly n-type doped $Zn_{1-x-y}Mg_xCd_ySe$ where n >> p and p-type doped $ZnSe_{1-x}Te_x$ with high Te content where p >> n, Eq. (4) can be used to determine the free carrier concentration. In this thesis, all values of free carrier concentration measured by Hall effect were determined from Eq. (4). It should be noted

Reproduced with permission of the copyright owner. Further reproduction prohibited without permission.

that for samples which contain significant carrier compensation, such as p-type doped $ZnSe_{1-x}Te_x$ alloys with low Te content, the use of Eq. (4) may introduce errors. More detailed characterization such as in high magnetic fields and/or magnetic field-dependent Hall effect measurements may be useful to determine their free carrier concentration more accurately.

2. Experimental details

Samples for Hall effect measurements are cut into 0.5cm x 0.5cm squares. Four contacts are placed on the corners of the square as shown on Figure 9. Ohmic contacts are essential for accurate Hall effect measurements. For samples with free carrier concentration of 10^{18} cm^{-3} or higher, ohmic contacts can be obtained by depositing In drops on the four corners. For samples with relatively low free carrier concentrations ($< 1 \times 10^{18}$ cm^{-3}), liquid Hg:In alloy drops were used as ohmic contact material on the four corners followed by an annealing at 300°C under a mixture of H_2 and N_2 for

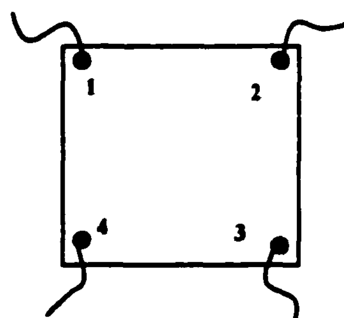

Figure 9 Van der Pauw Hall sample.

Reproduced with permission of the copyright owner. Further reproduction prohibited without permission.

3 min. After soldering gold wires on the contacts, the sample was then placed into the Hall effect setup. The operating magnetic field is fixed at 2.5 kG.

For resistivity measurements, eight voltage measurements are taken in the absence of magnetic field. The voltage sequence is shown in Table 1. After measuring these voltage values (in Volts), resistance can be calculated using Ohm's Law: $R_n = |V_n| / I$. For a perfect ohmic contact, the contact

Voltage Designation	*Current Applied between*	*Voltage Measured between*
V_1	1 – 2	4 – 3
V_2	2 – 1	4 – 3
V_3	2 – 3	1 – 4
V_4	3 – 2	1 – 4
V_5	3 – 4	2 – 1
V_6	4 – 3	2 – 1
V_7	4 – 1	3 – 2
V_8	1 – 4	3 – 2

Table 1 Sequence of voltage measurement for determination of resistivity.

resistance obtained from two oppositely applied currents (such as R_1 and R_2) should be equal. The average resistance between a pair of contacts will be $R = \Sigma^8_{n=1} R_n /8$. Then resistivity can be determined via[10],

$$\rho = F \pi t R \, 10^{-4} / \ln 2 \tag{6},$$

where t is the sample thickness in μm and F is the van der Pauw factor

Reproduced with permission of the copyright owner. Further reproduction prohibited without permission.

(symmetry factor). The van der Pauw factor F can be approximately obtained by[10]

$$F = 1 - \ln 2\,[(R_b-R_a)/(R_b+R_a)]^2/2 - [(R_b-R_a)/(R_b+R_a)]^4[(\ln 2)^2/4 - (\ln 2)^3/12] \quad (7)$$

where $R_a=(R_1+R_2)/2$ and $R_b=(R_3+R_4)/2$, the average resistance of a pair of contacts.

For the determination of carrier type, mobility and the carrier concentration, we need to measure the Hall coefficient. The measurements for the Hall coefficient are taken in the presence of a 2.5 kG magnetic field with + and – fluxes and the voltage measurement sequence is shown in Table 2. Once the voltages (in Volts) are measured, the average voltage for each configuration can be obtained: $V_{1F} = (V_9 - V_{10}) / 2$ and $V_{1R} = (V_{11} - V_{12}) / 2$. The other set of average voltages (V_{2F} and V_{2R}) are similarly defined. Then the Hall voltage for each configuration is $V_{H1} = (V_{F1} - V_{R1}) / 2$ and $V_{H2} = (V_{F2}$ -

Voltage Designation	*Flux*	*Current Applied between*	*Voltage Measured between*
V_9	+*B*	1 – 3	2 – 4
V_{10}	+*B*	3 – 1	2 – 4
V_{11}	-*B*	1 – 3	2 – 4
V_{12}	-*B*	3 – 1	2 – 4
V_{13}	+*B*	2 – 4	1 – 3
V_{14}	+*B*	4 – 2	1 – 3
V_{15}	-*B*	2 – 4	1 – 3
V_{16}	-*B*	4 – 2	1 – 3

Table 2 Sequence of voltage measurement for determination of Hall coefficient.

Reproduced with permission of the copyright owner. Further reproduction prohibited without permission.

V_{R2}) / 2. The average Hall coefficient can be obtained by

$$R_H = 10\, t\, (V_{H1}+V_{H2}) / (2\, I\, B) \quad (8),$$

where t is the sample thickness in μm, B is the magnetic flux in kG, and I is the current in A. If R_H is negative, the carriers are n-type. If R_H is positive, the carriers are p-type. After the R_H is determined, the carrier concentration and Hall mobility can be obtained via Eq. (4) and Eq. (5), respectively.

Reproduced with permission of the copyright owner. Further reproduction prohibited without permission.

2-4-4 Electrical and electrochemical capacitance-voltage profiling

Information of the free carrier or net carrier concentration is important for the study of doping in semiconductors. Although the doping concentration is related to the resistivity, it is sometimes not derived from resistivity measurements but is measured independently. Typically, the free electron concentration of n-type ZnSe-based wide bandgap II-VI materials can be determined from the Hall effect measurement while p-type net acceptor concentration (N_A-N_D) is usually obtained from the capacitance-voltage (C-V) characteristics due to the formation of a Schottky barrier instead of an ohmic contact at the contact-semiconductor interface. In III-V materials the free hole (electron) concentration measured by Hall effect is usually nearly equal to the net acceptor (donor) concentration determined from C-V curves at room temperature because donors and acceptors are totally ionized. However, for wide bandgap materials, these two values may not be identical.[11] For example, the ionization energy of nitrogen in p-type ZnSe is about 110 meV, four times larger than kT at room temperature, so that the free hole concentration in the valence band should be significantly

Reproduced with permission of the copyright owner. Further reproduction prohibited without permission.

smaller than the net acceptor concentration[11]. Besides the binding energy, other factors such as compensation mechanisms may also affect the ionization rate of acceptors or donors.[12]

In this section, we will focus on the introduction of two characterization methods: electrical C-V and electrochemical C-V (EC-V) techniques used to determine the (N_A-N_D) level of N doped ZnSe-based II-VI materials in this thesis. General information about the theory of C-V characterization and some factors affecting accuracy of these measurements will be addressed first.

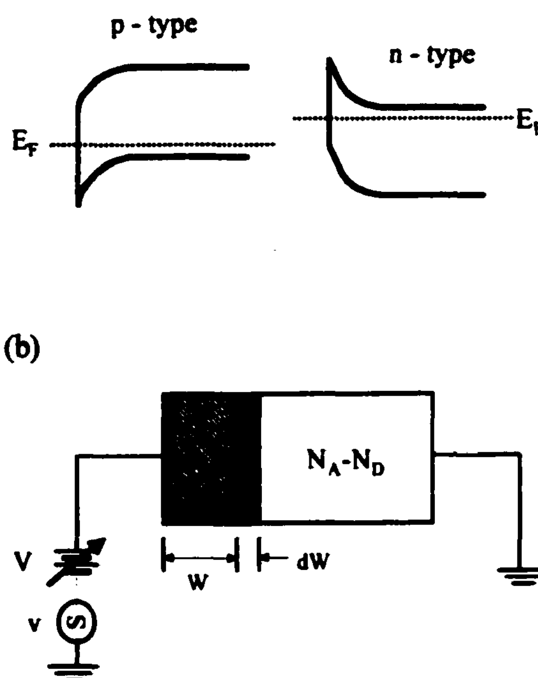

Figure 10 (a) Schematic diagrams of n-type and p-type contact-semiconductor Schottky barrier. **(b)** Schematic diagram of the contact-Semiconductor interface region while a reverse bias is applied.

1. Theory

The C-V technique relies on the fact that the width of a space-charge region (scr) of a semiconductor junction device

Reproduced with permission of the copyright owner. Further reproduction prohibited without permission.

depends on the applied reverse-biased voltage. The profiling method used in this thesis is to apply Schottky barrier diodes [shown in Figure 10(a)] by using a metal or a liquid electrolyte contact. A reverse bias will produce a scr whose boundary is gradual or fuzzy. For the evaluation of carrier concentration, we need to idealize the boundary of the scr to be perfectly sharp with a width of W as shown in Figure 10(b). Besides this, the effect of minority carriers is neglected and the region beyond W is of perfect charge neutrality. These assumptions are known as the "depletion approximation".[10,15] By assuming the depletion approximation, we can consider this reverse-biased junction as a parallel plate capacitor, its capacitance can be expressed as $C = \varepsilon A/W$ and thus,[10]

$$C = \varepsilon A/W = -dQ_s/dV \qquad (1)$$

where ε is the dielectric constant, Q_s is the semiconductor charge and A is the contact area. To measure the capacitance, we can superimpose a small-amplitude ac voltage v on a dc voltage V when the dc bias V is applied to the contact side. The ac voltage typically varies at a high frequency, such as 1 MHz and 3 kHz, with amplitude of 10 to 20 mV. In fact, the ac frequency affects the accuracy of C-V measurements for ZnSe-based II-VI materials

Reproduced with permission of the copyright owner. Further reproduction prohibited without permission.

grown on GaAs substrate and it will be discussed below.

For the p-type case, let us consider a diode to be biased to dc voltage V plus a sinusoidal ac voltage. Assume the ac voltage increasing from zero to a small positive voltage and adding a charge increment dQ_m to the contact. The charge increment dQ_m must be balanced by an equal semiconductor charge increment dQ_s for overall charge neutrality, where dQ_s is given by

$$dQ_s = -eA(N_A-N_D)dW \quad (2)$$

so that,

$$dQ_s/dV = -eA(N_A-N_D)(dW/dV) \quad (3).$$

By differentiating Eq. (1) and substituting dW/dV into Eq. (3), the doping concentration can be determined by

$$(N_A-N_D) = 2/e\varepsilon A^2[d(1/C^2)/dV] \quad (4).$$

The net acceptor concentration thus can be obtained from a $1/C^2$ - V curve by taking the slope $d(1/C^2)/dV$. Since the area appears as A^2 in Eq. (4), it is very important that the contact area should be precisely defined for an accurate concentration. After the capacitance has been measured, the scr width (W) can also be obtained via the Eq. (1). For p-type ZnSe epilayers

Reproduced with permission of the copyright owner. Further reproduction prohibited without permission.

grown on p-type GaAs substrates, the equivalent electrical circuit of the resulting structure consists of two barriers: a Schottky barrier (SB) diode formed at the contact/p-ZnSe junction, and a p-ZnSe/p-GaAs hetero-junction (HJ). Because of a large valence band discontinuity in the heterojunction (>1 eV) there is a depletion region on the wide band gap side, i.e., in the ZnSe:N region, as shown in Figure 11. This type of structure shows a back to back diode behavior. Thus, the measured capacitance includes two sources; one from the Schottky barrier (C_{SB}) and the other from the heterojunction (C_{HJ}). The schematic cross-sectional view of the device is drawn in Figure 12(a) and the equivalent circuit used to model this device is shown in Figure 12(b). Thus the total C_{HJ} can be expressed as

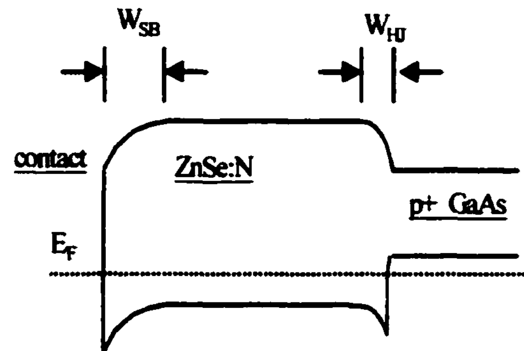

Figure 11 Schematic diagram of the band structure of a ZnSe:N sample grown on p^+ GaAs for C-V measurement.

$$C_{HJ}^{tot} = C_{HJ}^{0} + C_{HJ}^{1} + C_{HJ}^{2} + \ldots + C_{HJ}^{n} \quad (5),$$

where n is the number of spreading current paths [illustrated by arrows in Figure 12(a)]. Thus, the measured capacitance should be

Reproduced with permission of the copyright owner. Further reproduction prohibited without permission.

$$C_M = C_{SB}C_{HJ}^{tot} / (C_{SB} + C_{HJ}^{tot}) \quad (6).$$

It has been observed that the total HJ capacitance increases dramatically with decreasing ac frequency. Marshall et al[11] has reported that at high frequency, such as 1 MHz, only the region of the HJ directly under the SB contact can contribute to the capacitance significantly. In this high frequency limit, the derivative of 1/[Eq. (6)]^2 can be simplified as[13]

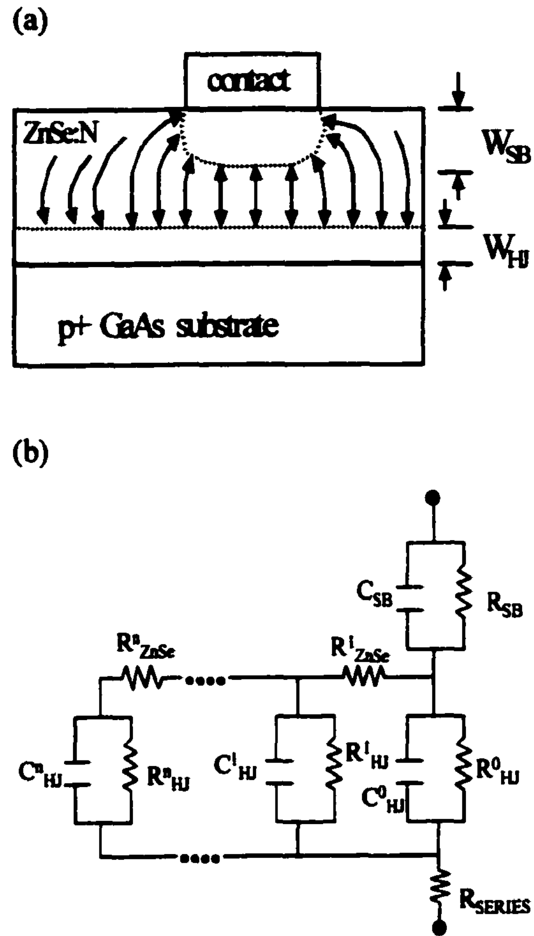

Figure 12 (a) Schematic cross-sectional view of the ZnSe:N device for C-V measurements. The arrows indicate a flow of current in the ZnSe:N region. **(b)** Equivalent circuit for modeling the device in (a).

$$d(1/C^2_M)/dV = (1 + C_{SB}/C_{HJ0})\, d(1/C^2_{SB})/dV \qquad (7)$$

where C_{HJ0} denotes the HJ capacitance corresponding to the area of SB only.

If we substitute Eq. (7) into Eq. (4), then the measured $(N_A\text{-}N_D)$ will be

$$(N_A\text{-}N_D)_{Measured} = (N_A\text{-}N_D)_{SB}/(1 + C_{SB}/C_{HJ0}) \qquad (8),$$

Reproduced with permission of the copyright owner. Further reproduction prohibited without permission.

where the $(N_A\text{-}N_D)_{SB}$ represents the real value. Thus, the measured net acceptor concentration at high frequency (e.g. 1MHz) will be *lower* than the real net acceptor concentration $(N_A\text{-}N_D)_{SB}$.

When a relatively low ac frequency is applied, such as 3 kHz, the spreading current becomes significant illustrated by the curved arrows in Figure 12(a).[12] The entire HJ depletion region contributes to the total HJ capacitance so that $C_{HJ}^{tot} >> C_{SB}$ resulting in $C_M \sim C_{SB}$ according to Eq. (6). Thus, the measured net acceptor concentration by Eq. (4) will be close to the real value. Table 3 lists measured $(N_A\text{-}N_D)$ levels of several nitrogen doped ZnSe and ZnMgSe samples grown on GaAs substrates. These levels were determined from electrical and electrochemical C-V curves with various ac

Samples	Electrical C-V				Electrochemical C-V
	1k Hz	*3.2k Hz*	*100k Hz*	*1M Hz*	*3.2k Hz*
ZnSe:N (1)	5×10^{17}	4.6×10^{17}	2.4×10^{17}	1.7×10^{17}	2.5×10^{17}
ZnSe:N (2)	3.3×10^{17}	3.5×10^{17}	1.7×10^{17}	1.1×10^{17}	4.8×10^{17}
ZnMgSe:(N+Te) (1)	7.1×10^{17}	7×10^{17}	4×10^{17}	1×10^{17}	6×10^{17}
ZnMgSe:(Te+N) (2)	----	3.5×10^{17}	1.5×10^{17}	1.3×10^{17}	2.4×10^{17}

Table 3 List of measured $(N_A\text{-}N_D)$ levels for several nitrogen-doped samples grown on GaAs. The levels were determined by the C-V curves using different ac frequencies.

Reproduced with permission of the copyright owner. Further reproduction prohibited without permission.

frequencies. As listed in Table 3, the measured (N_A-N_D) level decreases with the increase of ac frequency which is consistent with the model above. Due to the concern for accuracy, the (N_A-N_D) levels of the p-type samples in the following studies were all determined from the C-V curves measured with an ac frequency of 3 kHz.

It should be mentioned that the depletion approximation is generally a reasonable approximation for most cases when the scr is reverse biased.[10,15] For p-type samples with significant carrier compensation and relatively large ionization energies of acceptors, the effect of minority carriers (i.e. electrons) on the scr may introduce significant errors to the depletion approximation. When the effect of minority carriers becomes important in the scr, a plot of $1/C^2$ against the applied dc voltage is no longer linear (the slope of $1/C^2$ curve may vary with applied dc voltages).[15] The correction for this effect is complicated and beyond the topic of this thesis. In this thesis, we used Eq. (4), by assuming the depletion approximation, to determine the (N_A-N_D) values for nitrogen doped samples. It should be noted that errors may be present in the (N_A-N_D) values.

Reproduced with permission of the copyright owner. Further reproduction prohibited without permission.

2. Electrical C-V characteristics

For an electrical C-V measurement, a Au dot with diameter of 600 μm and thickness of about 100 nm is evaporated on the clean surface of a p-type sample. Indium on the p+ GaAs substrate side is used as an ohmic contact. A dc voltage varied from –2 to 2 V is applied on the Au (SB) contact while the ohmic contact (substrate side) is grounded. The capacitance is measured by superimposing a small-amplitude ac voltage *v* on a dc voltage. The ac voltage varies at a frequency of 1 MHz, 100 kHz, or 3.2 kHz. Net acceptor concentrations are determined by taking the slope of the $1/C^2$ curve versus dc V and substituting the slope into Eq. (4). In general, a net acceptor concentration measured at lower ac frequency is higher and more accurate than that measured at higher ac frequency as listed in Table 3. Figure 13 shows an example of typical C-V and $1/C^2$-V curves of nitrogen doped ZnSe measured at ac frequency of 3 kHz.

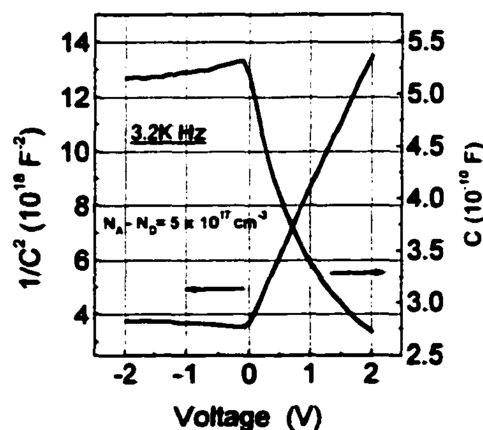

Figure 13 Capacitance-voltage and $1/C^2$–V curves of a ZnSe:N sample measured with 3.2 kHz ac frequency.

Reproduced with permission of the copyright owner. Further reproduction prohibited without permission.

By Eq. (4), the (N_A-N_D) level of this sample has been calculated to be about 5×10^{17} cm^{-2}.

3. Electrochemical C-V characteristics

The electrochemical C-V profiling technique, including C-V and depth (etch) profiling, is based on making a liquid electrolyte-semiconductor Schottky contact and measuring the capacitance at a constant dc voltage rather than at the various ones in the case of electrical C-V profiling. It has

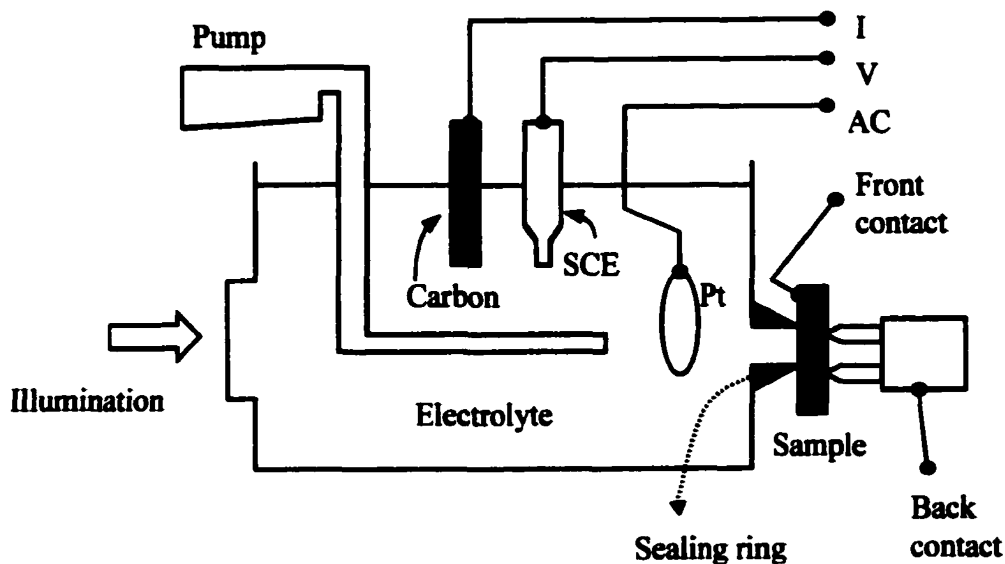

Figure 14 Schematic diagram of the electrochemical cell showing the Pt, saturated calumel electrode (SEC), carbon electrode, and the pump used to agitate the electrolyte and disperse bubbles on the semiconductor surface.

Reproduced with permission of the copyright owner. Further reproduction prohibited without permission.

the capability to characterize the capacitance as a function of depth into the layer in steps as small as 0.005 μm. This is useful for the study of modulation doped structures such as δ-doping or multiple layer structures. The depth profiling is achieved by electrolytically etching the semiconductor between capacitance measurements. Figure 14 shows the schematic diagram of the Bio-Rad PN4200 EC-V profiler. The sample is mounted and pressed against a well-defined sealing ring in the electrochemical cell that contains an electrolyte. The opening of the sealing ring defines the electrolyte contact area of approximately 0.1 cm^2 by means of the four spring-loaded back contacts pressing the sample against the PVC sealing ring as shown in Figure 14. Either a back contact on the substrate side (the four spring-loaded contacts) or a front contact on the epilayer side can be used for the C-V profiling. In general, for samples grown on semi-insulating substrates, the ECV profiling should be performed by using the front contact method. For a highly doped (conductive) sample, a sufficiently good ohmic contact can be obtained by applying a 40 V ac voltage for a duration of 150 ms between the spring loaded wires of the front contact or two of four back contact pins. For samples with low doping level, extra preparation, such as depositing In:Hg

Reproduced with permission of the copyright owner. Further reproduction prohibited without permission.

alloy drops with annealing at 300 °C, is necessary for obtaining an ohmic front contact. The detailed preparation of the In:Hg alloy contact has been described in the Hall effect section.

The etching and measuring conditions are controlled by the potential across the cell. This is established by passing a dc current between the semiconductor and the carbon electrode to maintain the required potential measured with respect to the saturated calomel electrode (SCE). To reduce series resistance, the ac voltages are measured with a platinum electrode located near the sample. The typical measuring potentials with respect to the SCE are normally between –1.5 and 0 V for p-type materials which are smaller than the breakdown voltage. This avoids any depth error if there is a leakage current through the ZnSe film. It has been reported that NaOH (1M) : Na_2SO_3 (1.25M) solution can be used as the EC-V electrolyte for n- and p-type ZnSe-based samples.[14] The depth profiling is mainly controlled by the etching current. The etching rate is proportional to the etching current. The etched depth is calibrated by the use of an Alpha-Step 200 surface profiler which is used to measure the crater depth after the profiling. Several problems usually arise during the EC-V profiling, which are:

Reproduced with permission of the copyright owner. Further reproduction prohibited without permission.

1. a poor electrolyte-semiconductor Schottky barrier,
2. preferential dissolution at the defect areas,
3. too high or too low electrochemical etch rates,
4. formation of insoluble or non-metal products on the etch surface,
5. a rough bottom of the etch crater.

The first problem can be prevented by cleaning the surface of samples with acetone before the measurements. In the depth profiling of Mg- and Be-based II-VI materials, samples usually experience preferential dissolution at defect areas. This creates deep holes going through to the conductive GaAs substrates. When this happens, the etching current and the measured carrier concentration will increase irregularly but there is no real etching of the layer. A fast etching with high applied etching voltage has been found to make this problem worse. Thus, a low etching current (~0.05 A, corresponding to a slow etching rate and a low applied etching voltage) and a thick epilayer (>1.5 μm) are preferred for reducing the preferential dissolution of defects. In addition, for the optimum conditions, a blue light illumination on the etch area is useful. A blue illumination can speed up the

Reproduced with permission of the copyright owner. Further reproduction prohibited without permission.

etching without an increase of the applied etching voltage so that a lower voltage is applied for a specific etching rate (current). We have successfully achieved the EC-V profiling for Mg- and Be- based II-VI materials by these optimum conditions.

When a non-metal product, such as a Se residue for Se-based materials, is formed on the etch surface, the etching current will decrease quickly and the C-V measurement will be affected. This may also result in a non-uniform etching so that a rough etch crater may form. The Se-residue can be resolved by the presence of SO_3^{-2} ion in the electrolyte. Improper etching conditions such as too fast etching can cause a rough crater bottom while the bottom of the etch crater after profiling may appear rough because of the residues of the solution left in the crater. Boiling the samples before and after the profiling in acetone and applying a reasonable etching rate will reduce these problems and a well-defined crater can be obtained. The EC-V profiling technique will be used to determine the depth-dependent (N_A-N_D) levels for most of p-type doped samples including modulation-doped samples.

Reproduced with permission of the copyright owner. Further reproduction prohibited without permission.

Chapter 3

Bipolar Doping of $Zn_{1-x-y}Mg_xCd_ySe$ Alloys

3-1 n-type doping of $Zn_{0.51}Cd_{0.49}Se$ and $Zn_{1-x-y}Mg_xCd_ySe$ alloys lattice-matched to InP using $ZnCl_2$

For the fabrication of light emitting diodes (LEDs) and diode lasers, effective p-type and n-type doping of cladding and waveguide layers is essential. Typically, a doping level in the range of 10^{17} cm^{-3} or higher is required for high performance devices. The achievement of n-type doping of lattice-matched $Zn_{0.51}Cd_{0.49}Se$ and $Zn_{1-x-y}Mg_xCd_ySe$ layers with various bandgap energies will be reported in this section.

Chlorine as a substitutional atom on a Se site can form a shallow donor in ZnSe. It has been reported that Cl doped ZnSe can approach a free electron concentration as high as 3 x 10^{20} cm^{-3}.[1] Here we used chlorine, obtained from $ZnCl_2$, as the n-type dopant for $Zn_{0.51}Cd_{0.49}Se$ and $Zn_{1-x-y}Mg_xCd_ySe$ alloys lattice-matched to InP. Hall effect measurement was applied to characterize the electrical properties including free electron

Reproduced with permission of the copyright owner. Further reproduction prohibited without permission.

concentration and mobility of these Cl doped samples. Photoluminescence (PL) was used to study their optical property at 10 K.

Semi-insulating InP (001) substrates (Sumitomo Electric) were used for the epitaxial growth of these n-type layers. The ex-situ and in-situ substrate preparation procedures were described in Chapter 2.[2,3] An 80 nm lattice-matched InGaAs buffer layer doped with Be (InGaAs:Be, p-type) was grown at 480 °C on the deoxidized surface. For comparison, Cl doped $Zn_{0.51}Cd_{0.49}Se$ layers lattice-matched to InP were also grown without the InGaAs:Be buffer layer. All the $Zn_{1-x-y}Mg_xCd_ySe$ quaternary layers were grown with the III-V buffer layer.

The growth conditions of lattice-matched $Zn_{0.51}Cd_{0.49}Se$ and $Zn_{1-x-y}Mg_xCd_ySe$ quaternaries on InP are the same as described in Chapter 2. For example, the beam equivalent pressure (BEP) ratio of Cd to Zn was kept at 2 for the growth of $Zn_{0.51}Cd_{0.49}Se$ and at 1.6 for the quaternaries. A low-temperature $Zn_{0.51}Cd_{0.49}Se$ buffer was also grown at 170 °C for 1 min. It was followed by about 4 min interruption of growth during which the substrate temperature was raised to the desired growth temperature of 270 °C. Then the $Zn_{0.51}Cd_{0.49}Se$ or $Zn_{1-x-y}Mg_xCd_ySe$ layer doped with Cl was grown. The typical growth rate was about 1 μm/hr.

Reproduced with permission of the copyright owner. Further reproduction prohibited without permission.

Chlorine was provided by a solid $ZnCl_2$ source heated in a Knudsen effusion cell. The $ZnCl_2$ cell temperature was varied from 60 °C to 90 °C for different doping levels. Due to the ease of oxidization of active Mg atoms, 10 nm ZnSe:Cl was grown as a protection cap layer on the Cl doped $Zn_{1-x-y}Mg_xCd_ySe$ layer. All samples have thickness of 1.5-2.0 μm to ensure reliable Hall effect measurements. Liquid Hg:In alloy drops were used as the ohmic contact material on the four corners of the square followed by an annealing at 300 °C under a mixture of H_2 and N_2 for 3 min as described in Chapter 2. After soldering the gold wires on the contacts, the sample was then placed into a 2.5 kG magnetic field followed by the characterization of the electrical properties by Hall effect measurement at room temperature. In order to prevent the electrical conductivity of the InGaAs buffer layer from interfering with our measurements, the III-V (InGaAs) buffer layer was doped p-type with Be. Figure 1 shows the results of the electrical characterization of the Cl doped $Zn_{0.51}Cd_{0.49}Se$ with various $ZnCl_2$ cell temperatures. Two sets of samples were grown, one with the $Zn_{0.51}Cd_{0.49}Se$ grown directly on InP substrates and another with the InGaAs:Be buffer layer.

Figure 1(a) shows the free electron concentration (n) as a function of the reciprocal of the $ZnCl_2$ cell temperature. The $ZnCl_2$ cell temperature was

Reproduced with permission of the copyright owner. Further reproduction prohibited without permission.

varied from 60 to 90 °C. As shown in the figure, the n-type doping efficiency in the samples with the InGaAs:Be buffer layers is significantly higher that those without the buffer layers. It is expected that good crystalline quality is essential for optimum doping efficiency. In fact, the introduction of the InGaAs buffer layer improved the crystalline quality of the $Zn_{0.51}Cd_{0.49}Se$ and quaternary epilayers as confirmed by lower etch pit (stacking fault) densities and narrower x-ray diffraction peaks.[2,3]

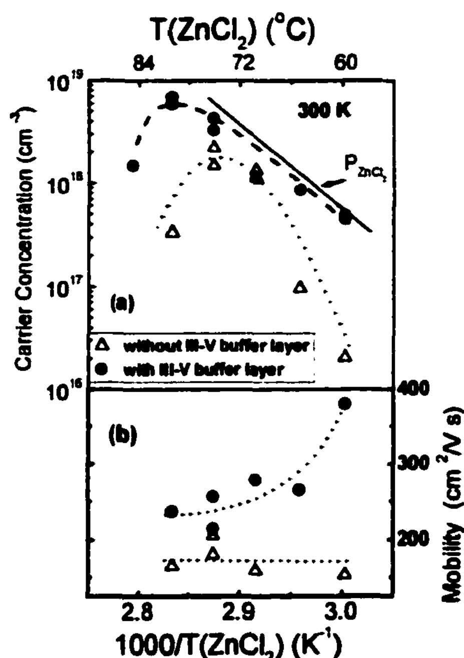

Figure 1(a) Free electron concentration of Cl doped $Zn_{0.51}Cd_{0.49}Se$ grown with and without an InGaAs:Be buffer layer as a function of $ZnCl_2$ cell temperature. The solid line is the $ZnCl_2$ vapor pressure in arbitrary units. **(b)** Hall mobility of Cl doped $Zn_{0.51}Cd_{0.49}Se$ grown with and without InGaAs:Be buffer layer as a function of $ZnCl_2$ cell temperature. Both (a) and (b) are measured at room temperature.

The maximum free electron concentration of $Zn_{0.51}Cd_{0.49}Se$:Cl is 7 x 10^{18} cm^{-3} with a mobility of 240 cm^2/Vs achieved with the $ZnCl_2$ cell temperature at 80 °C. Before reaching the maximum, the concentration proportionally increases as the reciprocal of the $ZnCl_2$ cell temperature decreases and has the same slope as the $ZnCl_2$ vapor pressure as shown in Figure 1(a). This implies that the free electron concentration of $Zn_{0.51}Cd_{0.49}Se$:Cl epilayers is

Reproduced with permission of the copyright owner. Further reproduction prohibited without permission.

proportional to the amount of chlorine incorporated in the layer. By contrast the set of samples grown without the InGaAs:Be buffer layer reaches a maximum concentration of only 2 x 10^{18} cm^{-3} and the value of n decreases somewhat faster than the $ZnCl_2$ vapor pressure as the $ZnCl_2$ cell temperature was reduced. This observation suggests that the activation of the Cl dopant is not complete in these samples possibly due to additional compensation effects.

Figure 1(b) compares the Hall mobility at room temperature versus the reciprocal of Cl cell temperature ($1/T_{ZnCl2}$) for $Zn_{0.51}Cd_{0.49}Se$:Cl grown with and without the InGaAs:Be buffer layer. The mobility of $Zn_{0.51}Cd_{0.49}Se$:Cl grown with the buffer layer decreases from 380 cm^2/Vs (for 5 × 10^{17} cm^{-3}) to 200 cm^2/Vs (for 5 × 10^{18} cm^{-3}) as $1/T_{ZnCl2}$ decreases (or increase of impurity concentration) while the mobility of the samples without the buffer layer remains nearly constant at a low value of 150-200 cm^2/Vs. In general, assuming a good crystalline quality, carrier mobility in compound semiconductors is mainly dominated by three principal scattering mechanisms which are phonon scattering, ionized impurity scattering, and alloy scattering. At low temperature, phonon scattering dominates the carrier transport.[51] At room temperature and high doping level, assuming most of carriers are ionized, the phonon scattering may be screened so that it is

Reproduced with permission of the copyright owner. Further reproduction prohibited without permission.

reduced and the ionized impurity scattering becomes dominant.[52] For alloy samples with the same material composition, the effect from the alloy scattering should be a constant. Thus, the decrease of mobility with the decrease of $1/T_{ZnCl2}$ (or increase of impurity concentration) in Figure 1(b) should be due to the increased ionized impurity scattering in the samples.

For samples with poor crystalline quality, structural defects such as stacking faults or dislocations, may seriously impede carrier transport and thus limit the carrier mobility. A low and constant mobility, as shown in Figure 1(b), for the samples without the InGaAs:Be buffer layer suggests that a defect related scattering mechanism is dominant in these samples. The difference between the mobilities of the two sets of samples in Figure 1(b) becomes smaller when the Cl cell temperature is higher (or impurity concentration is higher). This suggests that ionized impurity scattering becomes comparable to the defect scattering at higher doping levels.

A series of Cl doped $Zn_{1-x-y}Mg_xCd_ySe$ quaternary layers lattice-matched to InP having a 77K bandgap of about 2.74 eV was also grown with various $ZnCl_2$ temperatures. Figure 2 compares the results presented above for $Zn_{0.51}Cd_{0.49}Se$ with those obtained for the quaternary layers. Both sets of samples are grown with InGaAs:Be buffer layers. In spite of the significantly higher bandgap energy of the quaternary than that of $Zn_{0.51}Cd_{0.49}Se$ (77K E_g=

Reproduced with permission of the copyright owner. Further reproduction prohibited without permission.

2.17 eV) due to the introduction of Mg atoms, there is not a large difference in the value of free electron concentration that can be obtained for the two materials, as seen in Figure 2. High doping levels (3×10^{18} cm^{-3}) were also achieved for the quaternary with Hall mobility of about 230 cm^2/Vs.

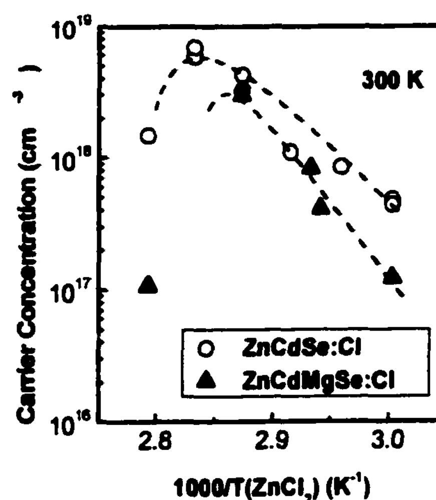

Figure 2 Comparison of the free electron concentration of Cl-doped $Zn_{1-x-y}Mg_xCd_ySe$ (with a 77 K bandgap of 2.74 eV) as a function of the reciprocal of $ZnCl_2$ cell temperature with that of Cl-doped ZnCdSe. Both sets of samples are grown with InGaAs:Be buffer layers.

In the two materials, after reaching the maximum, the free electron concentration decreases abruptly when the $ZnCl_2$ cell temperature is increased further. This suggests that beyond a point, the incorporated Cl atoms do not act as donors. This behavior is similar to that observed in Cl doped ZnSe[4,5] and it could result from the formation of deep, compensating acceptor complexes, or reaching the solubility limit.[6,7]

In order to understand the electrical properties of these materials, it is useful to plot the Hall mobility versus carrier concentration in a log-log scale. The data for the ternary and quaternary samples of Figure 2 are plotted this way in Figure 3. As previously discussed, the room temperature mobilities

Reproduced with permission of the copyright owner. Further reproduction prohibited without permission.

for $Zn_{0.51}Cd_{0.49}Se$ decrease with increasing doping level due to effective ionized impurity scattering at room temperature. Although only limited mobility data are available for the quaternary, Figure 3 also indicates a lower mobility at low carrier concentrations for the $Zn_{1-x-y}Mg_xCd_ySe$ quaternary than for the ternary. The Hall mobility for $Zn_{1-x-y}Mg_xCd_ySe$ remains nearly constant as a function of carrier concentration. It is proposed that an additional scattering mechanism (possibly increased alloy scattering in the quaternary alloy) may be limiting the mobility of this material in particular at low carrier concentrations.

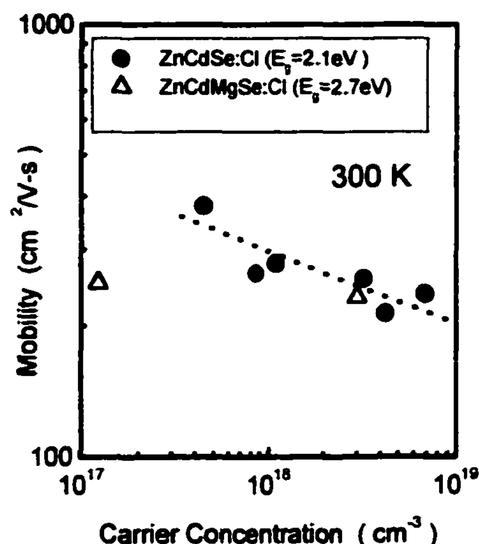

Figure 3 Hall mobility of ZnCdSe:Cl and ZnMgCdSe:Cl (with a 77 K bandgap of 2.74 eV) as a function of free electron concentration. Hall measurements were performed at room temperature.

A series of lattice-matched Cl doped quaternary layers were grown having various compositions (and bandgaps) using a $ZnCl_2$ cell temperature that gives maximum doping levels. The free electron concentration of these samples is plotted as a function of the quaternary bandgaps in Figure 4. The maximum free electron concentration decreases as the 77K bandgap energy

Reproduced with permission of the copyright owner. Further reproduction prohibited without permission.

(or Mg concentration) increases, as shown in Figure 4. It has been observed that the maximum achievable free electron concentration in II-VI materials is determined only by the energy difference between the conduction band minimum (CBM) and the Fermi level pinned by a universal compensation center in an absolute energy scale.[5,8] Similar decrease with the increase of bandgap has been reported for Cl doping of $Zn_{1-x}Mg_xSe$.[5] In that study, this behavior was explained as reflecting the fact that the increase in the bandgap of the ternary with addition of Mg results in an increase of only the CBM relative to ZnSe.[9] However, the rate of change of the maximum free electron concentration with bandgaps in our study is much smaller than the one reported for $Zn_{1-x}Mg_xSe$.[5] A possible explanation for the results in Figure 4 is that in our materials, unlike the ternary $Zn_{1-x}Mg_xSe$, the introduction of Mg atoms in the quaternary, simultaneously with a slight reduction in Cd to maintain the lattice-matching condition, does not only increase the CBM relative to that

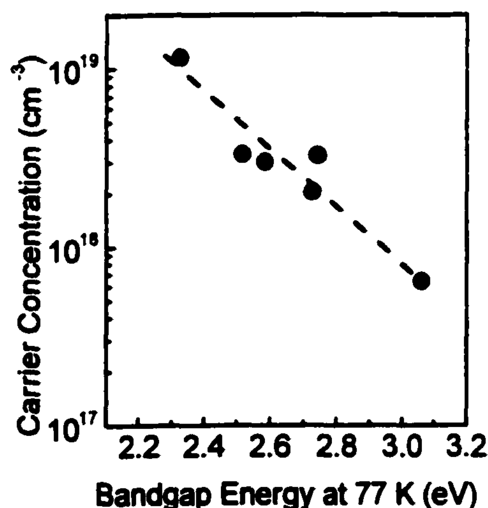

Figure 4 Dependence of maximum free-carrier concentration on the 77K bandgap for Cl-doped $Zn_{1-x-y}Mg_xCd_ySe$ quaternary layers.

Reproduced with permission of the copyright owner. Further reproduction prohibited without permission.

of lattice-matched $Zn_{0.51}Cd_{0.49}Se$, but also lowers the valence band maximum (VBM). Another factor that may result in the decrease observed in Figure 4 is a reduction of solubility of chlorine with increasing bandgaps.[6]

The 10 K PL spectra for latticed-matched $Zn_{0.51}Cd_{0.49}Se$ and $Zn_{1-x-y}Mg_xCd_ySe$ layers doped at a level of 10^{18} cm^{-3} are shown in Figure 5. All the layers are about 1.5 μm in thickness. Strong PL emission originating from near band edge recombination is observed for all three samples. The width of the PL emission increases with increasing Mg content (and bandgap) as in the case of undoped quaternary layers.[3] No deep level emission was introduced by the chlorine impurity even at this high electron concentration (3 x 10^{18} cm^{-3}), confirming the good crystalline and good optical quality of these Cl doped $Zn_{1-x-y}Mg_xCd_ySe$ layers.

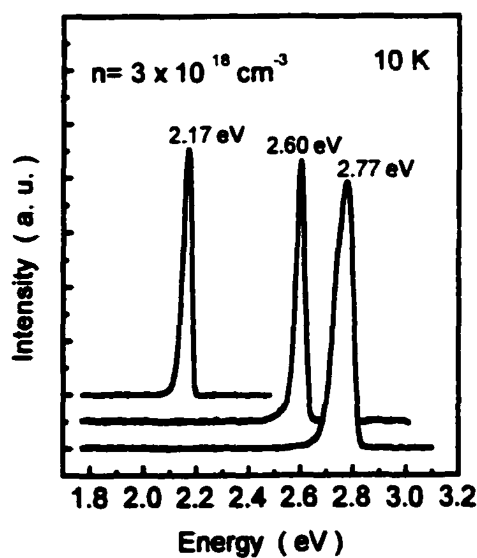

Figure 5 Photoluminescence spectra measured at 10 K for Cl-doped ZnCdSe and for two Cl-doped $Zn_{1-x-y}Mg_xCd_ySe$ layers of different compositions. All samples are lattice matched to InP and have a carrier concentration of 3 x 10^{18} cm^{-3}.

Reproduced with permission of the copyright owner. Further reproduction prohibited without permission.

3-2 Conventional p-type doping of $Zn_{1-x-y}Mg_xCd_ySe$ using an rf-discharge nitrogen plasma source

It is well known that Se-based II-VI materials are difficult to dope p-type while the p-type doping of Te-based ones is relatively easy. Since nitrogen was successfully incorporated as a shallow acceptor in ZnSe and produced a net acceptor concentration as high as 1×10^{18} cm^{-3}, it has become the most frequently used dopant for making p-type II-VI materials.[10] In this section, we apply a radio frequency (rf) discharge nitrogen plasma source for the p-type doping of lattice-matched $Zn_{0.51}Cd_{0.49}Se$ ternary and $Zn_{1-x-y}Mg_xCd_ySe$ quaternary alloys grown on (001) InP. Low temperature photoluminescence (PL) was used to investigate the optical properties of these nitrogen doped samples. Electrical capacitance-voltage (C-V) profiling was performed for the determination of carrier concentration. The capacitance as a function of applied dc voltage was measured between an Au contact on the sample surface and an In ohmic contact on the side of p^+ InP substrate as described in Chapter 2. The Au contact was obtained by depositing directly on the clean sample surface and its area was well defined (~0.3 mm^2).

The epitaxial growth procedures of the ternary and quaternary for the nitrogen doping are the same as those in the n-type doping. The nitrogen

Reproduced with permission of the copyright owner. Further reproduction prohibited without permission.

plasma source was controlled by the rf discharge power and pure nitrogen flow. In general, higher discharge power or larger nitrogen flow corresponding to higher background pressure in the growth chamber results in a higher nitrogen incorporation. However, it has been observed that too much nitrogen incorporation may cause serious carrier compensation in the Se-based II-VI materials. Therefore, an appropriate control of nitrogen source conditions including the rf discharge power and nitrogen flow is required for achieving optimum nitrogen incorporation in these materials.

Different nitrogen conditions were used including various rf discharge powers from 200 W to 400 W and various pure nitrogen flows corresponding to a background pressure from 1 x 10^{-6} to 1 x 10^{-5} Torr. In the growth of nitrogen doped $Zn_{1-x-y}Mg_xCd_ySe$, the quality of the growing surface is very sensitive to the nitrogen flow. For example, samples of $Zn_{1-x-y}Mg_xCd_ySe$:N grown with a high nitrogen flow, corresponding to the chamber background pressure of 8 x 10^{-6} Torr, usually show a high density of pits on the as-grown surface under Nomarski interference contrast microscope illumination while those with a low nitrogen flow show a shiny surface. In fact, the RHEED pattern of those samples with high nitrogen flow degraded from streaky to spotty during the growth. A spotty RHEED pattern suggests a rough growth front which indicates a three-dimensional

Reproduced with permission of the copyright owner. Further reproduction prohibited without permission.

growth mode. The observation of the RHEED degradation is consistent with the poor sample surface suggesting that too much nitrogen may hinder the growth of high quality $Zn_{1-x-y}Mg_xCd_ySe$. In the case of $Zn_{0.51}Cd_{0.49}Se$, the degradation in RHEED pattern was not observed while using high nitrogen flow.

Figure 6 shows the 7 K PL spectrum of a N doped $Zn_{1-x-y}Mg_xCd_ySe$ quaternary sample. The dominant peak at about 2.588 eV was assigned to the near bandedge emission while a broad peak at 2.49 eV was observed only when nitrogen was incorporated. This additional broad emission (about 100 meV below the near bandedge emission) may originate from a nitrogen-related emission such as donor-acceptor-pair (DAP) emission or a free-to-bound (FB) (conduction band to bound acceptor) suggesting that nitrogen has been incorporated in the quaternary. Figure 7 shows the C-V measurement result of another nitrogen doped quaternary (E_g = 2.5 eV). The sample was doped with an rf

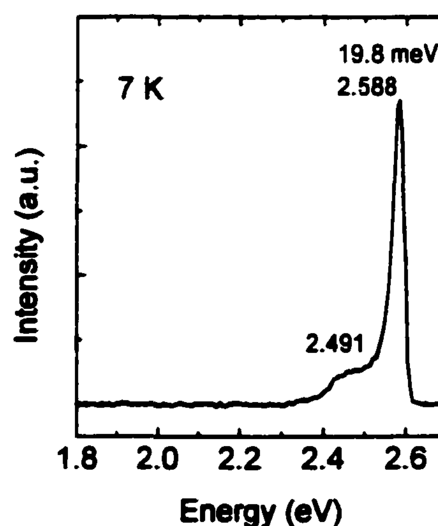

Figure 6 Photoluminescence spectrum of N doped ZnMgCdSe quaternary at 7K. The dominant peak at 2.588 eV is assigned to the near bandedge emission while the broad band at 2.491 eV is related to the nitrogen incorporation.

Reproduced with permission of the copyright owner. Further reproduction prohibited without permission.

discharge power of 400 W and chamber background pressure of 3 x 10^{-6} Torr. Under these doping conditions, the RHEED pattern remained streaky to the end of the growth suggesting a two-dimensional growth mode for this sample. The net acceptor concentration (N_A-N_D) was calculated to be 7 x 10^{15} cm^{-3} from the slope of the $1/C^2$ curve. A level higher than 1 x 10^{16} cm^{-3} could not be achieved by changing the nitrogen source doping conditions by increasing the rf discharge power and/or nitrogen flow.

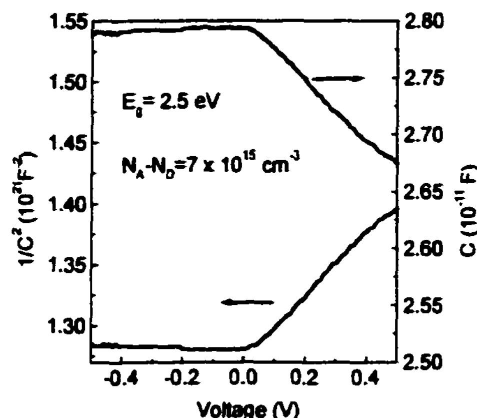

Figure 7 Capacitance-voltage (C-V) plot for a ZnMgCdSe quaternary layer with bandgap of 2.5 eV doped with nitrogen. The (N_A-N_D) level is 7 x 10^{15} cm^{-3}.

Nitrogen doping has also been performed in the lattice-matched $Zn_{0.51}Cd_{0.49}Se$ material using various nitrogen source conditions. Even though low temperature PL spectra show emissions associated with N incorporation, unusual C-V curves rather than those of typical p-type behavior were obtained. Furthermore, the results of electrochemical C-V profiling suggest that these samples are very resistive and their doping level could not be determined.

Reproduced with permission of the copyright owner. Further reproduction prohibited without permission.

The p-type doping difficulty in these $Zn_{1-x-y}Mg_xCd_ySe$ materials in comparison to ZnSe must be due to the addition of Cd and/or Mg atoms since the maximum achievable (N_A-N_D) level (~1 x 10^{16} cm^{-3}) of the quaternary is much less than that of ZnSe (~1 x 10^{18} cm^{-3}). In fact, studies of the p-type doping of other Se-based II-VI materials suggests that Cd and Mg may introduce some additional carrier compensation processes into nitrogen doped ZnSe materials, such as DX-like centers and nitride complexes. In order to understand this behavior, it is helpful to study the p-type doping behavior of $Zn_{1-x}Mg_xSe$ and $Zn_{1-y}Cd_ySe$ ternaries as a function of materials (Mg and Cd) concentration. In the next section, further studies in the p-type doping of these two ternaries as a function of composition, as well as the use of modulation doping techniques will be addressed.

In spite of the low (N_A-N_D) level (~1 x 10^{16} cm^{-3}) in the quaternary, the fabrication of light emitting diodes (LED) may be still possible as long as a p-type contact layer is achieved. Therefore, MBE growth and p-type doping of the ZnSeTe alloy lattice-matched to InP will be investigated. In chapter 4, the MBE growth of high quality ZnSeTe alloys with good compositional control will be reported, along with their p-type doping as a function of material composition.

Reproduced with permission of the copyright owner. Further reproduction prohibited without permission.

3-3 p-type doping issues of Se-based II-VI materials

Nearly all wide bandgap semiconductors exhibit difficulties with achieving good bipolar conductivity and tend to prefer one type of doping. Extensive studies over the last two decades have revealed many mechanisms that could result in doping difficulties. For example, the position of the valance band maximum (VBM) and the conduction band minimum (CBM) of semiconductors might be one factor to consider. Generally speaking, a lower CBM position on an absolute energy scale facilitates n-type doping, while higher VBM position is good for p-type doping.[13] ZnTe is known to have a higher VBM position than ZnSe on an absolute energy scale. It has been reported that ZnTe is more receptive to p-type doping with a reported free hole concentration[11] as high as 1 x 10^{20} cm^{-3} (using a discharge nitrogen source), while ZnSe can only achieve a net acceptor concentration[12] (N_A-N_D) of 1 x 10^{18} cm^{-3} with a free hole concentration somewhat lower than that.[50] On the other hand, ZnSe has a lower CBM position than ZnTe on an absolute energy scale and it is highly receptive to n-type doping with a maximum reported free electron concentration of 3 x 10^{20} cm^{-3}, while only low n-type ZnTe has been obtained.[1]

The band structure is only one obvious consideration for the doping of wide bandgap semiconductors. For example, CdSe has a higher VBM

Reproduced with permission of the copyright owner. Further reproduction prohibited without permission.

position than ZnSe on an absolute energy scale, but high p-type doping is much harder to achieve[49] suggesting that there may be other factors dominating its doping properties. Numerous studies over the past years have shown that the doping difficulties may result from the formation of several different defects, which cause carrier compensation. It has been observed that for wide bandgap materials carrier compensation becomes more likely as the bandgap increases.[14] This is believed to be because compensation defect formation is energetically more favorable when the value of the bandgap is large in comparison to the bond energies.[15] This characteristic of wide bandgap materials hinders the reliable operation of their laser diodes, and limits their feasibility as photonic device materials. Therefore, suppressing the compensation effects is of top priority for developing new optoelectronic devices made from II-VI wide bandgap materials. Finally, the solubility may be limiting the incorporation of the impurity and/or determining the way in which it is incorporated in the lattice, both of which will affect the maximum achievable doping levels.

In general, the proposed defects that limit the p-type doping of ZnSe:N, can be classified into several categories including 1) native defects, 2) complex defects involving impurities, 3) associated-impurity compensation centers, and 4) bond-breaking defects (DX-like centers). Table 1 lists some

Reproduced with permission of the copyright owner. Further reproduction prohibited without permission.

proposed defects that may limit the p-type doping of nitrogen doped ZnSe for each category.[16]

Categories	Compensating defects/type of solubility
Native defects	$\underline{V_{Se}, V_{Zn}}$ [17] $\underline{Se_i, Zn_i, Zn_{Se}, Se_{Zn}}$ [18]
Complex defects	N_{Se}-V_{Se} [19] $\underline{N_{Se}\text{-}Zn_i}$ [20] Nitride complex (Se_4N_4)[21]
Associated-impurity defects	$\underline{N_i}$, $\underline{N_{Se}\text{-}N_i}$ [22] $\underline{Zn\text{-}(N_{Se})_n, N_{Se}\text{-}N_{Zn}}$ [23] $\underline{(N_2)_i, (N\text{-}N)_{Se}}$ [24]
Bond breaking defects	$\underline{\text{Impurity-host bond breaking}}$ [25] Host-host bond breaking [26]

Table 1 Proposed compensating defects that limit the p-type doping in nitrogen doped ZnSe. Those underlined are defects less likely to exist in MBE grown ZnSe:N, based on prior studies.

1. Native defects

Laks et al[18] has proposed that when using advanced, non-equilibrium crystal growth processes such as MBE and MOCVD, isolated native defects such as vacancies, interstitials, and antisite defects are too small in number to

Reproduced with permission of the copyright owner. Further reproduction prohibited without permission.

compensate doped impurities. Thus, these isolated native defects are not expected to play a major role in the compensation process of epitaxial layers.

2. Complex defects

There are two types of complexes working as compensation defects in this category. The first type is the complex consisting of substitutional nitrogen at a Se site (N_{Se}) and a native defect, such as the vacancy at the Se site (V_{Se}) and Zn interstitials (Zn_i). Hauksson et al[19] has proposed that a N_{Se}-V_{Se} complex in ZnSe:N may work as a single donor and it may be the origin of the deep donor-acceptor-pair (D^dAP) emission observed in low-temperature photoluminescence in this material. Garcia and Northrup[20] has theoretically predicted that the N_{Se}-Zn_i complex may play a significant role in hole compensation. However, Yao et al[23] has applied particle induced X-ray emission (PIXE) to get insight into the lattice location of Zn and Se atoms in heavily doped ZnSe:N and the results show that Zn and Se atoms are located at the substitutional sites and there is no detectable signal from interstitial Zn and Se atoms in these samples. Thus, he concluded that the hole compensation in heavily doped ZnSe:N is not likely caused by the Zn_i-related complex defect. Molecular beam epitaxy is a non-equilibrium growth technique. Optimized MBE growth and doping conditions such as growth rate and group

Reproduced with permission of the copyright owner. Further reproduction prohibited without permission.

II/VI flux ratio may be useful to further reduce the formation of native defects such as Se vacancy (V_{Se}) as well as its related compensation defects. In addition, a non-equilibrium doping technique with growth interruption during dopant deposition, such as the δ-doping technique, has been observed in other cases to reduce these types of compensating defects.[34,37,38,39]

Another type of complex defects has been suggested by Baron et al.[21] They proposed that the achievable doping level is competing with the formation of dopant-associated chemical complexes such as nitride complexes for nitrogen doping. In their systematic study of nitrogen doped p-type ZnCdTe alloys, the hole concentration dramatically decreased as the Cd content increased while the incorporated nitrogen concentration [N] measured by nuclear reaction analysis did not change significantly with alloy composition. The difference between [N] and hole concentration is as large as 3 orders of magnitude for CdTe. By eliminating other compensation effects in N doped ZnTe-based alloys, they attributed this big difference to the addition of Cd atoms. One possible explanation for the rapid decrease with the increase of Cd concentration is the formation of Cd_3N_2 complex. They proposed that the formation enthalpy (heat) of Cd_3N_2 is higher than that of CdTe thus the preferential formation of the nitride will lower the amount of available nitrogen for forming N_{Te} acceptors. In nitrogen doped ZnMgTe alloys, Mg_3N_2

Reproduced with permission of the copyright owner. Further reproduction prohibited without permission.

complex has a similar formation preference compared to MgTe.[21] A more abrupt decrease of hole concentration with increase of Mg concentration in ZnMgTe:N was also observed in their study. In nitrogen doped Se-based II-VI materials, where the compensation mechanisms are much more complicated, the compensation due to the formation of nitride complexes should be seriously considered. A similar difference between [N] and net acceptor concentration (N_A-N_D) in ZnSe:N has also been observed. For example, nitrogen doped ZnSe has a (N_A-N_D) level of 1 x 10^{18} cm^{-3} while the incorporated nitrogen [N] is larger than 5 x 10^{18} cm^{-3}, detected by SIMS.[12] This suggests that only part of incorporated nitrogen atoms act as acceptors. The formation of a nitride complex such as Se_4N_4 may be responsible for lowering the amount of available nitrogen atoms to act as acceptor impurities.[21] If this is the dominant compensation mechanism in ZnSe-based materials, then a modulation doping technique with growth interruption during dopant deposition should be useful in suppressing the nitride complex formation so as to increase the p-type doping efficiency. However, previous experimental results have shown that a conventional δ-doping and atomic layer epitaxy (ALE)[28] cannot increase the maximum (N_A-N_D) level of nitrogen doped ZnSe over 1 x 10^{18} cm^{-3} suggesting that other mechanisms may dominate its compensation.

Reproduced with permission of the copyright owner. Further reproduction prohibited without permission.

3. Associated-impurity defects

Recent theoretical studies suggest that atomic nitrogen tends to substitute at a Se site[29] and Yao et al[23] has experimentally shown that most of the incorporated N is situated at the substitutional Se sites according to the angular distribution spectra of γ-rays emitted from N atoms in heavily doped ZnSe:N. Hence N_i and N_{Se}-N_i are not likely to exist. Furthermore, by comparing the angular distribution spectra of γ-rays from N atoms in a N-doped ZnSe sample and from N_2 molecules in a N_2-implanted ZnSe, it has been concluded that in MBE grown ZnSe:N preferential occupation at substitutional sites is in the form of atomic nitrogen rather than the molecular nitrogen.[16] Thus, $(N_2)_i$ and $(N_2)_{Se}$ are less likely to exist in ZnSe:N. Yao et al[23] did observe that Zn-$(N_{Se})_n$ [such as Zn-$(N_{Se})_2$, i.e. N_{Se}-Zn-N_{Se}] and N_{Se}-N_{Zn} centers, which work as deep hole traps, exist in heavily nitrogen implanted ZnSe samples with [N]~1.5 x 10^{20} cm^{-3}. Yet this should not play a significant role in the hole compensation in conventionally doped ZnSe:N whose [N] < $10^{19}cm^{-3}$. Based in this discussion, these associated-impurity defects [N_i, N_{Se}-N_i, $(N_2)_i$, etc] should be less likely to play significant roles of the limitation of p-type doping of nitrogen doped ZnSe.

Reproduced with permission of the copyright owner. Further reproduction prohibited without permission.

4. Bond breaking defects

Two types of the bond-breaking mechanisms can be considered: the impurity-host bond breaking and the host-host bond-breaking. Figure 8 shows the schematic diagrams of an ideal ZnSe:N bond structure [in (a)] and the two bond-breaking structures. Figure 8(b) presents a large atomic relaxation in the vicinity of acceptor impurities (indicated in the dashed square) which leads to a significant alteration of their electronic properties. For p-type doping of II-VI wide bandgap materials, this impurity-host bond breaking may lead to a deep state which can trap a hole from other acceptors to form a more stable state, a positively charged AX^+ defect center. A similar DX^- compensation center has been observed in n-type doped $Al_xGa_{1-x}As$ alloys.[30] Based on theoretical calculations, it has been suggested that nitrogen in ZnSe is not likely to exhibit this type of lattice relaxation, while it is very likely to occur in MgSe- or CdSe- based II-VI materials.[15]

Figure 8(c) shows the structure diagram of the host-host bond breaking process.[26] Two Zn-Se bonds with one common Zn, nearest to the impurity, are broken and a Se-Se dimer is formed due to the impurity-induced lattice distortion. This impurity complex can compensate a hole from an acceptor impurity and form an AX^+-type center. Theoretical studies suggest that the host-host bond-breaking is energetically favorable in nitrogen doped ZnSe

Reproduced with permission of the copyright owner. Further reproduction prohibited without permission.

and MgSe (a more serious case), while it is very unlikely to occur in nitrogen doped ZnTe.[26] We have observed that in nitrogen doped $Zn_{1-x}Mg_xSe$ alloys the $(N_A\text{-}N_D)$ level dramatically decreases as Mg content increases which is consistent with the prediction of this model. In addition, the model also provides a satisfactory explanation for the presence of persistent photoconductivity (PPC). Unfortunately, if the host-host bond-breaking mechanism is the dominant compensation mechanism in p-type doped ZnMgSe-based II-VI materials, it seems impossible to prevent by conventional (i.e. uniform and typical δ-) doping techniques as long as the impurity-induced distortion exists

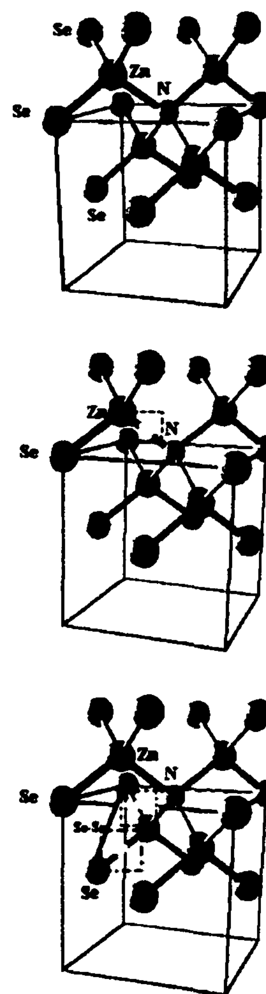

Figure 8 (a) Ideal bond structure of N-doped ZnSe. (b) Proposed model of impurity-host bond breaking. The bond between a substitutional nitrogen and Zn host may be broken due to the lattice relaxation as shown by the dashed square. (c) Model of host-host bond breaking. Two Zn-Se bonds (with common Zn), nearest to a substitutional nitrogen atom, may break as shown by the dashed squares and form a Se-Se dimer (red line). This bond-breaking complex works as a single donor.

Reproduced with permission of the copyright owner. Further reproduction prohibited without permission.

in the crystals. In order to overcome the host-host bond-breaking, logically one should consider how to isolate the substitutional nitrogen bonds (N-Zn) from Zn-Se bonds. Using Te atoms as a co-dopant during nitrogen doping may be a good way to change the local environment of the incorporated nitrogen. Details about the Te-codoping techniques will be addressed in Section 3-5.

5. Solubility limit

The concept of solubility limit should be considered as 1) the material (impurity) solubility limit[27] and 2) the upper limit of the achievable free carrier concentration.[13] The material solubility is a concept based on thermodynamic equilibrium considerations. This solubility argument, if applicable to the kinetic situation of the non-equilibrium growth by MBE, should be considered in the selection of a suitable dopant. Laks et al[27] proposed solubility limits of various p-type dopants in ZnSe. At the experimental growth temperature of 250 °C, the calculated solubility limit for nitrogen in ZnSe is 2×10^{19} cm^{-3} while 4×10^{15} and 6×10^{18} cm^{-3} for Na and Li, respectively. The proposed solubility limit of nitrogen in ZnSe actually is enough for obtaining low p-type resistivity if all of incorporated nitrogen atoms can work as acceptors. Thus, nitrogen is basically an ideal p-type

Reproduced with permission of the copyright owner. Further reproduction prohibited without permission.

dopant for ZnSe in terms of the impurity solubility limit.

A model to predict the maximum achievable free carrier concentration in II-VI materials has been proposed by Faschinger et al.[13] They applied the amphoteric defect model in III-V materials proposed by Walukiewicz[31] to predict the maximum achievable free carrier concentration for various II-VI materials. This model simply considers an assembly of compensation effects without recognizing individual mechanisms and assumes that the formation reaction of the compensation defects is similar in most of the II-VI materials. Therefore, the energetic position (E_{SI}) of forming defects, which act as compensation centers, will be a constant relative to the vacuum level in most of II-VI materials. When the Fermi level (E_F) in II-VI semiconductors, moving with doping level, approaches the E_{SI}, the system starts to form the compensation defects with an opposite charge instead of adding "free" carriers to the material. Thus, there should be a maximum value of free carrier concentration when the E_F just approaches the E_{SI} position.

Figure 9 shows the predicted (solid curve) and reported (points) of maximum free electron concentration of various n-type doped II-VI materials as a function of CBM positions on an absolute energy scale, assuming VBM_{ZnSe}= 0. The E_{SI} position is determined (2.59 eV above VBM_{ZnSe}) from Cl-doped ZnMgSe whose maximum free electron concentration and

Reproduced with permission of the copyright owner. Further reproduction prohibited without permission.

bandedge positions on an absolute energy scale are known. As shown in Figure 9, the experimental and predicted data match very well when the level is below 10^{19} cm^{-3}. This suggests that the model describes well the compensation behavior in n-type doped II-VI materials where the compensation phenomena is not significant. However, the maximum achievable free electron concentration deviates from the predicted value when the level is beyond 10^{19} cm^{-3}. This could be due to a more significant compensation effects that become dominant when the doping level is high. The triangles in Figure 9 present the reported maximum free electron concentrations of Cl doped ZnSe obtained by δ-doping. Interestingly, the δ-doping technique (open triangle) seems able to overcome the compensation so that the carrier concentration goes back to follow the predicted curve.

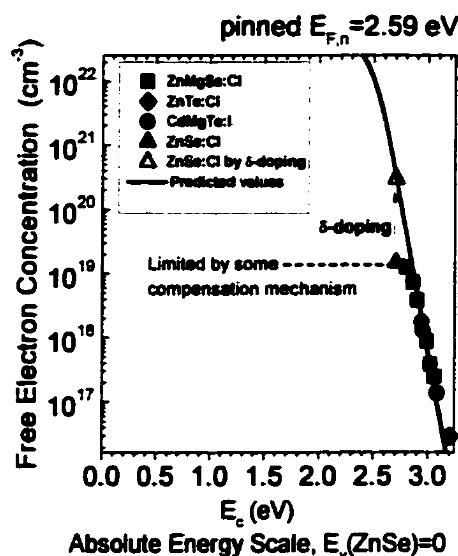

Figure 9 Free electron concentration vs CBM position on an absolute energy scale. Points represent those highest reported free electron concentrations of various n-type doped II-VI materials. The solid curve represents the predicted value by the model. The dashed line suggests that some compensation effect is observed but the δ-doping technique can overcome it (open triangle).

In p-type doped Se-based II-VI materials where the compensation

Reproduced with permission of the copyright owner. Further reproduction prohibited without permission.

mechanisms are more complex, the maximum free hole concentration of nitrogen doped ZnSe is predicted to be 1 x 10^{18} cm^{-3} by using the II-VI amphoteric defect model[13]. This suggests that the achievable (N_A-N_D) level should be higher than that.[50] Based on this prediction, the maximum p-type doping level of ZnSe has not been achieved yet. A (N_A-N_D) level higher than 1 x 10^{18} cm^{-3} in ZnSe:N should be possible if the concentration of its compensation centers is reduced.

After the above discussion, the remaining compensation defects, which may significantly affect the p-type doping properties of ZnSe:N, are complex defects [including (N_{Se}-V_{Se}) and nitride complexes], and host-host bond breaking defect. Besides these, the solubility limit (especially in the substitutional sites) should still be considered as a possible limiting mechanism. These defects and the solubility limits may also play an important role of limiting the achievable carrier concentration in $Zn_{1-x-y}Mg_xCd_ySe$ alloys. In the following sections, p-type doping of ZnSe using an rf discharge nitrogen plasma source will be addressed. Besides uniform doping, several modulation doping techniques, such as conventional δ-doping with nitrogen and δ-doping with nitrogen and Te (N+Te) codoping, will be used to improve the p-type doping efficiency. Then, a systematic study in the p-type doping of $Zn_{1-x}Mg_xSe$ and $Zn_{1-y}Cd_ySe$ ternaries as a function of material composition

Reproduced with permission of the copyright owner. Further reproduction prohibited without permission.

will be addressed.

Reproduced with permission of the copyright owner. Further reproduction prohibited without permission.

3-4 p-type doping of ZnSe using an rf discharge nitrogen plasma source

ZnSe has been recognized as one of the most promising II-VI semiconductors for optoelectronic device applications due to its direct bandgap near 2.7 eV, just enough to provide a blue emission. Several elements including Li, Na, P, As, and N have been investigated for use as dopants to obtain p-type ZnSe while Cl has been found to be the satisfactory dopant for n-type doping (Section 3-1). In terms of success in incorporating substitutional acceptor impurities in ZnSe, Li was first considered as an efficient dopant by MBE. However, an upper limit of Li-doping [$(N_A-N_D)\sim10^{17}$ cm^{-3}] and the instability of Li atoms in ZnSe suggest that Li is not an ideal dopant for device applications.

Over the past few years, nitrogen has been found to be the best dopant for obtaining p-type ZnSe by MBE, so far, with the highest net acceptor concentration (about 1 x 10^{18} cm^{-3}) by conventional doping techniques. The nitrogen acceptors in ZnSe have activation energy of 110 meV. This is a relatively shallow acceptor level,[32] compared with others. Since Park et al[33] reported a highly efficient incorporation of atomic nitrogen by MBE using an rf (13.56 MHz) discharge nitrogen plasma source (mainly containing $N+N_2$), this atomic nitrogen source has become the most frequently used

Reproduced with permission of the copyright owner. Further reproduction prohibited without permission.

source for the p-type doping of MBE grown ZnSe and related II-VI compounds. In this section, we employ rf discharge nitrogen plasma source for p-type doping of ZnSe, supplied by Oxford Applied Research (Model MPD 21). The success of nitrogen doping of ZnSe can help us to learn the optimum nitrogen source conditions in our quaternary system.

nitrogen doped ZnSe layers were grown on (001) p^+-conductive GaAs substrates. The p^+- GaAs substrates were prepared by degreasing and etching in standard H_2SO_4:H_2O_2:H_2O solution of 4:1:1 concentration prior to its introduction into an ultra high vacuum (UHV) chamber. The GaAs substrates were thermally deoxidized and outgased in the III-V chamber at about 600 °C under As flux followed by the growth of Be-doped GaAs (p-type) buffer layer. The substrates were then transferred to the II-VI chamber via a UHV track chamber.

Prior to the growth in the II-VI chamber, a 15-second Zn-irradiation was performed to suppress the formation of Ga-Se related complexes on the II-VI/III-V interface which may cause stacking faults. A uniformly nitrogen doped ZnSe layer was then grown. The growth temperature of ZnSe was 250 °C. The beam equivalent pressure (BEP) ratio of Se to Zn was 2. A streaky (2 x 1) RHEED pattern was observed suggesting a Se-stabilized surface and a preferred 2-dimensional growth mode during the doping. The nitrogen

Reproduced with permission of the copyright owner. Further reproduction prohibited without permission.

doping efficiency was studied as a function of ZnSe growth rate and nitrogen source conditions. The optimum growth rate is 0.8 μm/hr in terms of crystalline quality and doping efficiency. The optimum discharge nitrogen source conditions were an rf power of 400 W and a pure nitrogen (6N) flow corresponding to a chamber background pressure of 8 x 10^{-6} torr. The setup and operation of nitrogen source equipment was described in more detail in Chapter 2.

The (N_A-N_D) level of ZnSe:N was obtained from the characterization by C-V and electrochemical C-V profiling. The details of those measurements were described in Chapter 2. In general, the (N_A-N_D) levels obtained from both profiling methods are consistent with each other. Figure 10 shows the depth-dependent (N_A-N_D) level of a uniformly doped ZnSe:N sample with the optimum nitrogen source conditions. The result was obtained by electrochemical C-V profiling and shows an average (N_A-N_D) level of 7

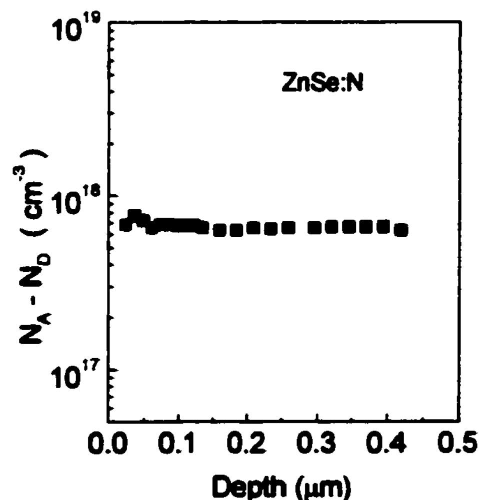

Figure 10 Depth-dependent (N_A-N_D) level of a uniformly doped ZnSe:N, measured by electrochemical C-V profiling. The sample was grown with the optimum discharge nitrogen condition.

Reproduced with permission of the copyright owner. Further reproduction prohibited without permission.

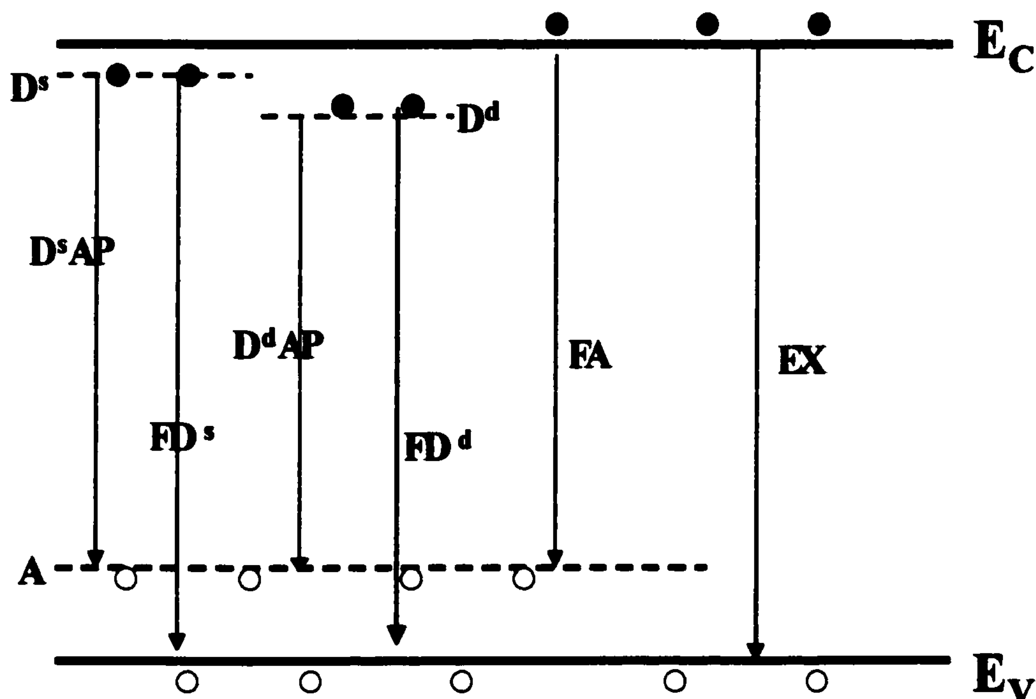

Figure 11 Schematic diagram of impurity levels and the transitions associated with each level in nitrogen doped ZnSe. E_c and E_V represent the CBM and VBM positions, respectively. D^s, D^d and A represent the shallow donor, deep donor, and acceptor levels, respectively. F represents a free carrier. These arrows represent various transitions between different levels. For example, EX indicates the excitonic transitions.

x 10^{17} cm^{-3}, which is close to the highest reported value of uniformly nitrogen doped ZnSe.

Figure 11 represents an energy diagram of the different impurity levels in ZnSe:N and the transitions associated with those levels. Besides the acceptor level [denoted as A, 110 meV higher than the valence band maximum (VBM) of ZnSe], a shallow donor level [D^s, 26 meV below the conduction band minimum (CBM) of ZnSe] and a slightly deeper donor

Reproduced with permission of the copyright owner. Further reproduction prohibited without permission.

level (D^d, 45 meV below the CBM of ZnSe) may also be introduced with nitrogen incorporation.[34] The transitions (arrows) shown in Figure 11 have been well studied by temperature-dependent photoluminescence (PL) in the past years.[34,35]

Figure 12(a)&(b) show the PL spectra of a uniformly nitrogen doped ZnSe [$(N_A-N_D) \sim 3 \times 10^{17} cm^{-3}$] at 9.5, 60, and 110 K. The 9.5 K spectrum shows a strong free exciton emission (EX) at 2.804 eV, a dominant I_1 emission associated with exciton bound at a neutral shallow N acceptor at 2.792 eV, and donor-acceptor-pair (DAP) emissions. The DAP emissions include a shallow donor-acceptor-pair (D^sAP) emission at 2.705 eV, a deep donor-acceptor-pair (D^dAP) emission at 2.686 eV, and their longitudinal optical (LO) phonon replicas (separated by 31 meV).

The shoulder on the right of the D^sAP peak was assigned as the free-to-acceptor (FA) emission at around 2.72 eV. At 60 K, the shallow donors are partially thermally ionized. Thus the emission due to the transition from a free electron to a neutral acceptor (FA) becomes more obvious as shown in Figure 12(a) (the blue curve). When the temperature was further increased above 100 K, the shallow donor was fully thermally ionized so that the FA emission at 2.702 eV becomes dominant and its strong LO-phonon replicas

Reproduced with permission of the copyright owner. Further reproduction prohibited without permission.

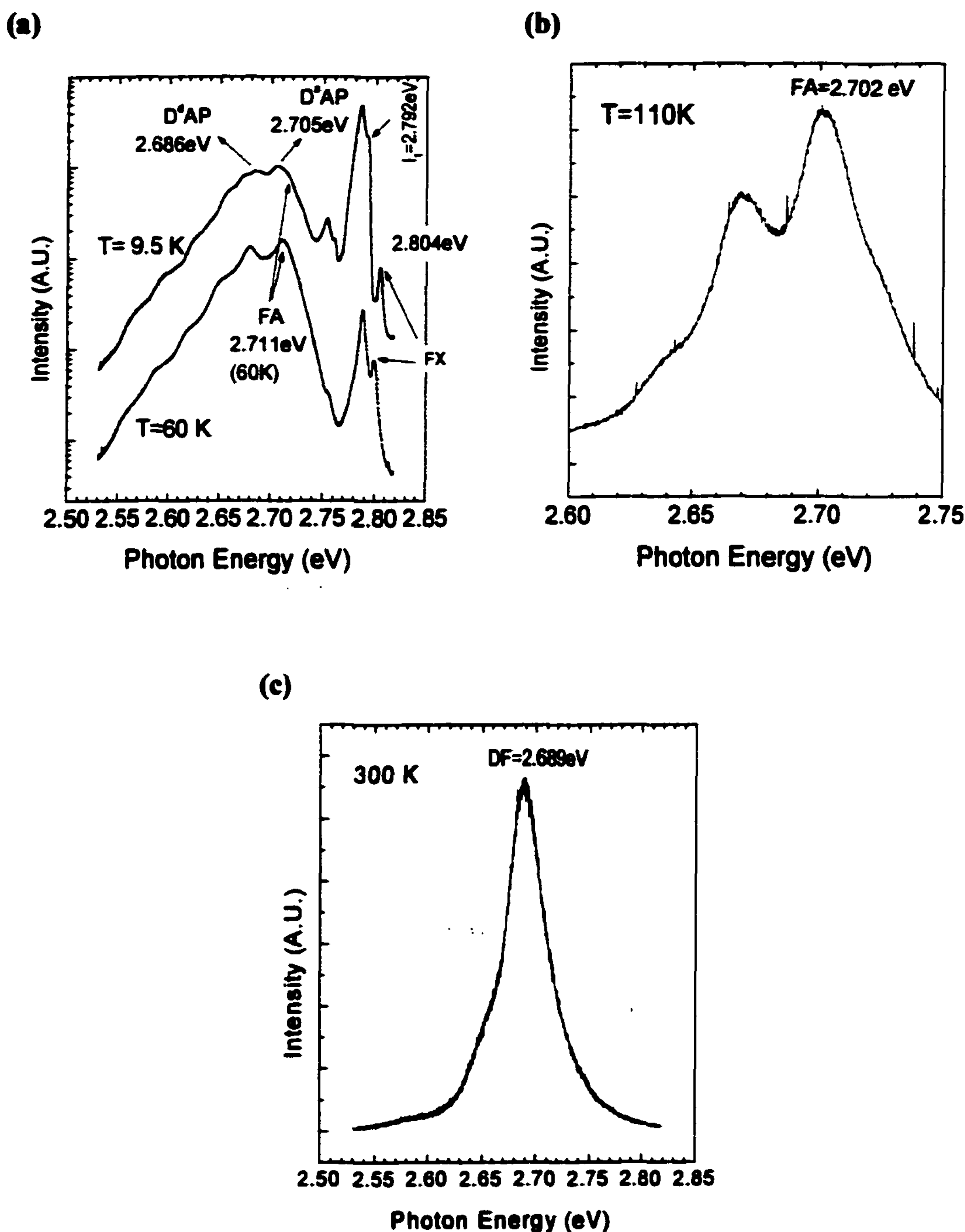

Figure 12 **(a)** PL spectra of uniformly nitrogen doped ZnSe [$(N_A$-$N_D)$~3 x 10^{17} cm^{-3}] at 9.5 and 60 K. Each peak, except the peak at 2.78~2.79 eV, has been assigned to different transition which is shown in Figure 11. The broad peak at around 2.75~2.76 eV is the LO-replica of the I_1 emission. **(b)** PL spectrum of the same sample at 110 K. The FA emission and its LO-replicas become dominant in the spectrum suggesting thermal ionization of shallow donors to the conduction band at this temperature. **(c)** 300 K PL spectrum of another uniformly nitrogen doped ZnSe [$(N_A$-$N_D)$~8 x 10^{16} cm^{-3}]. The dominant peak was assigned to shallow donor-to-free hole transition as shown in Figure 11. The appearance of this peak suggests a thermal ionization of acceptor to the valence band.

Reproduced with permission of the copyright owner. Further reproduction prohibited without permission.

appear as shown in Figure 12(b). Figure 12(c) represents a 300 K PL spectrum of a lightly doped sample of ZnSe:N (8×10^{16} cm^{-3}). At room temperature, the FA emission disappears and the shallow donor-to-free hole (DF) emission increases as shown in Figure 12(c). The appearance of DF emission indicates the thermal ionization of acceptors at room temperature.

An (N_A-N_D) level higher than 8×10^{17} cm^{-3} cannot be achieved by uniform doping in our system. The low-temperature PL spectrum of highly nitrogen doped ZnSe [(N_A-N_D) ~ 7×10^{17} cm^{-3}] shows a dominant D^dAP emission and its replicas. Zhu et al[34] has proposed that the deep donor (D^d) is associated with the N_{Se}-V_{Se} complex which works as a carrier compensation center in ZnSe:N. The same group also used a conventional δ-doping technique with nitrogen to suppress the formation of Se-vacancies (V_{Se}) as confirmed by the reduction of D^dAP emission in low-temperature PL spectrum.[34] Although Se vacancies and their related compensation complexes were reduced significantly by this technique, an (N_A-N_D) level higher than the optimum value (about 1×10^{18} cm^{-3}) has yet to be reported, suggesting that there may be other more active compensation defects involved in suppressing the nitrogen doping efficiency in ZnSe. As discussed in Section 3-3, with the exception of N_{Se}-V_{Se} complexes, after the pure nitrogen δ-doping technique is used, the dominant limiting mechanism

Reproduced with permission of the copyright owner. Further reproduction prohibited without permission.

in ZnSe:N would possibly result from the host-host bond-breaking defect or the solubility limits (in the substitutional sites). In order to prevent the bond breaking type of defects, it would be necessary to isolate the substitutional nitrogen from Zn-Se bonds.

In the next section, several modulation doping techniques will be discussed, including conventional δ-doping with nitrogen, and special δ-doping with N+Te codoping. These will be investigated for enhancing the p-type doping of ZnSe.

Reproduced with permission of the copyright owner. Further reproduction prohibited without permission.

3-5 Modulation doping techniques

Despite the fact that a high net acceptor concentration (N_A-N_D), ~1 x 10^{18} cm^{-3}, of ZnSe:N has been achieved, the obtainable p-type conductivity is still not sufficient for some practical device requirements such as the formation of p-type ohmic contacts. In this section, several modulation doping techniques, including conventional δ-doping with nitrogen and special δ-doping with N+Te codoping, will be systematically studied for enhancing the p-type doping of ZnSe.

3-5-1 Conventional δ-doping with nitrogen

Delta-doping was first developed for Ge doping in MBE grown GaAs by Wood et al.[37] The basic idea of the δ-doping technique is to insert a dopant-concentrated atomic layer into an undoped region during a growth interruption. Figure 13 shows a schematic diagram of a typical δ-doped structure. The versatility of the growth-interrupted dopant deposition, including the reduction of self-compensation, was demonstrated by many groups.[34,37,38,39] This technique was first applied to ZnSe by de Miguel, et al in 1988 for investigations of Ga-doped ZnSe (ZnSe:δ Ga).[39] In the study of ZnSe:δ Ga, the n-type doping efficiency was enhanced by a factor of three by

Reproduced with permission of the copyright owner. Further reproduction prohibited without permission.

depositing Ga impurities on the Zn-terminated ZnSe surface during growth interruption. It was concluded that compensation centers associated with Zn vacancy-dopant atom complexes (V_{Zn}-Ga_{Zn}) were reduced by the δ-doping. As mentioned previously,

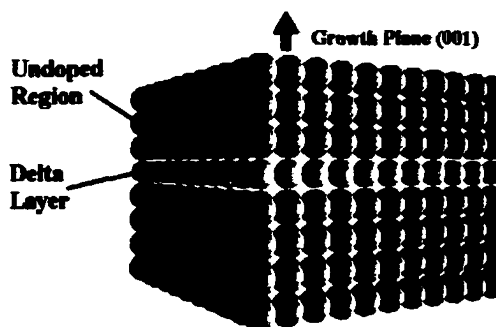

Figure 13 Schematic diagram of a typical δ-doped structure. The dopant-concentrated atomic layer is inserted among several undoped atomic layers (spacers).

for nitrogen doping of ZnSe, Zhu et al used a conventional δ-doping technique to reduce N_{Se}-V_{Se} complexes that were believed to work as compensation centers in nitrogen doped ZnSe.[34] These results suggest that the δ-doping is a doping technique that can reduce complex-type defects.[37] In this section, a conventional δ-doping technique, with nitrogen, will first be investigated in ZnSe.

Prior to the growth of the δ-doped region, a uniformly nitrogen doped ZnSe was grown as a buffer layer on a GaAs substrate. The details about the growth of the uniformly nitrogen doped ZnSe layer are described in Section 3-4. For the growth of the δ-doped region, the growth conditions and the nitrogen source conditions remained the same as those of the ZnSe:N buffer layer. The shutter control sequence of the element sources was complex and

Reproduced with permission of the copyright owner. Further reproduction prohibited without permission.

required a computer to control the shutters. Figure 14 shows the shutter control sequence of the conventional δ-doping technique. A ZnSe undoped region was first grown for t_{ZnSe} seconds and then the Se shutter was closed. The Zn shutter remained open for t_{Zn} seconds to interrupt the growth and to produce a Zn-terminated surface. Then all the shutters were closed for t_{all} seconds to desorb excess Zn from the surface. The shutter of the discharge nitrogen source was then open to deposit nitrogen onto the Zn-terminated surface for t_N seconds. After another interruption time of t_{all} seconds, Zn was again evaporated onto the N concentrated surface for t_{Zn} seconds followed by opening the Se shutter for the next undoped ZnSe region (t_{ZnSe} seconds). The thickness of the undoped ZnSe spacer was basically determined by the opening duration of Se shutter (t_{ZnSe}). The best results occur when t_{Zn}= t_{all}= t_N= 5 seconds (see Table 1 below). In addition, other groups had reported that the depositing of nitrogen on Se-terminated surfaces decreased the nitrogen doping efficiency,[36] thus the Zn-terminated surface was used for the following δ-doping experiments.

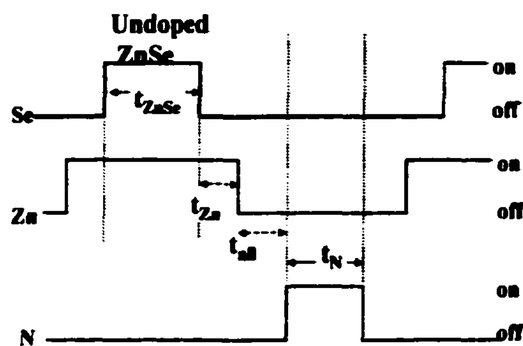

Figure 14 Shutter control sequence of the conventional δ-doping technique with pure nitrogen alone.

Reproduced with permission of the copyright owner. Further reproduction prohibited without permission.

First, a conventional δ-doped sample was grown with nitrogen plasma conditions that produce a low $(N_A\text{-}N_D)$ level of 8×10^{16} cm^{-3}. Figure 15(a) shows the depth-dependent $(N_A\text{-}N_D)$ level of the δ-doped ZnSe:N sample. In this sample, a uniformly nitrogen doped ZnSe buffer was first grown on a (001) p^+-GaAs substrate followed by the growth of the δ-doped region. The δ-doped region has 120 units (periods) where each unit includes one nitrogen doped atomic layer and 12 monolayers (MLs) of undoped ZnSe layers. The rf discharge power for the discharge nitrogen source was operated at 300 W and a nitrogen flow corresponding to a chamber background pressure of 6×10^{-6} torr was used. The nitrogen source conditions remained the same during the

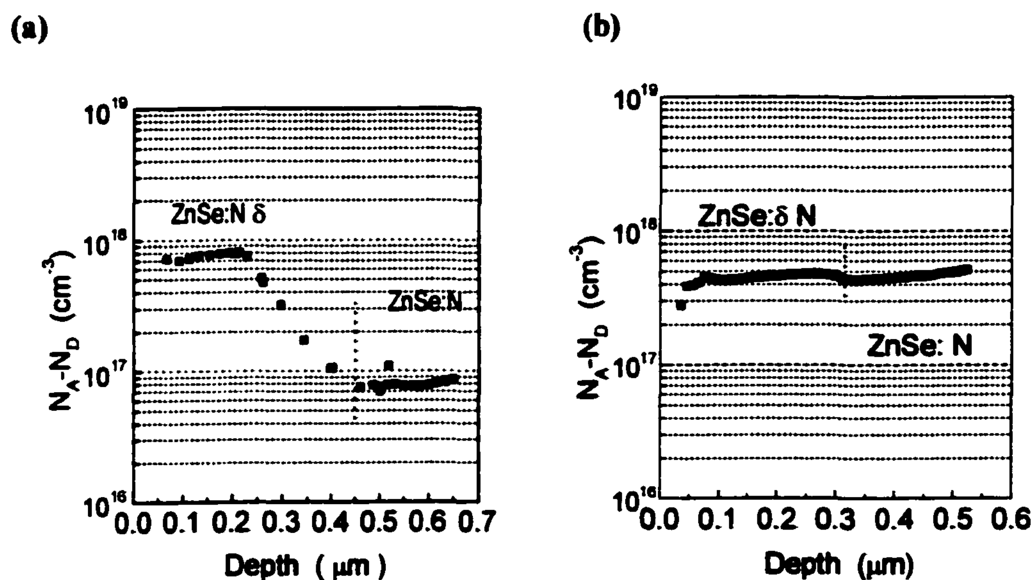

Figure 15 Depth-dependent $(N_A\text{-}N_D)$ levels of conventional δ-doped ZnSe:N samples using low (a) and high (b) nitrogen conditions. In (a), the $(N_A\text{-}N_D)$ level is dramatically increased to 8×10^{17} cm^{-3} from 8×10^{16} cm^{-3} using the conventional δ-doping technique while the level remains around 5×10^{17} cm^{-3}.

Reproduced with permission of the copyright owner. Further reproduction prohibited without permission.

entire growth process. The depth-dependent (N_A-N_D) level was determined by electrochemical C-V profiling. The etched depth was controlled by the computer and calibrated by the use of an Alpha Step-200 surface profiler after measurements. The details of this measurement technique are described in Chapter 2. As shown in Figure 15(a), an (N_A-N_D) level of 8 x 10^{17} cm^{-3} in the δ-doped region has been obtained while a level of only 8 x 10^{16} cm^{-3} is obtained in the uniformly doped region. This dramatic increase in doping level may be correlated with an increase of nitrogen concentration, or the decrease of the compensating defects. Secondary ion mass spectroscopy (SIMS) analysis[43] of a similar sample shows that the average nitrogen concentration in the δ-doped region was actually slightly lower than that in the uniformly doped region suggesting that a reduction of compensation defects is responsible for the improvement. In fact, many studies by other groups also attributed the improvement of the p-type doping level by δ-doping techniques to a reduction of compensating defects.[34,37,38,39]

Another sample was grown with a narrower undoped ZnSe spacing (5 MLs) and the optimum nitrogen source conditions that produce a (N_A-N_D) level of high 10^{17} cm^{-3} in uniformly doped ZnSe. By these conditions, a higher average concentration of nitrogen was expected in this sample than in the previous one. No significant improvement of the (N_A-N_D) level, over 8 x 10^{17}

Reproduced with permission of the copyright owner. Further reproduction prohibited without permission.

cm^{-3} obtained in the uniformly doped region, has been observed as shown in Figure 15(b). This limiting behavior of δ-doped ZnSe:N has also been observed by other groups.[34,36]

Thus, the conventional δ-doping technique seems effective when the p-type doping level is low and then becomes ineffective when the hole concentration in the material is high. A theoretical calculation by Chadi et al[26] suggests that the host-host bond breaking compensating defect is promoted in the presence of free holes in ZnSe:N and thus should be more significant at higher doping levels. Based on these observations, we may derive the hypothesis that when the p-type doping level is low, one type of defect, such as N_{Se}-V_{Se} complexes, are responsible for the hole compensation in nitrogen doped ZnSe. This defect is effectively reduced by δ-doping. As soon as the p-type doping level (free hole concentration) becomes high, another compensating defect, such as the host-host bond-breaking defect, may become dominant.

If this hypothesis is correct, a p-type doping level higher than one achieved above (~ 8×10^{17} cm^{-3}) is impossible to achieve using these doping techniques. In order to reduce this type of compensation, the local environment around the substitutional nitrogen atoms must be changed (and in this way avoid the formation of structural defects). A possible way to do

Reproduced with permission of the copyright owner. Further reproduction prohibited without permission.

this is to replace the second nearest neighbors (the 12 group VI sites) around a substitutional nitrogen atom. For this purpose, Te atoms are proposed to be a good co-dopant, since substitutional nitrogen (at a Te site) is stable in a ZnTe crystal. Furthermore, the Te environment may improve the efficiency of nitrogen incorporation (i.e. increase its solubility).[42] However, Te atoms in ZnSe affect the optical properties of the material due to the formation of isoelectronic traps.[44] Thus, taking advantage of Te without significantly affecting the intrinsic properties of material, such as bandgap and lattice constant, is critical.

3-5-2 Single (N+Te)δ-doping technique

It has been reported that nitrogen at Te sites can work as a shallow acceptor and almost all of the nitrogen atoms incorporated in ZnTe work as acceptors[40] (i.e. $[N]=N_A$). This suggests that nitrogen will not introduce any significant carrier compensation centers ($N_D=0$) in ZnTe. Furthermore, the incorporated nitrogen concentration [N] in ZnTe is about one order of magnitude higher than that of ZnSe under the same nitrogen source condition.[40] Based on the advantages mentioned above, Te is expected to be an ideal co-dopant for improving the nitrogen doping efficiency in ZnSe-based II-VI materials.

Reproduced with permission of the copyright owner. Further reproduction prohibited without permission.

The shutter control sequence for the (N+Te)δ-doping technique is similar to that of the conventional δ-doping except that the Te shutter was opened and closed along with the nitrogen shutter, as shown in Figure 14. Figure 16 shows the depth-dependent (N_A-N_D) level of a (N+Te)δ-doped ZnSe sample which contains a 50 nm uniformly doped ZnSe:N cap layer, 120 units of (N+Te)δ-doped region (~300nm), and a 350nm uniformly doped ZnSe:N buffer layer. Each (N+Te)δ-doped cycle contains one (N+Te) containing atomic layer and 7 undoped ZnSe layers. As shown in Figure 16, the cap region has an (N_A-N_D) level of about $5 \times 10^{17} cm^{-3}$ and the level increases up to 1×10^{18} cm^{-3} in the (N+Te)δ-doped region. Then the level drops back to 5×10^{17} cm^{-3} in the buffer layer. The nitrogen source conditions were kept the same during the growth of each region. The (N_A-N_D) level of 1×10^{18} cm^{-3} in the (N+Te)δ-doped region is higher than the maximum values achieved in our growth chamber by uniform doping and by conventional δ-doping as

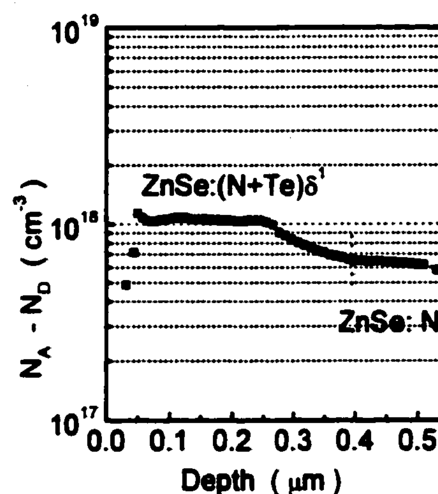

Figure 16 Depth-dependent (N_A-N_D) level of a single (N+Te)δ-doped ZnSe. The cap layer (first 50nm) and the buffer layer were uniformly doped ZnSe:N. The (N+Te)δ-doping can increase the p-type doping level up to 1×10^{18} cm^{-3}.

Reproduced with permission of the copyright owner. Further reproduction prohibited without permission.

discussed above.

Other parameters such as undoped spacing and nitrogen deposition time have been varied, while t_{Zn} and t_{all} were always kept at 5 seconds. Table 2 shows a list of several (N+Te)δ-doped samples grown with different δ-doping sequence parameters. As listed in Table 2, the optimum (N+Te) deposition time ($t_{N,Te}$) is 5 sec while a long (N+Te) deposition (10 sec) decreases the p-type doping efficiency and a short one produces less effect. The (N_A-N_D) level seems insensitive to undoped spacing at $t_{N,Te}$= 5 sec. No level higher than 1.5 x 10^{18} cm^{-3} was observed by this (N+Te)δ-doping. SIMS analysis of sample B suggests that the average amount of incorporated nitrogen in the (N+Te)δ-

#	ZnSe spacing	$t_{N,Te}$	(N_A-N_D) value (cm^{-3})		Doping efficiency
			Buffer	δ-region	
A	4 MLs	5 sec	3 x 10^{17}	1.5x 10^{18}	Enhanced
B	14 MLs	5 sec	6 x 10^{17}	1.2 x 10^{18}	Enhanced
C	7 MLs	5 sec	7 x 10^{17}	1.1 x 10^{18}	Enhanced
D	7 MLs	10 sec	3 x 10^{17}	9 x 10^{16}	Decreased
E	6 MLs	3 sec	3 x 10^{17}	5 x 10^{17}	Less enhanced

Table 2 Summary table of several significant (N+Te)δ-doped samples with different doping parameters.

Reproduced with permission of the copyright owner. Further reproduction prohibited without permission.

doped region is slightly lower than that in the buffer region. This suggests that the increase in acceptor concentration mainly results from the reduction of compensating centers. However, although the p-type doping level is improved, a level higher than 1.5 x 10^{18} cm^{-3} could not be achieved, suggesting that some limiting mechanism is still active in these (N+Te)δ-doped samples.

Figure 17 shows an ideal lattice structure around a substitutional nitrogen in a single (N+Te)δ-doped ZnSe sample. A substitutional nitrogen atom has 12 nearest group-VI sites (green balls and blue balls in Figure 17), 4 on the same (001) plane as nitrogen, 4 on the plane above, and another 4 on the plane below. In uniformly or conventionally δ-doped ZnSe with pure nitrogen alone, these 12 VI sites are occupied by 12 Se atoms. Thus their p-type doping level may be limited due to the nitrogen solubility limit (in substitutional sites) and/or structural defects such as the host-host bond-breaking defect. In (N+Te)δ-doped ZnSe, (in an ideal case) Te atoms may occupy the 4 group-VI sites (blue balls) on the same (001) plane of a substitutional nitrogen while the other 8 group-VI sites (green balls) are

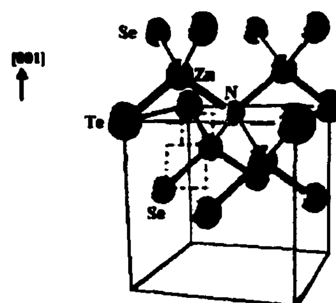

Figure 17 Ideal bond structure of a single (N+Te)δ-doped ZnSe. Those 4 group VI sites (blue balls), on the same (001) plane of the substitutional nitrogen atom (yellow ball) would be occupied by Te atoms while other 8 VI sites might be Se.

Reproduced with permission of the copyright owner. Further reproduction prohibited without permission.

occupied by Se atoms, as shown in Figure 17. It has been reported that the solubility of nitrogen in the substitutional sites in ZnTe is much higher than in ZnSe[40] and Zn-Te bonds around substitutional nitrogen is so stable that the bond-breaking defect is less likely to exist.[26] Thus, due to the replacement of ZnSe bonds with ZnTe ones, the solubility of substitutional nitrogen may be higher and/or the overall possibility to have the host-host bond breaking defects may be reduced. In a real case, the distribution of Te and Se atoms may be more complex so that the isolation of a substitutional nitrogen may not be as efficient as shown in Figure 17. Thus, the (N_A-N_D) level of a single (N+Te)δ-doped ZnSe is increased but still limited in the range of 1×10^{18} cm^{-3}.

If the models discussed above are correct, for a further improvement of the (N_A-N_D) level, a more efficient isolation of the substitutional nitrogen from Se atoms is necessary. A new approach, in which three consecutive (N+Te) atomic layers were deposited between undoped spacing layers [triple (N+Te)δ-doping or (N+Te)δ^3-doping], was developed for this purpose.

Reproduced with permission of the copyright owner. Further reproduction prohibited without permission.

3-5-3 (N+Te)δ^3-doping technique

The purpose of the (N+Te)δ^3-doping is to further isolate the substitutional nitrogen from Zn-Se bonds so as to prevent the bonds from breaking. For this purpose, three (N+Te) atomic layers are consecutively deposited on each undoped spacer layer, as shown in Figure 18(a). Figure 18(b) shows an ideal schematic bond structure of a (N+Te)δ^3-doped region indicated by the dashed square in Figure 18(a). In an ideal case, a substitutional nitrogen atom in the middle (N+Te) atomic plane would be surrounded by 12 Te atoms so that bond breaking will not occur. Thus, the middle (N+Te) plane may be free from the bond-breaking defects while two outer (N+Te) doped layers may still experience some compensation. In this case, the (N_A-N_D) level of a (N+Te)δ^3 structure should be significantly higher than that of the "single" (N+Te)δ-

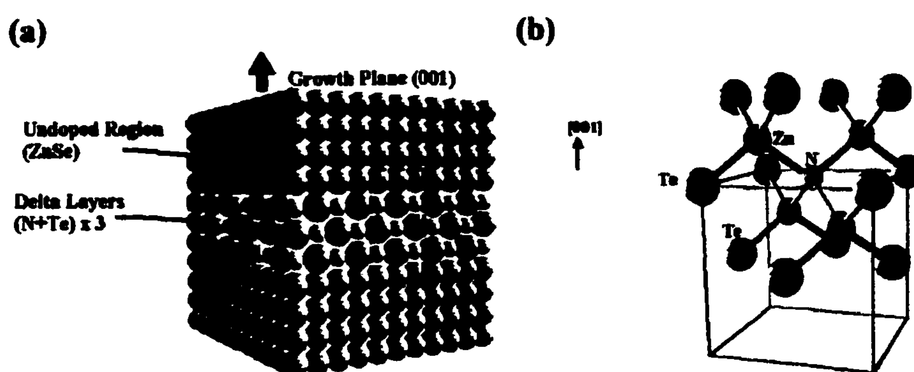

Figure 18(a) Schematic diagram of a (N+Te)δ^3-doped structure. **(b)** Ideal bond structure of the (N+Te)δ^3-doped ZnSe, as indicated on the dashed square of (a). Those 12 VI sites around a substitutional nitrogen atom of the middle (N+Te)-concentrated plane might be all occupied by Te atoms.

Reproduced with permission of the copyright owner. Further reproduction prohibited without permission.

doping technique.

The shutter control sequence for this technique is the same as that of the single (N+Te)δ-doping except that the procedure of (N+Te) deposition is repeated three times as indicated by the dashed arrow in Figure 19. Figure 20 shows the electrochemical C-V profiler result of a (N+Te)δ^3-doped ZnSe sample. The sample was grown on a (001) p^+-GaAs substrate and its structure includes 120 (N+Te)δ^3-doped units (~350nm) and an 800nm uniformly nitrogen doped ZnSe as a buffer layer. Each (N+Te)δ^3-doped unit contains 3 consecutive (N+Te) doped layers inserted between 7 MLs of undoped ZnSe. As shown in Figure 20, the (N_A-N_D) level in the (N+Te)δ^3-doped region is about 3 - 6 x 10^{18} cm^{-3} while that of the uniformly doped region is 3 x 10^{17} cm^{-3}. The level in the (N+Te)δ^3-doped region is significantly higher than the limiting value obtained with the single (N+Te)δ-doping, suggesting that compensation has been further reduced and/or the solubility limit was raised.

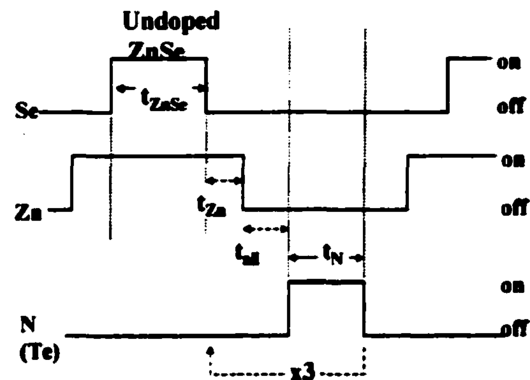

Figure 19 Shutter control sequence of the (N+Te)δ^3-doping technique.

Reproduced with permission of the copyright owner. Further reproduction prohibited without permission.

The average Te fraction of the $(N+Te)\delta^3$ sample is about 0.03 resulting in a lattice-mismatch of 0.28% to ZnSe. The value was calculated from the measured lattice constant assuming Vegard's law. It has been observed that the maximum p-type doping level of uniformly nitrogen doped ZnTe/ZnSe short period superlattices and ZnSeTe alloys significantly increase as Te content increases.[41,42] However, the (N_A-N_D) level of 3-6 x 10^{18} cm^{-3} (with only 0.03 Te fraction) corresponds to the optimum level obtained in a uniformly nitrogen doped ZnSeTe alloy with a Te fraction of about 0.12. A smaller Te content in the $(N+Te)\delta^3$-doped sample (only 0.03) suggests that the improvement of the p-type doping efficiency by the $(N+Te)\delta^3$ doping is not only due to an increase of Te content but to the effective isolation of nitrogen atoms from the ZnSe crystal.

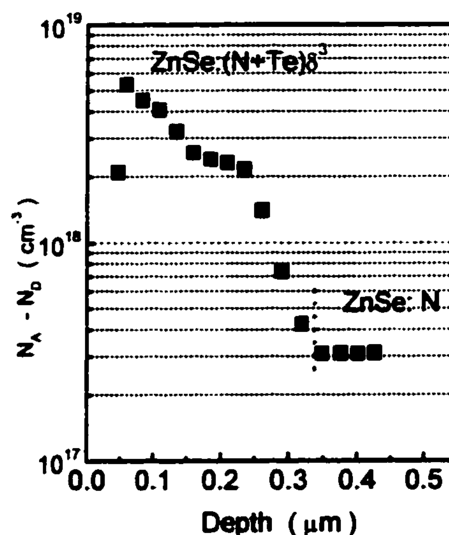

Figure 20 Depth-dependent (N_A-N_D) level of a $(N+Te)\delta^3$-doped ZnSe. The p-type doping efficiency of ZnSe is dramatically enhanced up to 6 x 10^{18} cm^{-3} by this new doping technique.

Another sample having an undoped spacing of 12 MLs was also studied. The (N_A-N_D) level is reproducibly in the mid 10^{18} cm^{-3} range. Moreover, if we compare the 12ML-$(N+Te)\delta^3$ sample with the 4ML-$(N+Te)\delta^1$ sample

Reproduced with permission of the copyright owner. Further reproduction prohibited without permission.

(Sample A in Table 2), the (N_A-N_D) level of the (N+Te)δ^3 sample is more than 3 times higher than that of the "single" (N+Te)δ-doped sample although the average amount of Te and nitrogen incorporated in both cases is expected to be about the same (3/12 : 1/4). This comparison illustrates the advantage of the (N+Te)δ^3-doping technique over the single (N+Te)δ-doping technique in terms of a more efficient isolation of the nitrogen atoms.

Figure 21 shows the I-V characteristics, measured between two gold electrodes on the sample surface, for the (N+Te)δ^3-doped sample of Figure 20 and for a uniformly nitrogen doped ZnSe [(N_A-N_D)=3 x 10^{17} cm^{-3}]. Dot electrodes were obtained by evaporating Au onto the clean surface of these samples without any post-deposition annealing. Each gold dot is about 500 μm in diameter and 3 mm in separation. The solid curve represents the I-V curve of the (N+Te)δ^3 sample while the dashed one is for the uniformly nitrogen doped ZnSe sample. It is well known

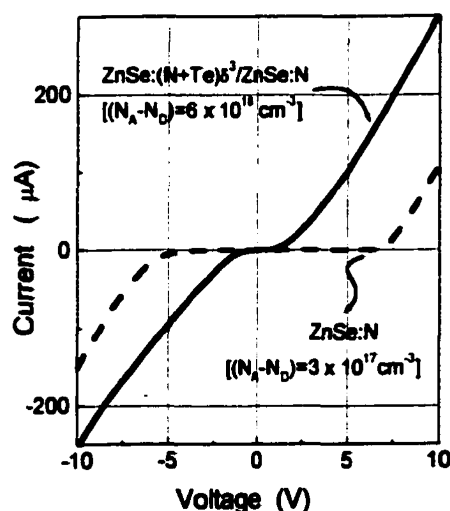

Figure 21 Contact-contact I-V characteristics of a uniformly and (N+Te)δ^3- doped sample.

Reproduced with permission of the copyright owner. Further reproduction prohibited without permission.

that Au forms a Schottky barrier on p-type ZnSe. The dashed curve in Figure 21 is a typical I-V curve of a back-to-back Schottky barrier. The tunneling effect of carriers over the barrier can be induced by either lowering the barrier height or thinning the depletion width produced in the semiconductor by the Schottky barrier. The reduction of the barrier height may be achieved by the selection of other contact materials or by post-deposition annealing. The depletion width is a function of the doping level in the semiconductor. A thin depletion width for tunneling to occur can be achieved by increasing the doping level of the semiconductor. The solid curve in Figure 21 presents more nearly ohmic characteristics for the $(N+Te)\delta^3$ doped sample, which is consistent with the increase of its (N_A-N_D) level. By using more sophisticated contact preparations, a more ideal ohmic behavior may be expected. It is not yet clear whether the ultimate doping level has been achieved by the new $(N+Te)\delta^3$-doping technique. However, based on its electrical properties and near lattice-matching to ZnSe, the $(N+Te)\delta^3$-doping technique shows a potential of obtaining a p-type ohmic contact layer for ZnSe-based devices without the large lattice mismatch to ZnSe, introduced by the ZnSe/ZnTe graded superlattice structure typically used for this purpose.[46]

Reproduced with permission of the copyright owner. Further reproduction prohibited without permission.

It is known that some isoelectronic impurities incorporated in binary compounds, such as Te in ZnSe, introduce trapping potentials due to differences in electronegativity.[44] For instance, Yao et al[44] have observed that Te impurities result in an emission band having phonon structure and peaking at 2.65 eV in slightly Te-doped ZnSe and a broad band at 2.48 eV in rather heavily Te-doped ZnSe at 14 K. In that study, the authors proposed that these emissions are much deeper than near bandedge emissions and attributed these deep emissions to the recombination of excitons bound at single Te (Te_1)

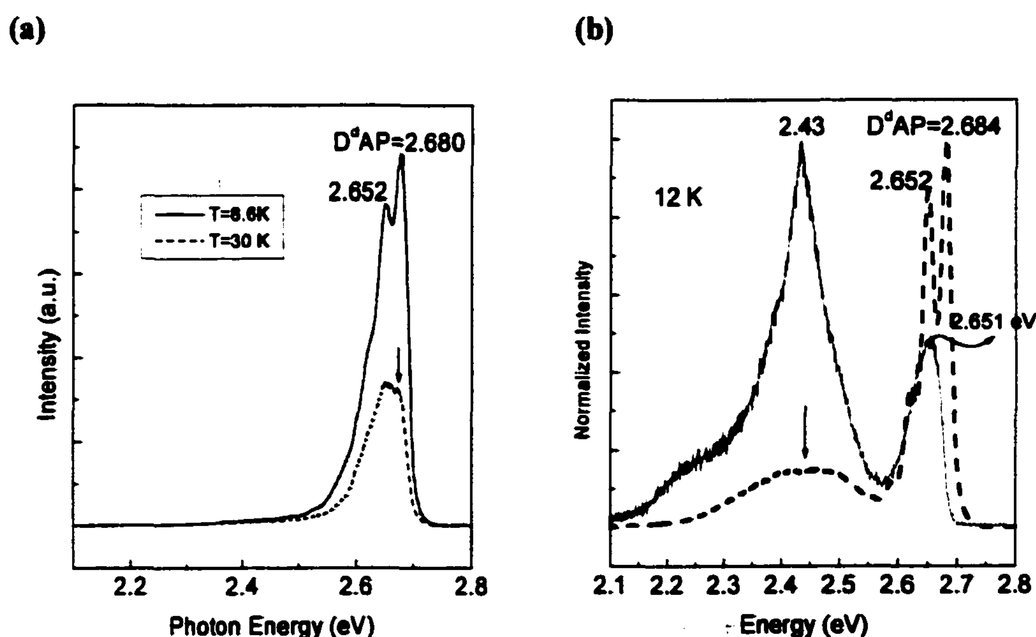

Figure 22(a) Low-temperature PL spectra of a single (N+Te)δ-doped ZnSe at 8.6 K and 30 K. The peak at 2.652 eV becomes dominant at 30 K suggesting a Te-related peak overlapping with the first phonon-replica of the D^dAP. **(b)** 12K PL spectra of a (N+Te)δ^3-doped ZnSe on an 800nm uniformly doped ZnSe:N buffer. The black spectrum represents a sample with 350nm (N+Te)δ^3-doped region while the dashed curve is for the 150 nm after etching of the same sample.

Reproduced with permission of the copyright owner. Further reproduction prohibited without permission.

atoms and Te clusters (Te_n, n>1). Figure 22 shows the low-temperature PL spectra of a single (N+Te)δ-doped (a) and (N+Te)δ^3-doped samples (b). The spectrum of the single (N+Te)δ-doped ZnSe shows a dominant D^dAP emission at 2.680 eV and another peak at 2.652 eV (about the position of the first LO phonon replica of the D^dAP transition). As the temperature was increased to 30 K, the D^dAP was suppressed and the peak at 2.652 eV became dominant. This behavior suggests that there is an additional peak overlapping with the first LO phonon replica of the D^dAP emission at 2.652 eV. This extra peak may be assigned to the emission associated with Te-related traps.[44] In Figure 22(b), the black spectrum represents a sample with 350 nm of (N+Te)δ^3-doped region on an 800 nm uniformly nitrogen doped ZnSe. The spectrum shows broad emission bands at about 2.65 and 2.43 eV. These broad peaks would be also attributed to Te-related emissions.[44] These broad bands may be composed of two or more overlapping emissions which correspond to excitons bound at Te clusters (Te_n) with different n values.[44] Further studies such as photoluminescence excitation, time-resolved PL and temperature-dependent PL would be needed to identify these emissions more precisely.

Thus, the concept of spatial separation of substitutional nitrogen seems plausible for increasing the solubility of substitutional nitrogen and/or reducing compensation centers which effectively suppress the maximum

Reproduced with permission of the copyright owner. Further reproduction prohibited without permission.

achievable p-type doping levels in ZnSe:N. This new approach may also be useful in enhancing the p-type doping of other Se-based II-VI materials such as $Zn_{1-x-y}Mg_xCd_ySe$ and $Zn_{1-x}Mg_xS_{1-y}Se_y$ systems where the p-type compensation effect is more severe.

In the next section, the p-type doping of $Zn_{1-x}Mg_{1-x}Se$ and $Zn_{1-y}Cd_{1-y}Se$ ternaries will be systematic studied as a function of material composition.

Reproduced with permission of the copyright owner. Further reproduction prohibited without permission.

3-6 p-type doping of $Zn_{1-x}Mg_xSe$ and $Zn_{1-y}Cd_ySe$ alloys

It has been observed that $Zn_{1-x-y}Mg_xCd_ySe$ quaternaries are difficult to dope p-type while their n-type doping is relatively easy. For example, the quaternary with a 77K bandgap energy of 2.5 eV can only be doped to a (N_A-N_D) level of about 1 x 10^{16} cm^{-3} while ZnSe with 77K E_g of 2.78 eV can be doped to the range of high 10^{17} cm^{-3} by using an rf discharge N plasma source.

As discussed in Section 3-3, solubility limits as well as several p-type compensation defects may be responsible for the p-type doping difficulties in these quaternaries. With the addition of Cd and Mg atoms, the compensation effects may become more severe. For example, Chadi et al[26] predicted that the reaction of the host-host bond-breaking compensation defect (DX-like center) in nitrogen doped MgS, MgSe, and MgTe are strongly exothermic. Furthermore, nitrogen in a MgSe lattice forms a deep hole trap (DX-like center) due to the impurity-host (N-Mg) bond breaking while that will not occur in N-Zn bonds in ZnSe lattice.[48] Thus, it is predictable that the maximum p-type doping level of nitrogen doped ZnSe-based materials may decrease as Mg atoms are added. A similar theoretical prediction of these bond-breaking defects in CdSe-based materials has not yet been reported. However, Baron et al[21] observed that the p-type doping level of ZnCdTe:N

Reproduced with permission of the copyright owner. Further reproduction prohibited without permission.

decreased drastically as the Cd concentration increased. The authors proposed that the formation enthalpy (heat) of Cd_3N_2 complexes is comparable to that of the CdTe bond in nitrogen doped ZnCdTe and thus attributed the decrease of the p-type doping level to the formation of Cd_3N_2. If this mechanism can be applied to ZnCdSe, then a decrease in p-type doping level with the increase of Cd concentration is likely. At this moment, it is not clear which mechanism dominates the compensation effects in $Zn_{1-x-y}Mg_xCd_ySe$ quaternaries. In order to understand this issue, it is useful to investigate the p-type doping of $Zn_{1-x}Mg_xSe$ and $Zn_{1-y}Cd_ySe$ ternaries as a function of material composition. Besides uniform doping, the "single" (N+Te)δ-doping has also been used in both ternaries to examine its effect.

Nitrogen doped $Zn_{1-x}Mg_xSe$ and $Zn_{1-y}Cd_ySe$ ternaries were grown on (001) p^+-GaAs substrates using an rf discharge nitrogen source. The detailed procedures about the ex-situ and in-situ preparation of the substrates have been described in Section 3-4. The growth temperature was 250 °C and the growth rate was about 0.8~1.0 μm/hr for both ternaries. All samples were grown under Se rich conditions. The RHEED pattern during the growths shows a streaky (2 x 1) surface reconstruction suggesting a preferred two-dimensional growth mode. Prior to the II-VI growth, a 15-second Zn-

Reproduced with permission of the copyright owner. Further reproduction prohibited without permission.

irradiation was used to suppress the formation of Ga-Se related complexes at the II-VI/III-V interface which could cause stacking faults.

A 0.5 μm uniformly doped ZnSe:N layer was first deposited as a buffer layer followed by the growth of 1.5 μm uniformly doped $Zn_{1-x}Mg_xSe$:N or $Zn_{1-y}Cd_ySe$:N. In some samples, the (N+Te)δ-doped layer was then grown on the uniformly doped layer. The shutter control of the (N+Te)δ-doping is similar to that of ZnSe, except for the growth of the undoped $Zn_{1-x}Mg_xSe$ or $Zn_{1-y}Cd_ySe$ spacer. The undoped spacer of each sample is about 7 MLs. Since N-Mg (and possibly N-Cd) bonds may break and form deep hole traps (DX-like centers) while Zn-N bonds are relatively stable,[26] nitrogen and Te atoms were deposited on Zn-terminated surfaces. For this purpose, Mg and Cd shutters were closed and opened as the Se one. Finally, for $Zn_{1-x}Mg_xSe$ samples, a 0.2 μm uniformly doped ZnSe:N layer is grown on the top as a cap layer to prevent oxidization of active Mg in the air.

The nitrogen source was operated under optimum conditions, at an rf discharge power of 400 W and a pure nitrogen (6N) flow corresponding to a chamber background pressure of 8 x 10^{-6} torr. The nitrogen conditions remained the same during the growth of each layer. The compositions of Mg and Cd in the ternaries were calculated from single crystal x-ray diffraction

Reproduced with permission of the copyright owner. Further reproduction prohibited without permission.

measurements by assuming a linear dependence of the lattice constant with Mg and Cd concentrations (Vegard's Law).

The (N_A-N_D) levels of both ternaries were determined by electrochemical C-V measurements. The preparation of the electrolyte for electrochemical etching was described in Chapter 2. The electrochemical etching of the ZnMgSe samples usually experiences preferential dissolution at the defect areas. A thick (1.5 μm) sample and a slow etching condition was used to minimized this problem. On the other hand, it was not possible to find an electrolyte for etching $Zn_{1-y}Cd_ySe$:N layers. However, a good electrolyte-semiconductor Schottky barrier could be still obtained. Thus the (N_A-N_D) levels of $Zn_{1-y}Cd_ySe$ samples were determined by surface C-V profiling while those of ZnMgSe samples were obtained by depth-dependent C-V profiling.

For $Zn_{1-x}Mg_xSe$ ternaries, the addition of Mg atoms increases the bandgap energy of the ternaries from 2.7 eV (ZnSe) towards 3.6 eV (MgSe). Figure 23 shows the (N_A-N_D) level of $Zn_{1-x}Mg_xSe$ samples as a function of bandgap energy (or Mg concentration). The solid circles represent the uniformly nitrogen doped samples. The (N_A-N_D) level decreases in two stages as a function of bandgap energy (or Mg concentration). Initially, below E_g=2.9 eV (x=0.2), the (N_A-N_D) level decreases slightly from 7 x10^{17} to 2 x 10^{17} cm^{-3}. Above E_g=2.9 eV, the (N_A-N_D) drops abruptly from 2 x 10^{17} to 3 x

Reproduced with permission of the copyright owner. Further reproduction prohibited without permission.

10^{15} cm^{-3} as the bandgap energy (or Mg concentration) increases from 2.9 (x=0.2) to 3.0 (x=0.35) eV. Ferreira et al[45] experimentally proved that the addition of Mg to ZnSe increases the bandgap by only lifting the position of the conduction band minimum (CBM) while the valence band maximum (VBM) remains constant with respect to the vacuum level.[45] Since the $VBM_{ZnMgSe}=VBM_{ZnSe}$, the maximum achievable hole concentration of ZnMgSe:N ternaries should be a constant for different Mg concentration according to the amphoteric defect model[42] in II-VI materials, described in Section 3-3. The data shown in Figure 23 do not follow the prediction of the model suggesting that other factors dominate the p-type doping in these materials. A similar E_g-dependent decrease of the (N_A-N_D) level (decreasing in two stages) was observed in the $Zn_xMg_{1-x}S_ySe_{1-y}$ quaternaries by other groups. The change in slope occurs at a similar bandgap ($E_g \sim 2.9$ eV) even

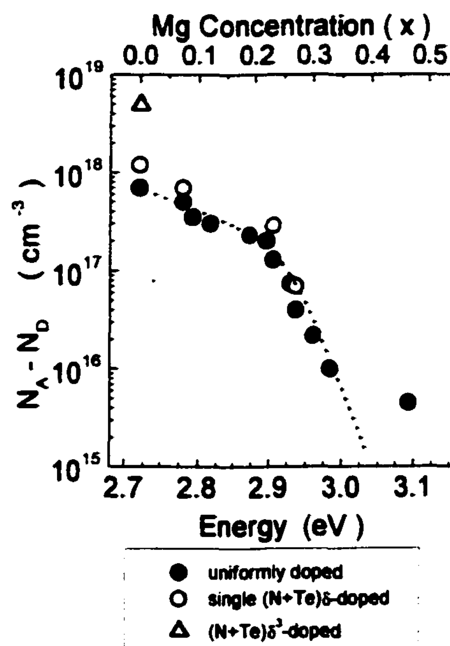

Figure 23 (N_A-N_D) level of $Zn_{1-x}Mg_xSe$:N vs bandgap energy (or Mg concentration). The solid circles represent the uniformly doped ZnMgSe:N while the blue open circles are for the (N+Te)δ-doped samples. The open triangle is for (N+Te)δ^3-doped ZnSe as a reference point.

Reproduced with permission of the copyright owner. Further reproduction prohibited without permission.

though the Mg concentration in the $Zn_xMg_{1-x}S_ySe_{1-y}$ quaternaries (<0.12) is lower than in the $Zn_{1-x}Mg_xSe$ ternaries (0.25). This suggests that a compensation center is activated as the bandgap energy becomes larger than 2.9 eV.[14] The blue open circles represent the (N_A-N_D) level of the (N+Te)δ-doped $Zn_{1-x}Mg_xSe$ samples. Some enhancement is evident but the (N_A-N_D) level still follows the same trend suggesting that the dominant compensation defect is still active.

In contrast to $Zn_{1-x}Mg_xSe$, the bandgap energy of $Zn_{1-y}Cd_ySe$ ternaries decreases from 2.7 eV (ZnSe) to 1.8 eV (CdSe) as the Cd concentration increases. Figure 24 shows the (N_A-N_D) levels of $Zn_{1-y}Cd_ySe$ samples as a function of the Cd concentration. The solid circles represent the data of uniformly doped $Zn_{1-y}Cd_ySe$:N. Their (N_A-N_D) levels decrease drastically from 7 x 10^{17} to 5 x 10^{15} cm^{-3} as the Cd concentration increases from y= 0 to 0.27. It is known that the addition of

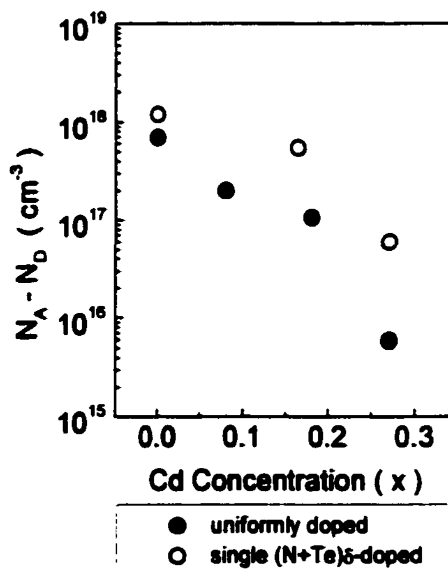

Figure 24 (N_A-N_D) level of $Zn_{1-y}Cd_ySe$:N vs Cd concentration. The solid circles represent the uniformly doped sample while those open circles are for the (N+Te)δ-doped samples.

Reproduced with permission of the copyright owner. Further reproduction prohibited without permission.

Cd in ZnSe raises the VBM position on an absolute energy scale. In general, a high VBM position facilitates the p-type doping. Thus, the decrease of the (N_A-N_D) level with the addition of Cd suggests that a compensation defect was introduced by the addition of Cd atoms. Several of the $Zn_{1-y}Cd_ySe$:N samples were grown on InP substrates. No difference in the behavior was observed even when the ternary is lattice-matched to the substrate and therefore has higher crystalline quality.

A similar decrease in (N_A-N_D) level as a function of Cd concentration was observed in the uniformly doped ZnCdTe:N system by Baron et al.[21] The authors proposed that nitrogen atoms prefer to form a Cd_3N_2 complex rather than substitute in Te sites during the nitrogen doping of ZnCdTe and attributed the decrease of the p-type doping efficiency to the preferential formation of the nitride complex. The growth interruption during nitrogen deposition in the δ-doping technique should be able to avoid the formation of nitride complexes. The open circles in Figure 24 represent the (N_A-N_D) data of (N+Te)δ-doped samples. By using the (N+Te)δ-doping technique, more significant enhancements in doping levels were observed in the $Zn_{1-y}Cd_ySe$ ternary than in $Zn_{1-x}Mg_xSe$. For example, the (N_A-N_D) level of $Zn_{0.73}Cd_{0.27}Se$ was increased about one order of magnitude (from 6×10^{15} to 6×10^{16} cm^{-3})

Reproduced with permission of the copyright owner. Further reproduction prohibited without permission.

while that of $Zn_{0.73}Mg_{0.27}Se$ was increased by less than a factor of two (from 4×10^{16} to 7×10^{16} cm^{-3}). This suggests that (N+Te)δ-doping is effective in suppressing a compensation center (possibly nitride complexes) in the ZnCdSe ternary. However, the doping level still decreases rapidly as a function of Cd content in the $Zn_{1-y}Cd_ySe$ layers. This suggests that some types of compensation defects are still active and cannot be completely eliminated.

It is now clear that Cd and Mg atoms may either introduce a new type of compensation mechanism or make some existing compensation mechanism become more severe. For example, the compensation defects present in ZnSe:N, such as N_{Se}-V_{Se} complex, nitride complexes, and host-host bond-breaking defects, may remain or become even more severe when Cd and Mg are added. Moreover, another compensation defect such as the impurity-host bond breaking defect (DX-center), which is not likely to occur in ZnSe:N, may become effective with the addition of Cd and Mg atoms. It is reasonable to imagine that the compensation mechanisms in $Zn_{1-x-y}Mg_xCd_ySe$ quaternaries should be somehow a mixture of those present in the two ternaries. We propose that, to enhance the p-type doping of the quaternaries more significantly, the doping should be performed in regions without Mg and Cd atoms. For this purpose, we propose a ZnMgCdSe/ZnSe:N superlattice structure, in which the p-type doping is only performed in the ZnSe region, as

Reproduced with permission of the copyright owner. Further reproduction prohibited without permission.

a substitute for the typical p-type quaternary cladding in a laser structure. For the fabrication of a high performance laser diodes, the p-type cladding layer with doping level in the range of 10^{17} cm^{-3} is required. We may also apply the (N+Te)δ^3-doping technique in the ZnSe region of the superlattice to further enhance the p-type doping level in the superlattice.

Reproduced with permission of the copyright owner. Further reproduction prohibited without permission.

Chapter 4

p-type Ohmic Contact Layer:

$ZnSe_{0.53}Te_{0.47}$ Alloy Lattice-matched to InP

4-1 MBE growth of $ZnSe_{1-x}Te_x$ alloys on InP substrates

$ZnSe_{1-x}Te_x$ alloys have significant potential importance in both material research and device applications. Since ZnSe can be readily doped n-type and ZnTe can be readily doped p-type, it has been proposed that $ZnSe_{1-x}Te_x$ alloys of some compositions may be able to be doped both p-type and n-type.[1] One of the factors that plays a role in the p-type doping behavior of semiconductors is the valence band maximum (VBM) position on an absolute energy scale. Due to the significant VBM offset (~1 eV) between ZnSe and ZnTe, it is of interest to investigate the p-type doping behavior of $ZnSe_{1-x}Te_x$ alloys as a function of Te concentration. To date, no systematic study of the doping of $ZnSe_{1-x}Te_x$ alloys has been reported. One of the reasons for this is the difficulty to obtain these materials in high quality and with good compositional control.[2] A $ZnSe_{0.53}Te_{0.47}$ layer lattice-

Reproduced with permission of the copyright owner. Further reproduction prohibited without permission.

matched to InP may be used as a p-type contact layer if good compositional control can be achieved and high p-type doping can be reproducibly obtained. In this section, we present the molecular beam epitaxial (MBE) growth of $ZnSe_{1-x}Te_x$ alloys with a wide range of Te and Se fractions grown on InP substrates with high crystalline quality and good compositional control.

The layers were grown on InP substrates by MBE. Knudsen effusion cells installed on a Riber MBE 2300 growth chamber were used for elemental sources including Zn(6N), Cd(6N), Se(6N), and Te(6N). The ex-situ preparation for InP substrates has been described in Chapter 2. The thermal deoxidization and growth were monitored by in-situ reflection high energy electron diffraction (RHEED). Prior to the growth of $ZnSe_{1-x}Te_x$, an InGaAs (100 nm) buffer layer was deposited on the deoxidized InP substrates. This was followed by a low temperature (LT) ZnCdSe (10 nm) buffer layer. Both buffer layers were nominally lattice-matched to the InP substrates. The InGaAs buffer layer was grown at 480 °C with an In/Ga beam equivalent pressure (BEP) ratio of 2, under an As overpressure. The LT-ZnCdSe buffer layer was grown at 170 °C while the growth temperature of the $ZnSe_{1-x}Te_x$ layers was 250 °C. The BEP of each II-VI element, which is proportional to the flux, was measured by an ion gauge placed in the

Reproduced with permission of the copyright owner. Further reproduction prohibited without permission.

position of the substrate before the growth of the LT-ZnCdSe buffer layer. For the ZnCdSe layer, the Cd/Zn BEP ratio used was about 2 with a Se overpressure 4 times larger than the sum of the Zn and Cd BEP. As will be discussed below, a Se/Zn BEP ratio of ~1 was used for the growth of the $ZnSe_{0.53}Te_{0.47}$ lattice matched to InP. The growth rate of the $ZnSe_{1-x}Te_x$ layers was about 0.8 μm/hr. All samples have thickness of 1.5~2 μm. Due to the different growth conditions for $ZnSe_{1-x}Te_x$ and LT-ZnCdSe layers, the Zn and Se cell temperatures must be adjusted after the growth of the LT-ZnCdSe buffer layer. A long growth interruption (about 20 min) after the adjustment of the cell temperatures is necessary to stabilize the Zn and Se fluxes and reduce the Se background pressure which may affect the control of the initial Se concentration in the $ZnSe_{1-x}Te_x$ alloy. Due to the preferential incorporation of Se over Te, the Se/Te ratio in the solid was difficult to control by adjusting the Se/Te flux (or BEP) ratio.[4] However, the Se and Te concentrations in $ZnSe_{1-x}Te_x$ layers could be precisely controlled by adjusting the Se/Zn BEP ratio, with an excess of Zn at the surface.[15] The layers were grown under Te-rich conditions with the Te BEP about 1.5 times larger than that of Zn, which is the optimum condition for ZnTe growth. A streaky (2x1) RHEED pattern was observed during the growth suggesting a preferred two dimensional growth mode. Too high a Te BEP did not

Reproduced with permission of the copyright owner. Further reproduction prohibited without permission.

significantly change the Te content in the $ZnSe_{1-x}Te_x$ layers but degraded the growth front and the crystalline quality of the layer, as indicated by the development of a spotty RHEED pattern after about 1 hour of growth.

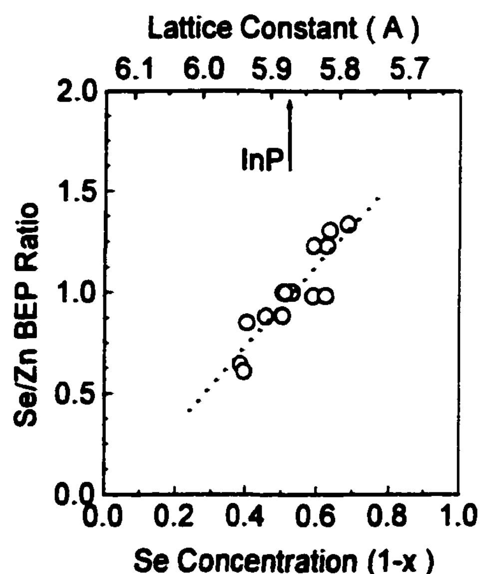

Figure 1 Se concentration in $ZnSe_{1-x}Te_x$ alloys as a function of Se/Zn BEP ratio used during MBE growth. The dashed line shows near proportional relation determined by a least-squares fit.

Figure 1 shows the Se content in the solid (1-x) in the region of 40% to 70% Se as a function of the Se/Zn BEP ratio used during growth. Values of x and 1-x are calculated from the measured lattice constant assuming Vegard's law. All the available Se incorporates as long as there is an excess of Zn, thus the Se concentration in $ZnSe_{1-x}Te_x$ alloys is proportional to the Se flux for a constant growth rate (determined by the Zn flux). The excess Zn determines the Te fraction. Additional Te is desorbed and simply maintains group VI rich conditions at the growth surface. The data in Figure 1 show some deviation from the ideal behavior indicated by the dashed line. We propose that this variation in the composition control (on the order of $\pm$ 0.06 in x) may be reduced by using two different Se cells with fixed temperatures for the growths of the LT-

Reproduced with permission of the copyright owner. Further reproduction prohibited without permission.

ZnCdSe buffer and the $ZnSe_{1-x}Te_x$, respectively. As indicated in Figure 1, the $ZnSe_{0.53}Te_{0.47}$ alloy lattice-matched to InP is obtained when the Se/Zn BEP ratio equals about 1.

Single and double crystal x-ray rocking curves were used to determine the lattice constant and to evaluate the crystalline quality of single layers of $ZnSe_{1-x}Te_x$ on InP. Figure 2(a) shows the single crystal x-ray diffraction scan of a 1.5 μm layer of $ZnSe_{0.62}Te_{0.38}$ ($\Delta a/a$=-0.6%). The strong and well-resolved $K_{\alpha 1}$ and $K_{\alpha 2}$ peaks from the epitaxial layer suggest its single crystalline quality. Figure 2(b) is the (004) reflected double crystal x-ray rocking curve (DCXRC) of the same sample taken at two different positions on the wafer. The similarity between the two scans indicates good uniformity throughout the layer. The peaks at 739 and 871 arcsec are assigned to the ZnSeTe layer in agreement with the data in Figure 2(a). They suggest the presence of two regions of slightly different Se content [(1-x) = 0.612 and 0.626] as a function of depth. Figure 2(c) and 2(d) are the corresponding single and double crystal x-ray data for another ZnSeTe layer. In this case, the single crystal scan [Figure 2(c)] exhibits only one set of peaks ($K_{\alpha 1}$ and $K_{\alpha 2}$) indicating near lattice-matching of the layer and the substrate. The DCXRC in Figure 2(d) shows a single small peak from the ZnSeTe layer which appears as a shoulder on the substrate peak, suggesting

Reproduced with permission of the copyright owner. Further reproduction prohibited without permission.

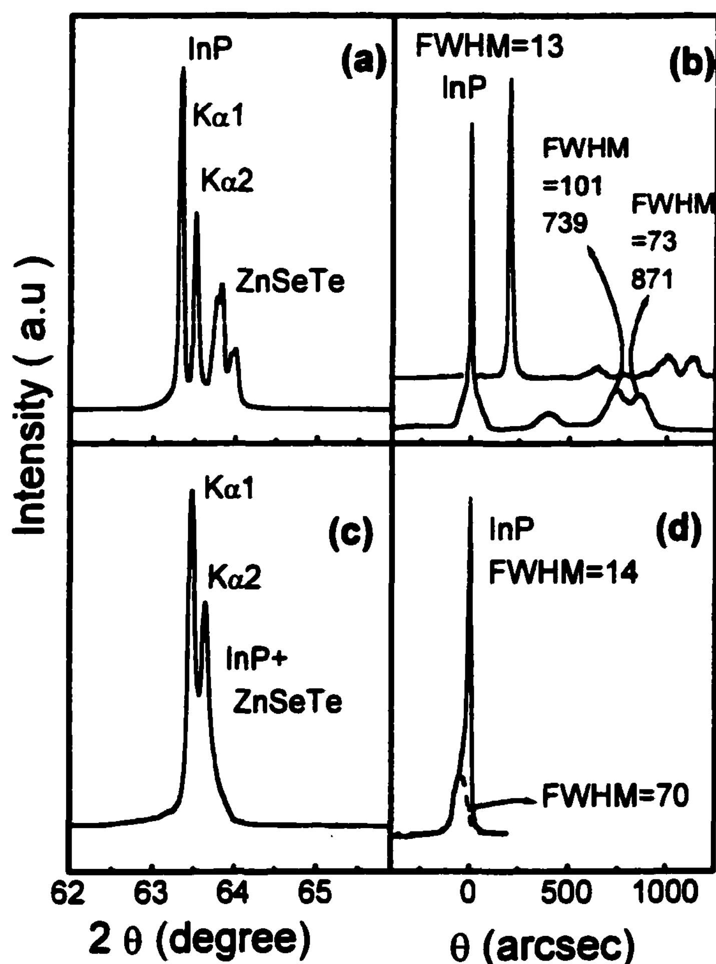

Figure 2 (a) Single crystal x-ray diffraction spectrum of the $ZnSe_{0.62}Te_{0.38}$ alloy. (b) Double crystal x-ray rocking curve of the sample in (a) taken at two different regions of the wafer. The top scan is intentionally shifted by 250 arcsec for clarity. (c) Single crystal scan of a $ZnSe_{0.53}Te_{0.47}$ layer. (d) Double crystal rocking curve for the sample in (c).

a uniform ZnSeTe layer composition. The full width at half maximum (FWHM) of the DCXRC peaks are 70-100 arcsec, the narrowest reported values for $ZnSe_{1-x}Te_x$ alloys indicating high crystalline quality.[5]

Since the concentration of Se is highly sensitive to the Se/Zn BEP ratio, the presence of a double x-ray peak in some samples may be due to Se

Reproduced with permission of the copyright owner. Further reproduction prohibited without permission.

flux fluctuations during the growth. We estimate that the concentration difference between the two peaks in Figure 2(b) corresponds to about 0.5 °C temperature fluctuation of the Se cell. A Se cracker cell is expected to provide more accurate control of the Se flux for a more uniform layer composition.

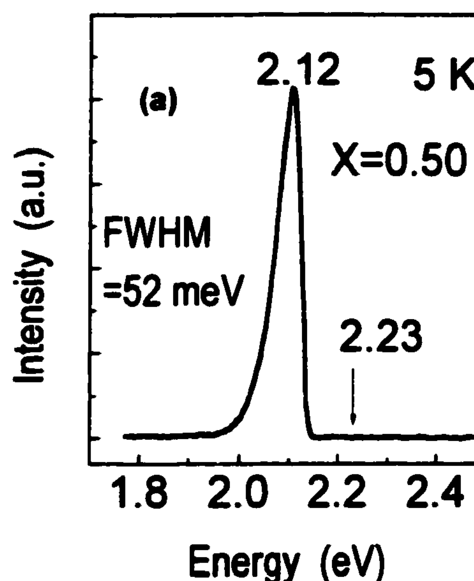

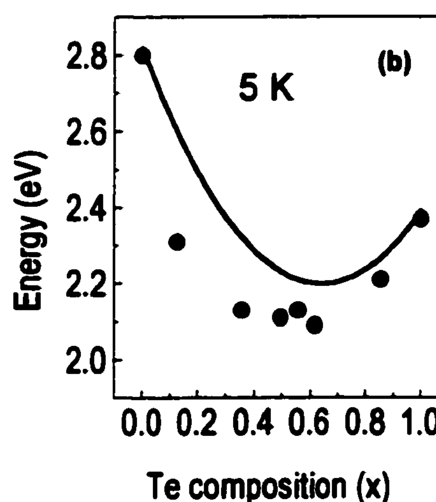

Figure 3 (a) 5K PL spectrum of the nitrogen doped $ZnSe_{0.50}Te_{0.50}$ alloy. The arrow indicates the position of the calculated 5K bandgap for this alloy. (b) Energy of 5K PL peak of $ZnSe_{1-x}Te_x$ alloys as a function of Te content (x). (Points at x=0, 0.35, 0.85 and 1 represent undoped samples, the rest are nitrogen doped). The solid curve represents the 5K bandgap of $ZnSe_{1-x}Te_x$ alloys calculated from the empirical formula of Ref. 7.

Photoluminescence (PL) measurements were performed using the single line at 325 nm of a He-Cd laser. Figure 3(a) shows the 5K PL spectrum of a $ZnSe_{0.50}Te_{0.50}$ layer. This particular layer is nitrogen doped to a level of mid 10^{16} cm^{-3}. No significant difference in the 5K PL spectrum is observed between nitrogen doped samples and undoped samples of similar composition.[6] The

Reproduced with permission of the copyright owner. Further reproduction prohibited without permission.

PL spectrum exhibits a strong dominant peak at 2.12 eV with FWHM of 52 meV and no deep level emission. The dominant PL emission has an energy 110 meV below that of the 5K bandgap which is calculated to be about 2.23 eV.[7] The dominant peak positions of the 5K spectra of $ZnSe_xTe_{1-x}$ layers having a range of Te concentrations are plotted in Figure 3(b) as a function of the Te fraction in the layers. As indicated in the figure caption, some of the layers are nitrogen doped and some are undoped. The data are in good agreement with those previously reported in the literature.[6] The solid curve in Figure 3(b) represents the calculated 5K bandgap of $ZnSe_{1-x}Te_x$ alloys using the empirical formula, $E_g(5K) = 1.507\ x^2 - 1.935\ x + 2.820$.[7] The PL data as well as the calculated curve shows the strong bowing property of the emission of $ZnSe_{1-x}Te_x$ as a function of Te concentration.[7] As previously reported, the PL emission of the alloy originates from a level within the gap. All samples, except ZnTe and ZnSe, show a dominant broad deep level emission without narrow excitonic emission lines. This deep emission has been attributed to the presence of Te clusters in the alloys.[8,9] The PL emission energies of our samples all lie below the calculated bandgap by a few meV to 300 meV depending on the concentration of Te. In general, the emission linewidth and its deviation from the bandgap decrease as the Te concentration increases.[6]

Reproduced with permission of the copyright owner. Further reproduction prohibited without permission.

High quality $ZnSe_{1-x}Te_x$ alloys with good compositional control have been achieved. To date, no data of the p-type doping in these alloys have been reported in literature. It is not clear how much Te is needed in the alloys so that the p-type doping in these materials becomes easier. As a p-type contact layer, it would be desirable that the p-type doping of lattice-matched $ZnSe_{0.53}Te_{0.47}$ alloys be more like that of ZnTe. In the next section, p-type doping of $ZnSe_{1-x}Te_x$ alloys using an rf discharge nitrogen source will be systematically studied as a function of Te concentration.

Reproduced with permission of the copyright owner. Further reproduction prohibited without permission.

4-2 p-type doping of $ZnSe_{1-x}Te_x$ using an rf discharge nitrogen plasma source

A systematic study of p-type doping of $ZnSe_{1-x}Te_x$ alloys with Te contents from 0% to 100% using a radio frequency- (rf-) discharge nitrogen plasma source has been performed. The p-type $ZnSe_{1-x}Te_x$ alloys were grown on semi-insulating InP substrates. Prior to the II-VI growth, a n-type (Si-doped) lattice-matched InGaAs was grown as a buffer layer where Si doping was used to prevent the electrical conductivity of the InGaAs buffer layer to interfere with our Hall effect measurements. In the II-VI chamber, 0.5 μm undoped $ZnSe_{1-x}Te_x$ was first grown followed by 1.5 μm nitrogen doped layer. Two different conditions for the discharge nitrogen plasma source were used. Condition I has an input power fixed at 250 W with nitrogen background pressure in the growth chamber of 2×10^{-6} torr while condition II, the optimum doping conditions, has 400 W input power and an 8×10^{-6} torr background pressure in the chamber. The electrical properties were characterized by Hall effect measurement and the electrochemical C-V (ECV) profiling. The contacts for Hall effect were prepared by simply depositing Au or In on the surface of samples. The details about the Hall effect measurement have been described in Chapter 2. For samples grown on semi-insulating substrates, the front contact method (described in Chapter 2)

Reproduced with permission of the copyright owner. Further reproduction prohibited without permission.

was used for ECV profiling which determines the (N_A-N_D) level of those samples. For samples with high doping level (~10^{19} cm^{-3}), a good ohmic contact can be obtained by applying a 40 V ac pulse for a duration of 150 ms between the spring loaded wires of the front contact. For samples with low doping level, the ohmic front contact can be obtained by the same way as those of Hall effect measurement (using Hg:In alloys) followed by a blast high voltage ac pulse.

Figure 4 shows the free hole (indicated by circles) and net acceptor concentrations (indicated by triangles) of $ZnSe_{1-x}Te_x$ alloys as a function of Te content. The free hole concentration of the alloys using condition II, measured by Hall effect at room temperature, increases abruptly from 10^{17} to 10^{19} cm^{-3} as the Te content increases from 12% to 40%. A similar abrupt increase in free hole concentration is seen in the samples doped using condition I, the

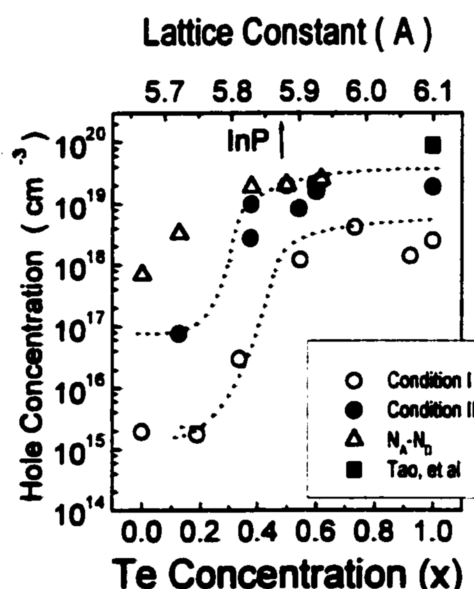

Figure 4 Free hole concentrations for $ZnSe_{1-x}Te_x$ alloys doped with N under two different N plasma source conditions (circles). The triangles represent the net acceptor concentration of $ZnSe_{1-x}Te_x$ alloys measured by ECV for samples grown under condition II. The dashed lines are drawn to aid the eye. The square represents the value for N doped ZnTe reported by I.W. Tao, et al.[11]

Reproduced with permission of the copyright owner. Further reproduction prohibited without permission.

only difference being that the curve is shifted to a lower free hole concentration range. The abrupt increase in free hole concentration may be correlated with the pronounced bowing property of bandgap energy in $ZnSe_{1-x}Te_x$ system as shown in Figure 3(b) of Section 4-1. It has been observed that the valence band offset between ZnSe and ZnTe is about 0.8 eV, which is even bigger than the difference of their bandgap energies [E_g(ZnSe)=2.7 eV and E_g(ZnTe)=2.4 eV].[13] The valence band maximum (VBM) in an absolute energy scale is an important factor determining the maximum free hole concentration that can be achieved in a semiconductor.[14] Based on these considerations, we suggest that the abrupt increase in free hole concentration may be correlated with the transition of the VBM positions from ZnSe-like to ZnTe-like. Further investigations such as the measurement of the VBM positions in an absolute energy scale as a function of Te concentration, may help to understand the behavior illustrated in Figure 4.

The net acceptor concentrations (N_A-N_D) for the samples doped using condition II are also shown in Figure 4 (empty triangles). The net acceptor concentration was measured by ECV measurements. As indicated in Figure 4, ZnSe has a net acceptor concentration of 7 x 10^{17} cm^{-3} while $ZnSe_{1-x}Te_x$ with only 12% Te has a (N_A-N_D) level of 4 x 10^{18} cm^{-3}. This value of (N_A-N_D)

Reproduced with permission of the copyright owner. Further reproduction prohibited without permission.

level for the 12% Te alloy is about one order of magnitude higher than the free hole concentration for the same alloy composition. The free hole concentration of the 12% Te alloy is similar to that of a uniformly nitrogen doped ZnSe/ZnTe short period superlattice of a similar average composition (Te~12%).[2] At 40% Te, the (N_A-N_D) value increases to ~2 x 10^{19} cm^{-3} and remains approximately constant for higher Te content. In this range, the free hole concentrations and the net acceptor concentrations become nearly equal.

Several observations may be drawn from this data. For high Te content samples (greater than 40% Te), the free carrier concentrations are high and nearly equal to the net acceptor levels suggesting full ionization of holes at room temperature. In this range, the acceptor levels remain constant, possibly due to being near the solubility limit of N in this material.[10] The value indicated by the square, the highest reported value for N doped ZnTe,[11] is given as comparison. In samples with less Te, there is about one order of magnitude difference between the net acceptor and free hole concentrations indicating either increased compensation or a reduced ionization fraction of holes. This may be due to several factors, such as high acceptor binding energies, the position of the valence band maximum in an absolute energy scale or the presence of compensating mechanisms in the low Te content materials. As described in Section 2-4-3, it should be noted that the presence

Reproduced with permission of the copyright owner. Further reproduction prohibited without permission.

of significant compensation in the samples with low Te content may result in the failure of Eq. (4) in Section 2-4-3 to describe the material accurately and thus introduce significant errors in the values of free hole concentration. Finally, the composition lattice-matched to InP, $ZnSe_{0.53}Te_{0.47}$, has a free hole concentration of 2 x 10^{19} cm^{-3}, with a hole mobility of 3-4 cm^2/V sec. The value of the mobility is in agreement with other II-VI materials having such high hole concentration (i.e. ZnTe is 8.2 cm^2/V sec for 8.9 x 10^{19} cm^{-3}).[11] These electrical properties suggest that $ZnSe_{0.53}Te_{0.47}$ can be used as a p-type ohmic contact layer.

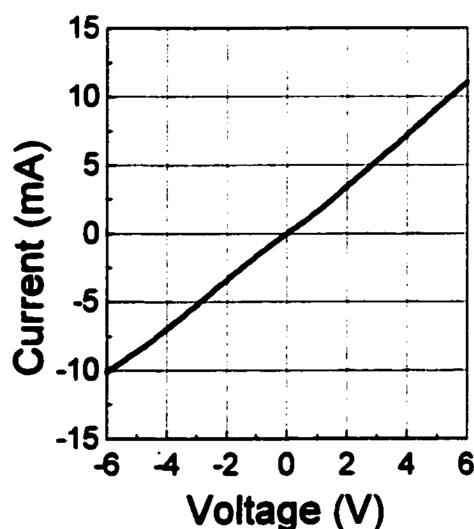

Figure 5 Current-voltage characteristics between two contacts on a lattice-matched $ZnSe_{0.53}Te_{0.47}$:N sample. The linear behavior between I and V suggests an ohmic contact.

Figure 5 shows the I-V characteristics between two In contacts deposited on the surface of a lattice-matched $ZnSe_{0.53}Te_{0.47}$:N sample, which has free hole concentration of 2 x 10^{19} cm^{-3}. The linear I-V behavior indicates that ohmic contacts are obtained by simply depositing In drops. This demonstrates that the lattice-matched $ZnSe_{0.53}Te_{0.47}$ can be used as an ideal p-type contact layer in the

Reproduced with permission of the copyright owner. Further reproduction prohibited without permission.

ZnMgCdSe LED or diode laser structures, based on its electrical properties as well as its lattice matching characteristics. Recently, ZnCdSe/ZnMgCdSe QW LEDs with good I-V characteristics have been made by the incorporation of such a highly p-type doped $ZnSe_{0.53}Te_{0.47}$ contact layer.[12] The LED results will be addressed in the next chapter.

Reproduced with permission of the copyright owner. Further reproduction prohibited without permission.

Chapter 5

ZnCdSe/ZnMgCdSe Quantum Well Light Emitting Diodes

5-1 MBE growth of full-color LEDs

It has been shown that totally lattice-matched or pseudomorphic photo-pumped lasers can be fabricated with the $Zn_{1-x-y}Mg_xCd_ySe$ system on InP substrates. By only changing the width and/or composition of the ZnCdSe active layer, these photo-pumped lasers can emit light in the red, green and blue colors; the three primary colors needed for full color applications.[1] This is evidence that the ZnCdSe/ZnMgCdSe QW system lattice-matched to InP has potential to fabricate light emitting devices in the full color range and on a single InP substrate. Through earlier results and those presented in the previous chapters, we have achieved the essential requirements for fabrication of the ZnCdSe/ZnMgCdSe QW LEDs, although higher p-type doping levels of $Zn_{1-x-y}Mg_xCd_ySe$ quaternaries would be

Reproduced with permission of the copyright owner. Further reproduction prohibited without permission.

Bandgap emission range	2.0-3.0 eV
Defect densities	$< 5 \times 10^4$ cm^{-2}
ZnMgCdSe n-type doping (free electron)	$> 1 \times 10^{18}$ cm^{-3}
ZnMgCdSe p-type doping (N_A-N_D)	$\sim 1 \times 10^{16}$ cm^{-3}
$ZnSe_{0.53}Te_{0.47}$ p-type doping (free hole)	$> 1 \times 10^{19}$ cm^{-3}

Table 1 Materials parameters relevant for LED fabrication of $Zn_{1-x-y}Mg_xCd_ySe$ structures lattice-matched to InP.

desirable. Those accomplishments include the growth of high quality $Zn_{1-x-y}Mg_xCd_ySe$ quaternaries lattice-matched to InP with etch pit (stacking fault) density of ~ 5×10^4 cm^2, n-type doping of the quaternaries (free electron concentration of above 1×10^{18} cm^{-3}), p-type doping of $Zn_{1-x-y}Mg_xCd_ySe$ layers [(N_A-N_D) ~ 1×10^{16} cm^{-3}] and the highly p-type doped $ZnSe_{0.53}Te_{0.47}$:N alloy as an ohmic contact layer lattice-matched to InP with a free hole concentration of 2×10^{19} cm^{-3}. Despite the relatively low doping level of the p-type quaternary layer, in this chapter we combine these results to fabricate LEDs from the ZnCdSe/ZnMgCdSe QW system by MBE and investigate their I-V and electroluminescence properties. The materials parameters relevant for LED fabrication of $Zn_{1-x-y}Mg_xCd_ySe$ structures lattice-matched to InP are summarized in Table 1.

Figure 1 shows a schematic diagram of the structure of the ZnCdSe/ZnMgCdSe QW LEDs we fabricated. The LED structure (Figure 1)

Reproduced with permission of the copyright owner. Further reproduction prohibited without permission.

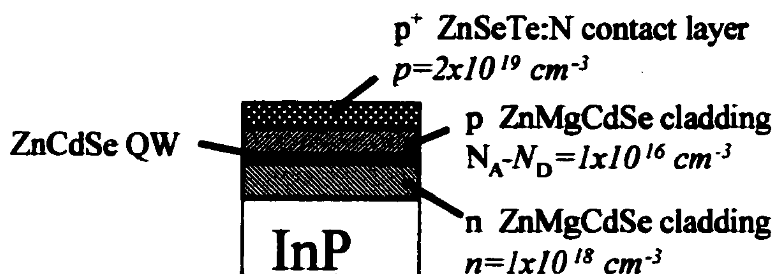

Figure 1 Schematic diagrams of the LED structures made from ZnCdSe/ ZnMgCdSe QW system.

contains a highly p-type doped $ZnSe_{0.53}Te_{0.47}$ contact layer, n-type and p-type doped $Zn_{1-x-y}Mg_xCd_ySe$ cladding layers, and a ZnCdSe QW active layer.

MBE growth of these LED structures was performed on n^+ InP (001) substrates. The InP substrate was thermally deoxidized in the III-V chamber followed by the growth of an n-type lattice-matched InGaAs:Si ($n \sim 1 \times 10^{18}$ cm^{-3}) buffer layer (~100 nm). The growth of the II-VI material was performed under Se-rich conditions with a VI/II beam equivalent pressure ratio of ~4. The growth was initiated at a low temperature (LT) of 170 °C by growing a ~5 nm ZnCdSe interfacial layer. Then, the temperature was raised to the growth temperature of 270 °C with a 4-minute interruption, after which the desired structure was grown. This procedure has been shown in the past to produce high quality quaternary layers.[2] A 500 nm $Zn_{1-x-y}Mg_xCd_ySe$:Cl n-type cladding layer ($n = 1 \times 10^{18}$ cm^{-3}) was deposited on the LT-ZnCdSe buffer layer followed by the growth of a ZnCdSe QW layer. After that, a 100 nm $Zn_{1-x-y}Mg_xCd_ySe$:N p-type cladding layer [(N_A-N_D)

Reproduced with permission of the copyright owner. Further reproduction prohibited without permission.

~ 1 x 10^{16} cm^{-3}] was then deposited on the QW layer followed by the growth of a lattice-matched and highly p-type doped $ZnSe_{0.53}Te_{0.47}$:N contact layer (p= 2 x 10^{19} cm^{-3}). The composition of both quaternary cladding layers was such that it was lattice-matched to the InP substrate; their bandgap was about 2.9 eV. The thickness and the composition of the ZnCdSe QW layer were chosen according to the desired emission range. In the range from blue to yellow, the lattice-matched ZnCdSe composition with a nominal bandgap of 2.1 eV was used. The emission energy was tuned by changing the ZnCdSe QW thickness. For red emission, a lattice-mismatched (1.2%) ZnCdSe QW layer with a thickness of 10 nm was used. The p-type quaternary layer was only 100 nm thick in order to minimize the device resistance. The thickness of the $ZnSe_{0.53}Te_{0.47}$:N contact layer was varied between 15-100 nm. The optimum value is about 15-20 nm in terms of luminescence properties of the devices as will be discussed later. The characterization of these devices will be presented in the next section.

Reproduced with permission of the copyright owner. Further reproduction prohibited without permission.

5-2 Characteristics of ZnMgCdSe-based LEDs

The LEDs were fabricated by depositing either a Au or an In dot on the surface and attaching Au wires to the back n^+ InP substrate surface and the top metal contact. The size of the In dot varied while the Au dot was ~0.3 mm^2. No post-deposition annealing of the metal contact was performed. Both of Au and In can form ohmic contacts on the highly p-type doped and lattice-matched $ZnSe_{0.53}Te_{0.47}$:N contact layer of these devices, as shown in Chapter 4. The I-V characteristics of the LEDs and diode layers were measured with a Keithley 236 source unit. For the LEDs, the surface electroluminescence (EL) emission under pulsed operation at various current levels, was collected by a microscope objective and focused onto an optical multi-channel analyzer to analyze the spectral characteristics of the device.

Three LED structures were grown with the different QW layer

LED Color	*QW* $\Delta a/a$ *(to InP)*	*QW Thickness*	*EL (300 K) Energy*	*EL (300 K) FWHM*
Blue-green	< 0.2 %	2 nm	2.358 eV	78 meV
Yellow	< 0.2 %	6 nm	2.244 eV	70 meV
Red	1.2 %	10 nm	1.967 eV	90 meV

Table 2 Parameters for the three LED structures investigated in this section.

Reproduced with permission of the copyright owner. Further reproduction prohibited without permission.

parameters given in Table 2. The QW thickness values given in Table 2 are nominal values based on measured growth rates of similar ZnCdSe thick layers and the growth time used for the QW growth. The lattice mismatch values ($\Delta a/a$) are calculated from x-ray diffraction spectra of thick (~1 μm) ZnCdSe layers with the same composition as the QW. The QW parameters used were selected in an attempt to obtain emission spanning a broad range of the visible spectrum. Table 2 also lists the EL properties of the three structures.

Figure 2 shows the I-V characteristics of one of these LEDs having a Au contact. The thickness of the $ZnSe_{0.53}Te_{0.47}$ (15-100 nm) had no significant effect on the I-V characteristics of the diodes. Low turn-on voltage (< 4 V), no reverse breakdown of the devices even at voltages below –10 V, and output currents of ~100 mA at 5 V were typically observed for these simple LED structures. Based on this I-V curve, the estimated device resistance is not substantially

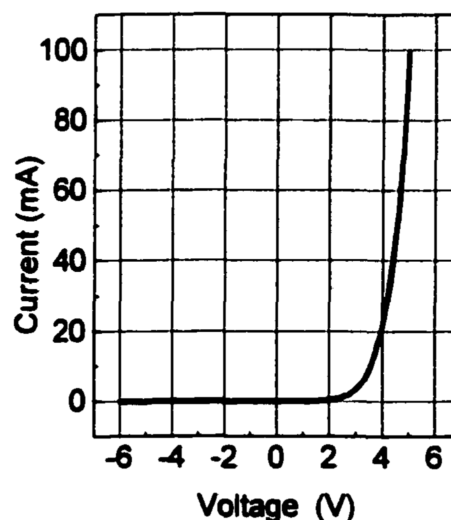

Figure 2 Current-Voltage (I-V) characteristics of a ZnMgCdSe-based LED structure with Au contact. The top contact is an Au dot (~0.3 mm^2).

Reproduced with permission of the copyright owner. Further reproduction prohibited without permission.

greater than that of commercial III-V based LEDs emitting in the yellow-green to red region.

The EL spectrum was measured from the top surface near the edge of the contact, under pulsed operation of the device at 100 mA with 100 ns and 0.1 % duty cycle. Quantum efficiency measurements are not possible with this simple geometry since most of the emission is lost within the contact region. Initially the EL measurements were made on the as-grown wafers, some of which had 100 nm thick $ZnSe_{0.53}Te_{0.47}$ p^+ contact layers. In those structures a broad red emission EL was observed regardless of the QW thickness. The solid line in Figure 3 shows the EL spectrum of one of these diodes. A broad EL band is observed centered at 1.835 eV. The sample was then etched by a 0.1 % Br_2/Methanol solution at 0 °C. The etching rate for $ZnSe_{0.53}Te_{0.47}$ is about 1.3 nm/sec calibrated by the use of an Alpha-Step 200 surface profiler.

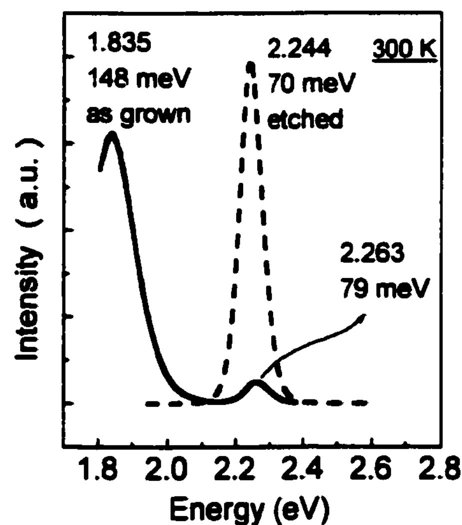

Figure 3 Surface electroluminescence (EL) spectra for an LED structure with a thick (100 nm) $ZnSe_{0.53}Te_{0.47}$ p^+ contact layer (solid curve). The dashed line represents the EL for the same structure after etching the top $ZnSe_{0.53}Te_{0.47}$ layer to 15 nm. The broad red emission in the as-grown structure originates from the $ZnSe_{0.53}Te_{0.47}$ cap layer and not from the QW.

Reproduced with permission of the copyright owner. Further reproduction prohibited without permission.

Based on the experimental results, the optimum thickness of the $ZnSe_{0.53}Te_{0.47}$ contact layer is about 15-20 nm in terms of both good contact and QW EL emissions.

After the chemical thinning the red emission was removed and the QW-related EL peak could be clearly observed. The EL spectrum of the same structure after etching of the $ZnSe_{0.53}Te_{0.47}$ layer down to a thickness value of ~20 nm is shown by the dashed line in Figure 3. This result indicates that most of the QW emission is absorbed by the thick (100 nm) $ZnSe_{0.53}Te_{0.47}$ layer, which then exhibits a very strong and dominant re-emission. The room-temperature bandgap of lattice-matched $ZnSe_{0.53}Te_{0.47}$ is expected to be at about 2.1 eV, thus, absorption of the QW emission is likely to occur for yellow, green or blue LEDs. $ZnSe_{0.53}Te_{0.47}$ layers of the lattice-matched composition exhibit a broad PL emission from isoelectronic centers within the gap, at about 2.0 eV.[8] The observed emission from the LEDs is somewhat lower in energy, at 1.835 eV, and may indicate that it is due to recombination occurring at the type-II interface between the $Zn_{1-x-y}Mg_xCd_ySe$ barrier layer and the $ZnSe_{0.53}Te_{0.47}$ cap. Although the band alignment between these two materials is not known, a type-II band alignment is expected.[9] In fact, strong luminescence has been previously observed from II-VI type-II heterstructures.[9] The elimination of the red

Reproduced with permission of the copyright owner. Further reproduction prohibited without permission.

emission and observation of QW EL after etching show that an optimum thickness for this layer must be used, thin enough to suppress the absorption of the QW emission but thick enough to insure good ohmic contact characteristics. Our experience suggests that 15-20 nm is appropriate.

Figure 4 shows the EL spectra of three LEDs with different QW thickness and/or composition. Three emission lines, one in the red (1.967 eV), one in the yellow (2.244 eV) and a third in the blue-green (2.385 eV) region of the visible range were observed from the three structures, demonstrating the feasibility of these devices for full-color display elements. A slightly thinner QW layer, with a higher subband energy level, would be needed to reach the blue emission. The EL line shapes are symmetric and have full-widths-at-half-maximum (FWHM) of 70-90 meV which are comparable to reported data from ZnSe-based QW LEDs (46-85 meV)[3-5] and significantly narrower than the typical widths from blue GaN-based LEDs (~200 meV).[6,7] The

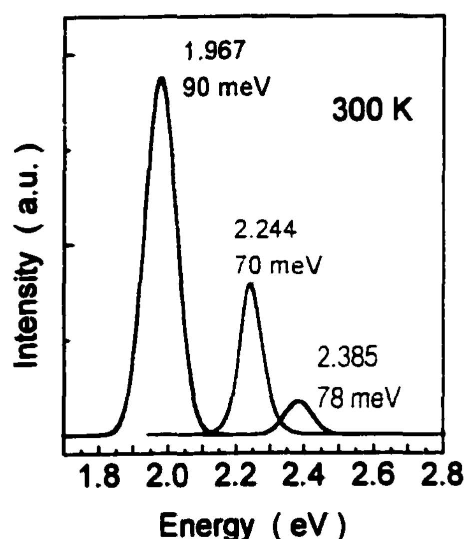

Figure 4 Surface electroluminescence (EL) spectra for three LED structures that differ only in the QW thickness and /or composition used. Emission throughout the visible range is observed.

Reproduced with permission of the copyright owner. Further reproduction prohibited without permission.

increase in EL intensity from the green to the red diode varies nearly proportionally with the QW thickness for each structure, suggesting that the quantum efficiencies for the three structures are comparable. The use of multiple QW's for the yellow, green or blue LED's, which are lattice matched, would compensate for this and adjust the brightness of the LEDs so that they are comparable.

For practical integrated full-color display elements, a method to fabricate the three structures on a single substrate (device integration) should be developed. An approach that may be used toward this goal is the use of shadow mask selective area epitaxy[10] as a means to pattern QW region, so that the different thickness and/or composition QWs can be deposited on a single substrate.

Reproduced with permission of the copyright owner. Further reproduction prohibited without permission.

Chapter 6

MBE Growth of II-VI Materials on Novel Hexagonal $Zn_xMg_{1-x}S_ySe_{1-y}$ Bulk Substrates

6-1 Introduction

Due to the unavailability of high quality II-VI bulk substrates, II-VI epitaxial structures for visible emitters are typically grown on III-V substrates, e.g. GaAs and InP. The main factor that limits laser lifetimes is the generation of defects at the II-VI/III-V interface due to heterovalent nucleation.[1] Thus, growth of wide bandgap II-VI devices on native (II-VI) bulk substrates is desirable. Native substrates have many advantages:

1) Chemical compatibility (probably the most important). The initial growth interface is isovalent, a better condition for bonding than the heterovalent condition of a foreign substrate. In addition, isovalency allows high temperature processing for contact formation, since

Reproduced with permission of the copyright owner. Further reproduction prohibited without permission.

problems caused by interdiffusion at the interface are minimized. This may be crucial for reducing contact resistance.

2) Band alignments are compatible leading to efficient carrier transport across the interfaces.

3) Thermal expansion coefficients are compatible, minimizing the presence of strain at the substrate/epilayer interface.

However, cubic wide bandgap II-VI bulk crystals tend to exhibit defects, such as twins. It has been observed that II-VI crystals with preferred hexagonal (wurtzite) structures, such as ZnS or CdS, can be grown without twins.[2] The hexagonal crystal structure offers a number of advantages over the more familiar cubic structure for semiconductor lasers:

1) It has been observed[2,3] that bulk hexagonal binary materials do not contain twins.

2) There are fewer easy glide planes in hexagonal structures, and thus dislocation motion (the leading mechanism of degradation) should be slower.

3) In this connection, the thermal expansion coefficients of hexagonal materials are generally lower than similar cubic ones;

Reproduced with permission of the copyright owner. Further reproduction prohibited without permission.

this is a sign of reduced anharmonicity in lattice vibration. Anharmonicity leads to easier atomic motion, which facilitates dislocation motion. Thus, a material system with lower anharmonicity should result in reduced degradation.

4) The long experience with electron beam pumped lasers[4] has also shown that hexagonal compounds, such as CdS and CdSe, have lower laser thresholds than cubic ones of similar bandgaps, such as ZnSe. This may be the result of the fact that the valence band degeneracy is lifted in hexagonal crystals. The splitting of the valence band is the same phenomenon that occurs in strained layer superlattices that are preferred for many laser applications, but, in this case, the strain is absent.

According to the advantages above, growth of hexagonal quantum well lasers of II-VI materials on a hexagonal native II-VI substrate, e.g. the quaternary $Zn_xMg_{1-x}S_ySe_{1-y}$[5], is expected to give a significant improvement in the life time and performance of laser diodes.

It has been observed in other systems that an epitaxial layer will tend to replicate the crystal structure of the bulk substrate, and thus it should be possible to grow a hexagonal layer of a normally cubic material on a

Reproduced with permission of the copyright owner. Further reproduction prohibited without permission.

hexagonal substrate. Since the bonding is tetrahedral in both phases, and the difference between the structures is not manifested until the third nearest neighbor, the hexagonal structure may be stabilized throughout the epitaxial layer. The enthalpy of the phase transition for ZnSe has been measured as 946 J/mol,[6] a rather small value (for comparison, the enthalpy of formation is 165 kJ/mol). Thus, it should be possible to make stable ZnSe in its hexagonal phase by epitaxial growth on a bulk hexagonal substrate.

Finally, it is desirable to have a substrate with a higher bandgap than the active layer of a diode laser, in order to avoid loss due to absorption by the substrate.[7] By adjusting the composition of the substrate (i.e. by formation of alloys) the bandgap of the native substrate can be tailored to meet these requirements. Furthermore, in alloys of hexagonal and cubic compounds, the crystal phase of the alloy is a function of composition.[8] Several recent studies of the ternary alloy $Zn_{1-x}Mg_xSe$ have shown a change from cubic to hexagonal structure as the Mg concentration is raised. Using high pressure Bridgman growth, the phase transition was found to be at 18.5%.[9] Using vapor growth, the transition was found between 10 and 20% Mg.[10] We have added sulfur to reduce the lattice constant to match ZnSe; this also promotes hexagonality. Thus, we believe that the phase transition is slightly below 12% Mg at a S concentration of 8%.

Reproduced with permission of the copyright owner. Further reproduction prohibited without permission.

The obvious method to raise the bandgap of ZnSe was through the addition of S, leading to the ternary ZnSSe. However, this reduces the lattice constant, thus inducing strain and misfit dislocations if it is used as an epitaxial substrate. Mg is usually thought to be smaller than Zn, because tables of ionic radii are derived from compounds, such as chlorides and the oxides, where Mg is in octahedral coordination. However, in tetrahedral coordination, it is larger than Zn, as shown to be the case for MgSe.[11] MgSe typically adopts a rocksalt structure with Mg and Se in octahedral sites; however, when it is deposited at low temperatures (77K), it takes the wurtzite structure, a hexagonal tetrahedral structure with both Mg and Se in tetrahedral coordination, and the one that is the main structure discussed in this paper. MgSe prepared at low temperatures retains its wurtzite structure when warmed to room temperature, where its lattice constants are usually determined. The addition of Mg raises the lattice constant, while the addition of S decreases it. Thus, they can be used to compensate each other, leading to a material of "constant" lattice constant. Since the lattice constants of MgSe, ZnSe and ZnS are known, the requisite lattice constant of any ZnMgSSe can be calculated. If Mg:S is 26:19, the lattice constant approaches that of ZnSe. In previous work, it has been found that the lattice constant of ZnSe could be matched to one part in 2800.[12] The use of bulk

Reproduced with permission of the copyright owner. Further reproduction prohibited without permission.

growth in this system thus allows the design of materials with lattice constants chosen on the basis of the desired design of the heterostructure. Engineering lattice constants, to suit novel heterostructures, "Substrate Bandgap Engineering", creates the potential for a new parameter in materials design.

We propose that as the composition varies, the structure (hexagonal or cubic) of quaternary $Zn_xMg_{1-x}S_ySe_{1-y}$ can also be varied as a function of Mg and S compositions.[5] In this chapter , we present initial work to demonstrate that hexagonal quaternary substrates of $Zn_xMg_{1-x}S_ySe_{1-y}$ can be grown having the desired bandgaps for visible emitter applications. These substrates may be desirable alternatives for epitaxial growth of II-VI blue laser structures. We show that $Zn_xMg_{1-x}S_ySe_{1-y}$ bulk crystals with 8%, 12%, and 16% Mg have been grown by the zone-melting technique. The S concentration is chosen by using the ratio 26:19, as explained above, in order to match the lattice constant of ZnSe. The 8% Mg crystal exhibits cubic symmetry, whereas the 12% and 16% Mg crystals are hexagonal. Hexagonal symmetry is demonstrated here by using optical birefringence, x-ray measurements and cross-sectional TEM measurements. The 12% Mg crystal is found to be defective (twinned) hexagonal while 16% Mg is pure hexagonal. These hexagonal 12% and 16% Mg crystals have good luminescence properties

Reproduced with permission of the copyright owner. Further reproduction prohibited without permission.

and appropriate bandgaps for blue-green laser applications as confirmed by photoluminescence (PL) and ellipsometry measurements. We also performed the MBE growth of ZnSe epilayers and ZnCdSe/ZnSe QW structures on the 12% Mg substrates. Epitaxial growth was achieved on both cleaved and cut and polished $(11\bar{2}0)$ surfaces. p-type doping of hexagonal ZnSe has also been performed using an rf discharge nitrogen source. TEM measurements indicate that the epitaxial layers are of hexagonal structure.

Reproduced with permission of the copyright owner. Further reproduction prohibited without permission.

6-2 Growth and characteristics of hexagonal $Zn_xMg_{1-x}S_ySe_{1-y}$ bulk substrates

Bulk ternary and quaternary alloys of binary compounds that have different preferred phases will assume one phase or the other depending on the composition. $Zn_xMg_{1-x}S_ySe_{1-y}$ bulk crystals with Mg composition of 8%, 12%, and 16% have been grown by the zone melting technique at Optical Semiconductors, Inc. This technique consists of lowering a graphite crucible containing the charge through an induction coil, that heats the molten zone to about 1600 °C at its peak temperature. A self-sealing and self-releasing technique is used, so that only a modest external pressure (1000 kPa) is needed to suppress volatilization.[14] The technique has been developed at Optical Semiconductors for the growth of high bandgap II-VI compounds, and uses specially designed crucibles. The specific procedure is an outgrowth of the method developed for the first growth of bulk zinc magnesium sulfoselenide. Zone melting is used because it has a short cycle time (1-2 days), and can make material of constant alloy mole fraction. Most importantly, this method has been proven to be capable of handling magnesium, a reactive element.

In this section, we determine the crystal symmetry and optical property of those bulk quaternary substrates using x-ray measurements,

Reproduced with permission of the copyright owner. Further reproduction prohibited without permission.

optical microscopy, transmission electron microscopy (TEM), and photoluminescence.

To confirm the crystal symmetry, a combination of x-ray powder diffraction (PXD) and optical interference microscopy has been performed. Powder species of the 12% and 16% Mg crystals were prepared for PXD measurement in order to determine their crystal symmetry and crystal lattice constants. Powder diffraction analysis of the crystals uses strong assumed $(10\bar{1}0)$ & $(00\bar{2}2)$ reflections to estabiish estimates for the hexagonal crystal lattice. The remaining reflection peaks from the hexagonal symmetry were then assigned. From PXD, we calculated lattice constant $a_0 = 4.013$ Å and a c_0/a_0 ratio of 1.634 for the 12% Mg material and $a_0 = 4.008$ Å and $c_0/a_0 = 1.640$ for the 16% Mg material assuming hexagonal symmetry. Their c_0/a_0 values are both very close to the ideal hexagonal value of 1.633. Although a few peaks could not be assigned, most of the peaks are consistent with a hexagonal structure. The presence of additional peaks may be a result of distortions introduced by grinding the substrates into powder or it could be due to small amounts of impurity phases in the crystal. The calculated hexagonal lattice constant a_0 is consistent with the cubic ZnSe lattice constant $[a_0^h = a_0^c/\sqrt{2}]$, which was anticipated based on the selected quaternary compositions.

Reproduced with permission of the copyright owner. Further reproduction prohibited without permission.

Optical determination was performed on selenide powders and wafers cut from our quaternary ingots. Since the cubic structure has no optic axis while the hexagonal structure is uniaxial, we have observed the phase transition, between cubic and hexagonal, of $Zn_xMg_{1-x}S_ySe_{1-y}$ quaternaries as a function of Mg composition by birefringence measurements. The 8% Mg crystal was easily identified as cubic based on its cleaving patterns. In the test of birefringence, cubic and hexagonal $Zn_xMg_{1-x}S_ySe_{1-y}$ samples were routinely distinguished in oil immersion mounts by the extinction of interference colors on the surface of the cubic crystal (i.e. the 8% Mg substrate). In contrast, hexagonal crystals are supposed to display an ordinary range of retardation colors, reflective of a random distribution of orientations in an oil mount. Moreover, twinned crystals showed clear linear striations at 400x along twin boundaries (as shown in Figure 1) in contrast to non-strained hexagonal crystals. The 16% Mg crystal shows isochrome surfaces for all crystallographic orientations, suggesting a hexagonal symmetry, while the 12% Mg crystal shows multiple color bands on the surface as shown in Figure 1. Figure 1 shows the image of birefringence test of the 12% Mg substrate. The multiple retardation color bands indicate that the 12% Mg substrate has hexagonal symmetry containing high density of twins.

Reproduced with permission of the copyright owner. Further reproduction prohibited without permission.

In a more sensitive test (uniaxiality test), crystal symmetry of the $Zn_xMg_{1-x}S_ySe_{1-y}$ substrate was confirmed through optical interference examination of a polished 0.2 mm thick by 0.25 cm^2 (0001) section. The 16% Mg substrate was additionally studied by preparing doubly polished wafers cut parallel to the (0001) basal section for the uniaxiality test. The setup diagram of this test is shown in Figure 2. Using interference microscopic methods (conoscopic method), plane-polarized light is focussed onto the center of wafers using a substage condensing lens. The resultant cones of light emerging from the top surface of the wafers are then resolved using a hyper-stage polarizer and Bertrand Lens (or pinhole) assembly to bring the image

Figure 1 Image of birefringence test of the 12% Mg substrate. The multi-color bands represents the boundaries of twins suggesting that the substrate is a highly twinned hexagonal.

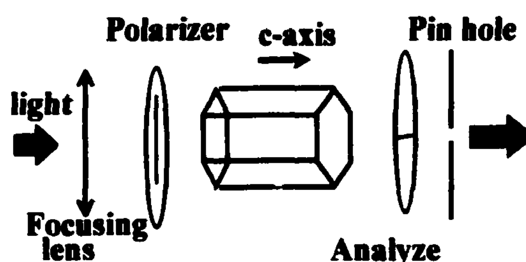

Figure 2 Schematic setup diagram of uniaxiality test.

Reproduced with permission of the copyright owner. Further reproduction prohibited without permission.

Figure 3 Interference figure of uniaxiality of the 16% Mg crystal. The directions of the isogyre cross are those of the polarizer and analyzer. This interference demonstrates that the 16% Mg crystal is pure hexagonal.

to the plane of the microscope oculars. The latter creates an image comprised of concentric circles of equal retardation where cones are imaged onto the image plane. Figure 3 shows the image of the uniaxiality test of the 16% Mg substrate. The magnitude of the retardation increases from a null value at the center of the image, where light has followed the trace of the optic axis, to a maximal value, where light toward the outside of incident cones intersects the optic axis at a significant angle. The retardation thus increases radically in this view creating the set of retardation rings. The isochrome color itself is created as a result of the constructive interference between the emergent ordinary and extraordinary light paths where vibration within the crystal is at ninety degrees. The reconstructed beam is rotated

Reproduced with permission of the copyright owner. Further reproduction prohibited without permission.

from the original direction by an increasing amount as the angle with the optic axis increases. The angle of the recombined beam relative to the analyzer (upper polarizer) controls the isochrome color. The presence of only one set of concentric circles demonstrates the uniaxial character of the wafer.[15] Figure 3 is caused by the orthonormal vibration directions of the extraordinary and the ordinary light beams relative to individual cones. The ordinary light vibrates tangent to emergent cones whereas the extraordinary light vibrates in a direction perpendicular to the cones. Therefore, there is always one band of emergent light with a vibration direction parallel to the substage polarizer that creates a null or extinction band. The set at ninety degrees creates a second extinction set normal to the first, the isogyre cross characteristic of uniaxial crystals. These two features, the concentric set of isochromes and the isogyre cross are restricted to the hexagonal and tetragonal systems.

The optical interference tests above indicate that while both substrates have hexagonal symmetry, the presence of multiple color bands in the 12% Mg crystal suggests that it may be twinned. The 16% Mg crystal gives an ideal interference figure including the isogyre cross and isochrome circles, demonstrating that not only is the 16% Mg crystal relatively perfect hexagonal material but also the (0001) surface of the sample studied was

Reproduced with permission of the copyright owner. Further reproduction prohibited without permission.

well prepared. When combined with the x-ray diffraction evidence, these results provide unequivocal demonstration of hexagonal symmetry in $Zn_xMg_{1-x}S_ySe_{1-y}$ substrate wafers with Mg contents higher than 12%.

TEM cross-section specimens were prepared by mechanically thinning the samples using a tripod polisher to ~30 μm followed by argon ion milling at room temperature. The energy of the argon ions was 3 keV and the current 1mA to minimize sample preparation damage. A JEOL 4000FX-II operated at 300 kV was used to study the substrate-epilayer structure.

Figure 4(a) shows a cross-sectional TEM image of the 16% Mg ZnMgSSe crystal. The sample was thinned until perforation occurred at the center. The lines are bent contours, evidence of crystalline material. The image clearly shows a very large single crystalline material with hexagonal-close-packed (HCP) structure and no stacking faults or twins. This HCP structure is confirmed by the diffraction pattern, shown in Figure 4(b). In contrast, Figure 5 is a cross-sectional TEM image from the 12% Mg ZnMgSSe crystal with an MBE grown hexagonal ZnSe epilayer on it. (The MBE grown ZnSe will be discussed in the next section in detail.) Although a hexagonal structure was observed from the diffraction patterns from this

Reproduced with permission of the copyright owner. Further reproduction prohibited without permission.

Figure 4 (a) Cross sectional TEM image of a ZnMgSSe crystal with 16% Mg.

Reproduced with permission of the copyright owner. Further reproduction prohibited without permission.

Figure 4 (b) A (0001) diffraction pattern from this sample.

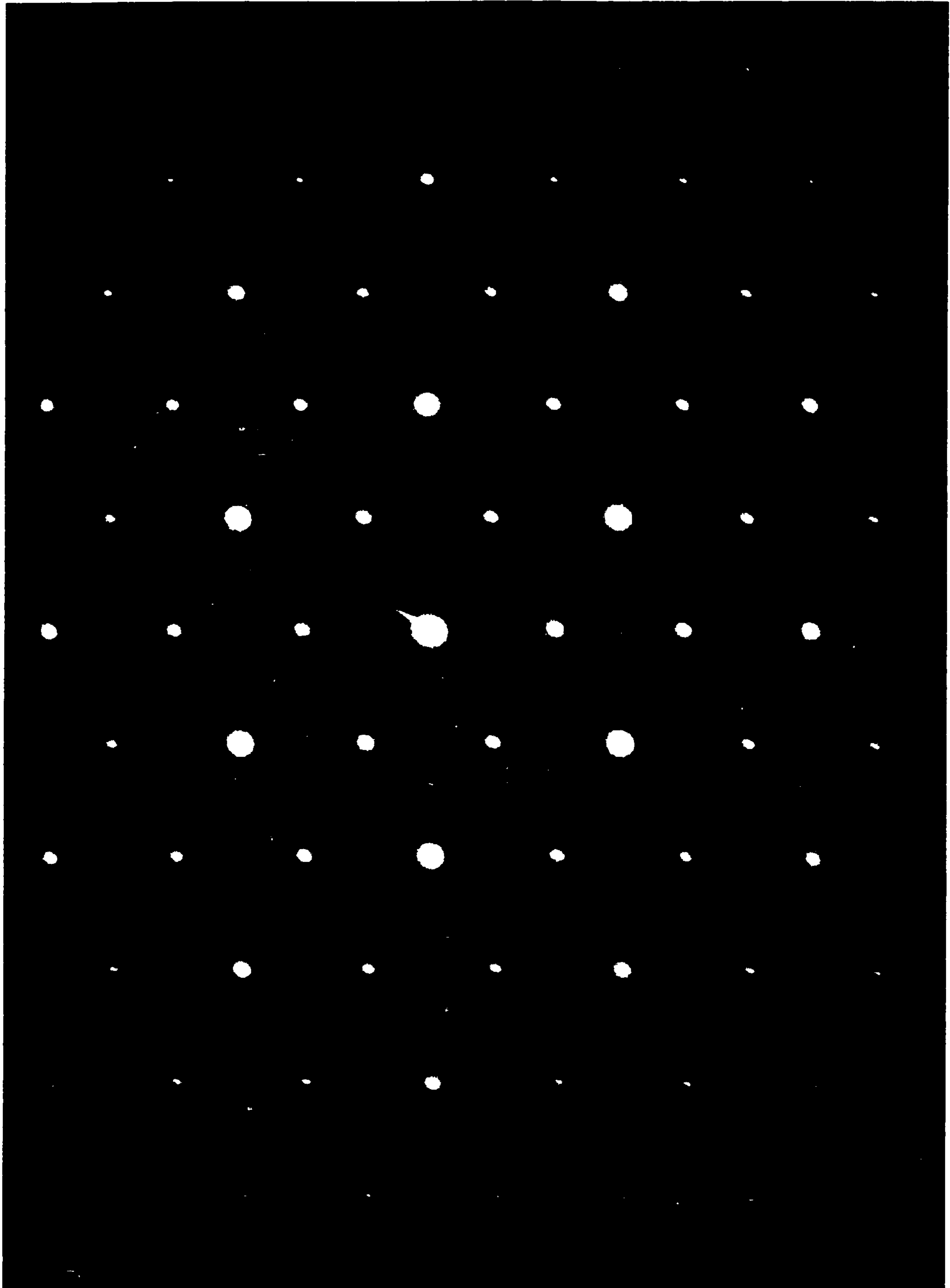

Reproduced with permission of the copyright owner. Further reproduction prohibited without permission.

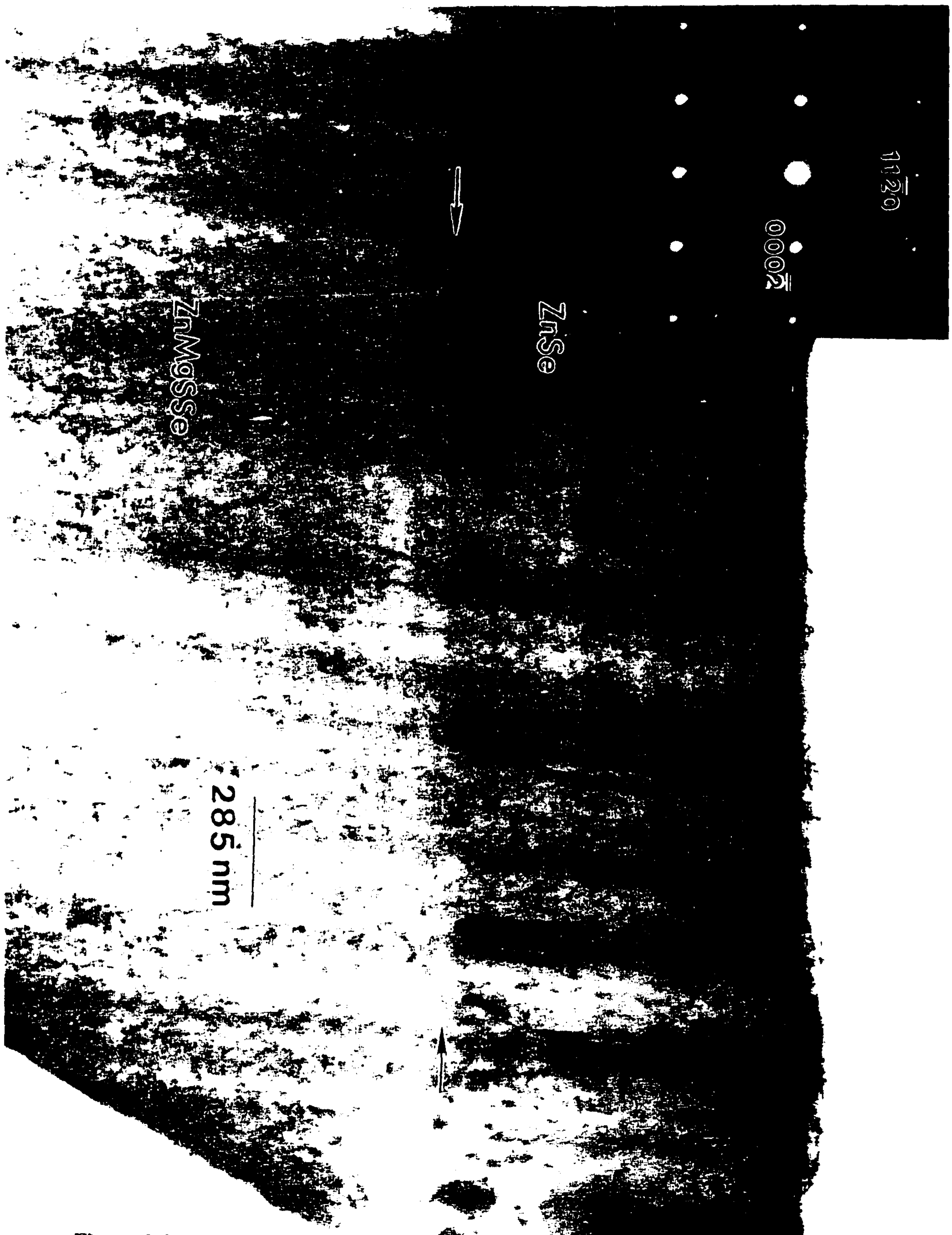

Figure 5 Cross sectional TEM image of a ZnCdSe/ZnSe QW structure grown on a ZnMgSSe substrate with 12% Mg content. The inset shows the (1010) diffraction pattern of this sample.

Reproduced with permission of the copyright owner. Further reproduction prohibited without permission.

sample (inset), the image in Figure 5 gives evidence for a high density of stacking faults. We propose that the high density of defects in the 12% Mg crystal occurs because of its close proximity to the cubic-hexagonal phase boundary.

It is known that the stacking order of a crystal with HCP symmetry is ABABAB.... along the c-axis while in cubic close packing is ABCABCABC... along the corresponding [111] direction. The differences among A, B, and C planes involve simply a translation of atomic planes to equivalent sites along directions perpendicular to the c-axis for the HCP and the [111] direction for the cubic structures. For example, a twinned cubic crystal could have a faulted stacking order of ABCABC$\underline{B}$CBACBA... where the underlined B plane is a mirror plane in the stacking sequence corresponding to a twin boundary. This stacking sequence can also be viewed as ....ccchhccc..., where c corresponds to cubic stacking and h to hexagonal stacking sequence. We believe that the faulted hexagonal structure observed in Figure 5 corresponds to changes in the stacking sequence of the form ABABA$\underline{C}$ACAC$\underline{B}$CBC... which can also be seen as hhhchhhhhchhh.... Based on this analysis it is not surprising to have a highly faulted hexagonal crystal when the crystal phase is at the transition of

Reproduced with permission of the copyright owner. Further reproduction prohibited without permission.

the stacking order from ABCABC...(cubic) to ABABAB...(hexagonal). We call this phenomenon "phase indecision".[16,17]

Measurement of the PL at 77K pumped by a He-Cd laser with a wavelength of 325 nm was performed to characterize the optical properties of the hexagonal crystals. To identify the observed luminescence peaks, temperature-dependent PL measurements of the 12% Mg crystal from 77K to 300K have been performed. Spectral ellipsometry measurements were used to confirm the bandgap emission of the substrate at 300K. Figure 6(a) shows the 77K PL spectra of the 12% and 16% Mg crystals. There are two peaks observed for each substrate at 77K, a small high energy peak and a dominant peak

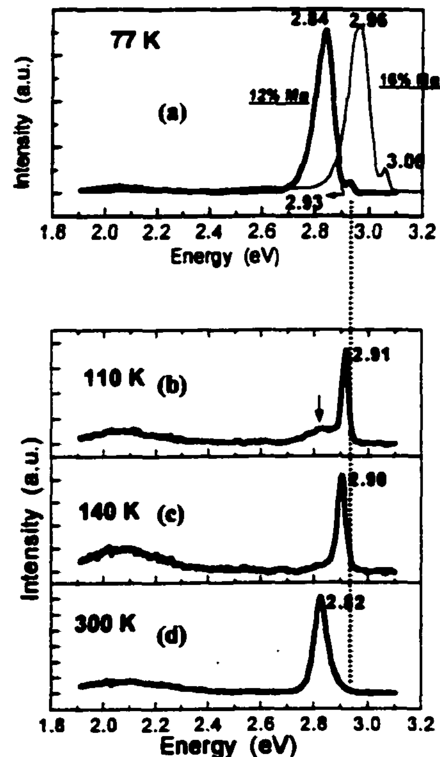

Figure 6(a) Photoluminescence at 77K of the 12% and 16% Mg crystals. The emissions at 2.93 eV and 3.06 eV are the near bandgap emissions for the 12% Mg crystal and the 16% Mg crystals, respectively. Spectra (a)-(d) show the temperature-dependent PL of the 12% Mg crystal. The assignment of the bandgap emission at 2.82 eV for the 12% Mg crystal at 300K has been confirmed by ellipsometry measurements.

Reproduced with permission of the copyright owner. Further reproduction prohibited without permission.

about 90 meV below it. To identify those peaks, temperature-dependent PL measurements were performed. Figure 6(a)-(d) presents the temperature-dependent PL spectra of the 12% Mg crystal from 77K to 300K with a constant excitation intensity. As the temperature increases, the dominant peak at 77K is dramatically reduced while the small peak at 2.93 eV shifts to 2.82 eV and becomes dominant. Spectral ellipsometry measurement at 300K indicates that the bandgap for this crystal is at 2.82 eV. Thus, we can assign the higher energy peak to the bandgap emission, while the lower energy transition may be related to a donor-to-acceptor-pair (DAP) transition. As shown in Figure 6(a), the 16% Mg crystal has a slightly higher 77K near bandgap emission of 3.06 eV. This is consistent with the higher Mg and S compositions which should increase the bandgap of $Zn_xMg_{1-x}S_ySe_{1-y}$. Both alloys, the 12% and 16% Mg, have potential use as blue light laser materials due to their high bandgap energy which will eliminate losses in the devices due to self absorption in the substrates.[7]

The characterization results above show that the $Zn_xMg_{1-x}S_ySe_{1-y}$ bulk substrates with 12% or 16% Mg have hexagonal symmetry and appropriate bandgap for the application to hexagonal blue green light emitting devices. The epitaxial growth of ZnSe single layer and ZnCdSe/ZnSe quantum well

Reproduced with permission of the copyright owner. Further reproduction prohibited without permission.

structure on those hexagonal substrates, including the 12% and 16% Mg substrates, using MBE technique will be addressed in the following section. Finally, nitrogen doping of the epitaxially grown hexagonal ZnSe, using an rf discharge nitrogen plasma source, has been performed by MBE and will be addressed below.

Reproduced with permission of the copyright owner. Further reproduction prohibited without permission.

6-3 MBE growth of hexagonal ZnSe epilayers and ZnCdSe/ZnSe QW structure on hexagonal $Zn_xMg_{1-x}S_ySe_{1-y}$ bulk substrates

Substrates for MBE growth were prepared by cleaving or by cutting and polishing. The (1120) plane, which is a good cleavage plane produced shiny cleaved surfaces with small steps visible under Nomarski interference contrast microscope illumination. Substrates were also prepared by sawing and chemomechanically polishing with bromine-methanol solution. In both cases, the (1120) surface orientation was confirmed by a single crystal x-ray θ-2θ scan. Figure 7 shows the single crystal x-ray diffraction spectrum of a 12% Mg (1120) prepared substrate. Two pairs of strong and narrow $K_{\alpha 1}$-$K_{\alpha 2}$ peaks at about 45.3° and 100.5° present the 1st and 2nd order diffraction from the (1120) plane which confirms the orientation of the substrate and the lattice constant obtained by PXD

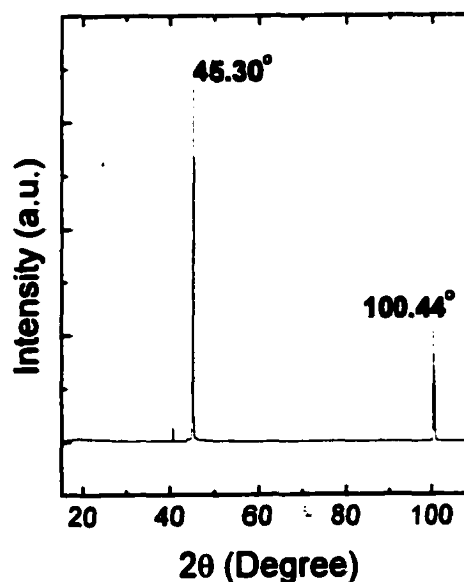

Figure 7 Single crystal x-ray diffraction spectrum (θ-2θ scan) of the 12% Mg crystal.

Reproduced with permission of the copyright owner. Further reproduction prohibited without permission.

measurement.

The 12% and 16% Mg substrates with the $(11\bar{2}0)$ surface orientation were used for MBE growth. The optimum epitaxial growth results were obtained on substrates that were degreased and etched ex-situ by a solution of 1% bromine in methanol. This produced a dark red residue on the surface, possibly a Se residue, that could be removed by boiling in trichlorethylene (TCE) which left a bright yellow and mirror-like surface. After introduction into the ultra high vacuum chamber, the substrate was kept at 300°C and then heated gradually to 510°C under a Se flux. Reflection high energy electron diffraction (RHEED) patterns of the substrates at 300°C were spotty. When the temperature was increased to 450°C - 510°C, the RHEED patterns had an increase in brightness and the reflection spots became elongated. It was assumed that the oxide layer was removed at these temperatures. The substrate was then kept at 510°C for 20 min to ensure complete oxide removal. No additional steps were needed to remove the oxide layer and produce a highly ordered crystalline substrate.

ZnSe epitaxial layers were grown on the 12% and 16% Mg $(11\bar{2}0)$ substrates using nominal growth rates of 1/3 and 1 μm/hr, estimated on the basis of the growth of ZnSe on (001) GaAs. The growth temperature was 300°C, and the beam equivalent pressure (BEP) ratio of Se to Zn was about

Reproduced with permission of the copyright owner. Further reproduction prohibited without permission.

4. Under both conditions the RHEED pattern became streaky as the growth proceeded, suggesting that the growth was 2-dimensional. The TEM result of the epitaxial layers with the growth rate of 1/3 mm/hr (see Figure 5 in Section 6-2) show that the epitaxial layer duplicates the structure of the substrate, that is, in this case, the layer exhibits a faulted hexagonal crystal structure, very similar to that of the substrate. Thus, we conclude that hexagonal ZnSe-based epitaxial layers and structures were obtained on these

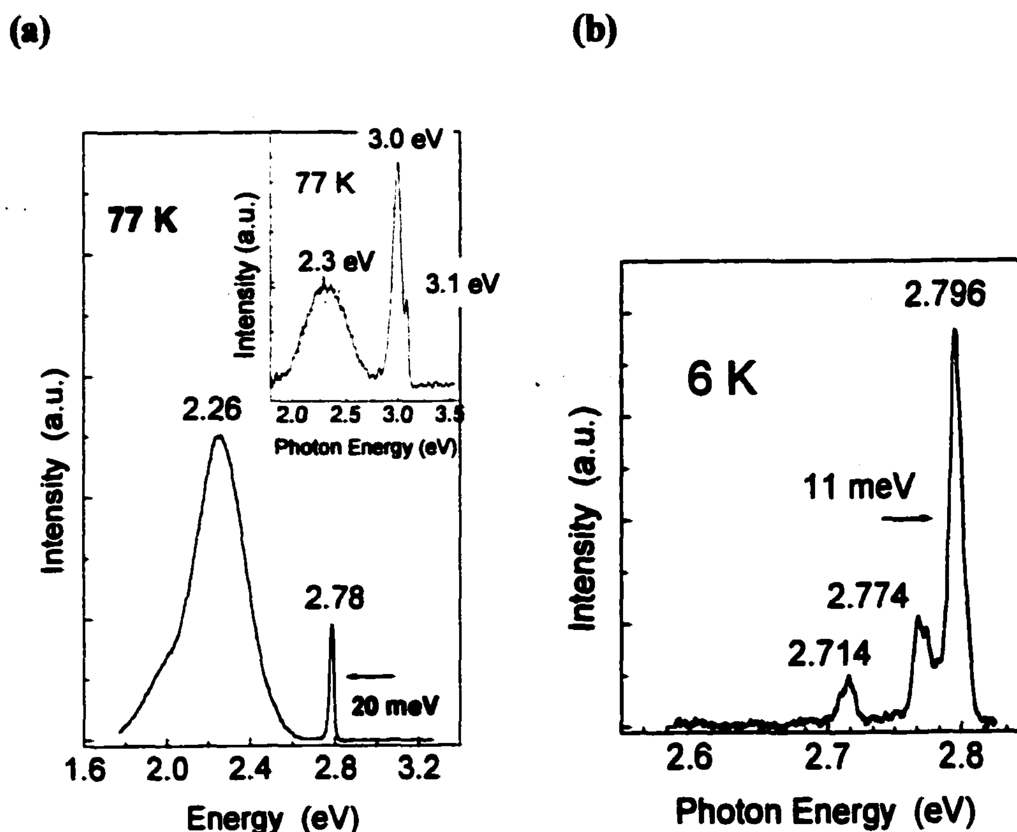

Figure 8(a) 77K PL spectrum of hexagonal ZnSe on a hexagonal ZnMgSSe substrate. The inset on (a) represents a 77K PL spectrum of a substrate that has similar deep level emission at around 2.3 eV. **(b)** 6K PL spectrum of the sample on (a). The spectrum shows no defect-related Y-line emission at around 2.60 eV.

Reproduced with permission of the copyright owner. Further reproduction prohibited without permission.

novel substrates.

Figure 8(a) shows 77K PL spectra of a hexagonal ZnSe single layer grown on a 12% Mg substrate with the slow growth rate. The spectrum shows a near bandgap emission at 2.78 eV and an efficient deep level emission at 2.3 eV. In fact, a similar deep level emission was observed in some of these substrates as shown in the inset. This suggests that the broad band in the ZnSe layers may originate from the substrate. For example, impurities in the substrate such as Cu, unintentionally incorporated during the bulk growth of the substrates, can easily diffuse into the ZnSe epilayer during the epitaxial growth.[26] It has been observed that only a small amount of Cu impurities can cause effective deep level emissions such as Cu-green and Cu-red emissions in ZnSe materials.[25] Further measurements such as secondary ion mass spectroscopy (SIMS) could be performed to detect the Cu incorporation. Figure 8(b) shows the 6K PL spectrum in the region around the near bandgap emission. The peaks at 2.796, 2.774, and 2.714 eV may be due to impurity-related transitions. More PL studies are needed to identify these peaks more precisely. No Y-line (an interface defect-related emission) was observed at 2.6 eV. The absence of the Y-line suggests that good substrate preparation and growth conditions have been achieved. In terms of the PL properties, there is no significant difference between the use

Reproduced with permission of the copyright owner. Further reproduction prohibited without permission.

of the 12% and 16% Mg substrates and between the fast and slow growth rates.

ZnCdSe/ZnSe quantum well (QW) structures were also grown using both growth rates. First, a nominally 1.5 μm thick ZnSe epilayer was grown on the substrate followed by the well layer of 10 nm $Zn_{0.7}Cd_{0.3}Se$. A cladding layer of 100 nm of ZnSe was then deposited over the QW. Figure 9 shows the 77K PL spectrum of a QW structure grown on a 12% Mg substrate. At 77K a very efficient emission at 2.44 eV, consistent with the expected bandgap energy of the QW layer, was observed. Interestingly, the broad deep level emission observed in single ZnSe layer was suppressed in the QW structure.

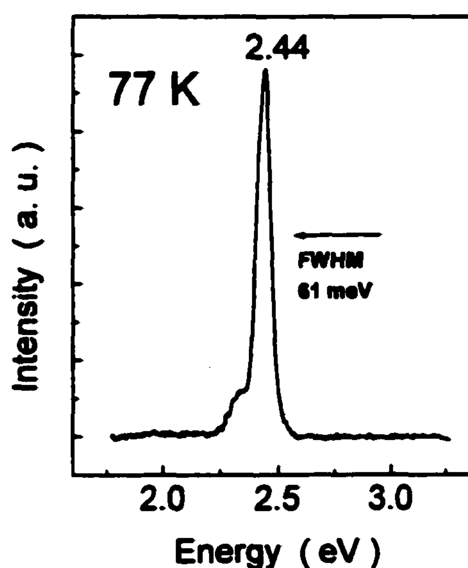

Figure 9 77K PL spectrum of the $Zn_{0.7}Cd_{0.3}Se$/ZnSe QW structure.

There is no significant difference in the PL properties observed between the QW samples using fast and slow growth rates or by using the 12% and 16% Mg substrates. Figure 10 shows the double crystal x-ray rocking curve from the (11$\bar{2}$0) plane of the QW structure. The asymmetric peak suggests two

Reproduced with permission of the copyright owner. Further reproduction prohibited without permission.

nearly matched overlapping peaks (dotted): one from the substrate and another from the epilayers. This supports the near lattice matching between the ZnSe epitaxial layer and the 12% Mg substrate. The strong x-ray signal suggests a good crystalline quality of this QW structure.

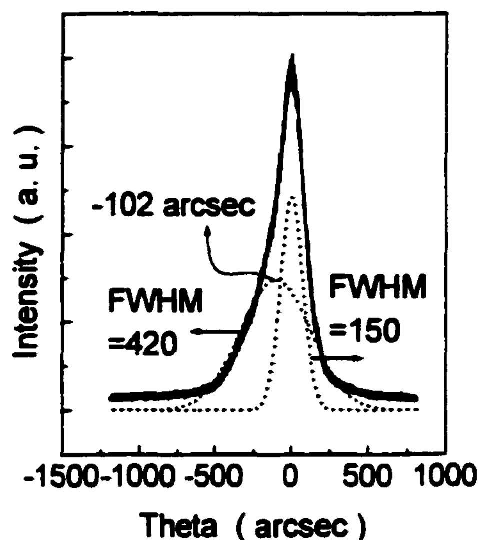

Figure 10 Double crystal x-ray rocking curve from the (11$\bar{2}$0) plane for a ZnCdSe/ZnSe QW structure grown on the 12% Mg quaternary substrate.

We conclude that good substrate preparations and growth conditions have been developed for MBE growths on these novel hexagonal $Zn_xMg_{1-x}S_ySe_{1-y}$ substrates. By using these conditions, hexagonal ZnSe-based epitaxial layers and QW structures have been successfully grown on these substrates, suggesting that hexagonal II-VI device structures can be grown on these novel hexagonal substrates. In the next section, the p-type doping of hexagonal ZnSe using an rf- discharge nitrogen plasma source will be addressed.

Reproduced with permission of the copyright owner. Further reproduction prohibited without permission.

6-4 p-type doping of hexagonal ZnSe using an rf discharge nitrogen plasma source

Hexagonal (wurtzite) II-VI compounds, such as CdS, CdSe, and ZnS, occur naturally as n-type semiconductors and have difficulties in achieving p-type doping.[18] As in the zinc-blende (cubic) system, the most widely accepted explanation for this difficulty is the "self-compensation" of the shallow acceptors by various naturally occurring or spontaneously created donor defects such as vacancies and interstitials as discussed in Chapter 6. It has been theoretically suggested that nitrogen substituting anion sites may produce shallow p-type dopants in these hexagonal II-VI materials.[18] In fact, based on our knowledge and background, the p-type doping of hexagonal ZnSe (h-ZnSe) by MBE has never been reported while that of cubic ZnSe (c-ZnSe) has been significant successful by using atomic nitrogen sources. In this section, the p-type doping of h-ZnSe using an rf discharge nitrogen source will be addressed.

Three different nitrogen doping conditions were used in this study. All samples were grown using a growth rate of about 0.8 μm/hr. The first source condition, which used the optimum rf power of 400 W, can typically produce a net acceptor (N_A-N_D) level of 7 x 10^{17} cm^{-3} in (001) c-ZnSe while the second (300 W) and the third (200 W) give levels of 8 x 10^{16} cm^{-3} and low

Reproduced with permission of the copyright owner. Further reproduction prohibited without permission.

10^{16} cm^{-3} (estimated), respectively. In terms of the PL properties of c-ZnSe:N, the 400 W nitrogen source condition introduced a dominant deep donor-acceptor-pair (D^dAP) emission at about 2.686 eV and its well-resolved LO phonon replicas in the low-temperature (7 K) PL spectra while the 300 W and the 200 W conditions produced only shallow donor-acceptor-pair (D^sAP) emissions (at about 2.70 eV) and their LO phonon replicas (as discussed in Section 3-4). The nitrogen doping of these c-ZnSe samples were typically performed on the (001) surface and the details have been described in Section 3-4.

For the case of h-ZnSe:N, the nitrogen doping was performed on the non-polar $(11\bar{2}0)$ plane of h-ZnSe. Electrical characterization of these h-ZnSe:N samples, such as C-V profiling and Hall effect measurement, is not possible at present for determination of the carrier concentration because the substrates are resistive and no ohmic contact can be obtained on these epilayers. Therefore, PL measurements such as time-resolved, temperature-dependent and excitation intensity-dependent PL were used for the investigation of nitrogen incorporation in these h-ZnSe:N samples based on the well-known optical properties of c-ZnSe:N. The PL measurements were performed using the 325 nm line of a He-Cd laser.

Reproduced with permission of the copyright owner. Further reproduction prohibited without permission.

Figure 11 shows the 7 K PL spectra of the samples grown with three different nitrogen conditions [400 W (solid), 300 W (dashed), and 200 W (dotted)]. The spectra were taken under the same laser excitation intensity (3 x 10^{-4} I_0; where I_0 is the maximum excitation intensity that the laser can produce, ~10 mW after chopping.). Three broad bands peaking at around 2.70 eV were observed. According to the time-resolved PL data, these broad peaks are related to donor-to-acceptor-pair (DAP) transitions.[27] This demonstrates that nitrogen has introduced acceptor levels in this hexagonal ZnSe. However, the peak position exhibits a red shift from 2.70 eV to 2.65 eV as the rf discharge power increases from 200 W to 400 W corresponding to an increased nitrogen incorporation. Similar red shifts with increase of nitrogen incorporation have also been observed in heavily nitrogen doped (or highly compensated) c-ZnSe samples by many groups.[19,20,21] Kothandaraman et al[19] and Baume et al[20] identified these emissions as D^dAP-like transitions and

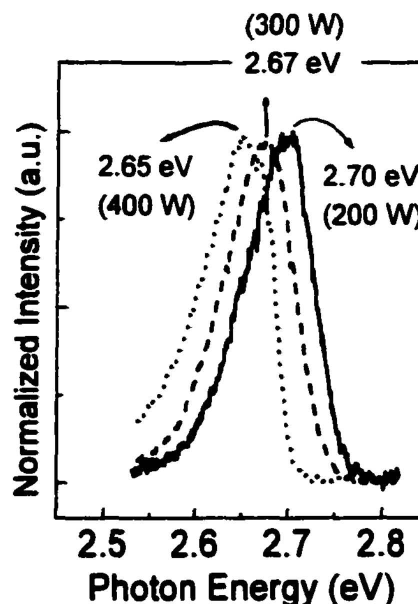

Figure 11 7K PL spectra of h-ZnSe:N with rf power of 400 W (solid), 300 W (dashed), and 200 W (dotted). The excitation intensity of all samples is 3 x 10^{-4} I_0.

Reproduced with permission of the copyright owner. Further reproduction prohibited without permission.

attributed the broadening and red-shifting of these D^dAP peaks due to Coulomb-potential fluctuations which were caused by a random distribution of ionized impurities in highly compensated (or heavily doped) crystals. Potential fluctuations lead to spatially separated potential wells in both the bands and the impurity energy states as shown in Figure 12.[19,20] Thus, D^dAP transitions from lowest donors into highest acceptors result in lower recombination energies, as indicated in Figure 12, compared to the DAP transition in the absence of fluctuations. Thus the red shift in the DAP emission as the nitrogen incorporation increases suggests that these h-ZnSe:N samples are heavily doped with nitrogen.

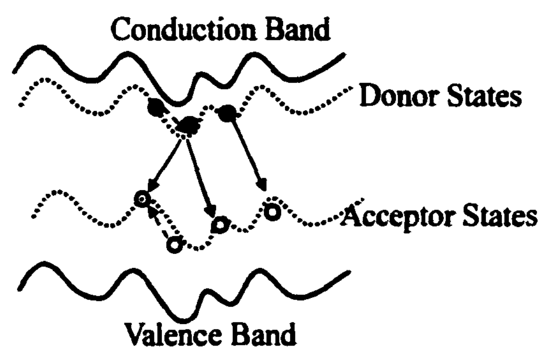

Figure 12 schematic diagram of the perturbed bands and impurity levels. The solid arrows represent the carrier recombination from the lowest electron states to the highest hole states in the impurity levels, thus reducing the energy of transition (the red shift).

For further investigation of these peaks, excitation intensity-dependent PL measurements were performed on these samples. Figure 13 (a) shows the PL spectra of the 400 W spectrum taken at various excitation intensities from 3 x 10^{-4} I_0 to I_0. At the lowest excitation, a broad and structureless band peaking at 2.65 eV was observed. As the excitation intensity is

Reproduced with permission of the copyright owner. Further reproduction prohibited without permission.

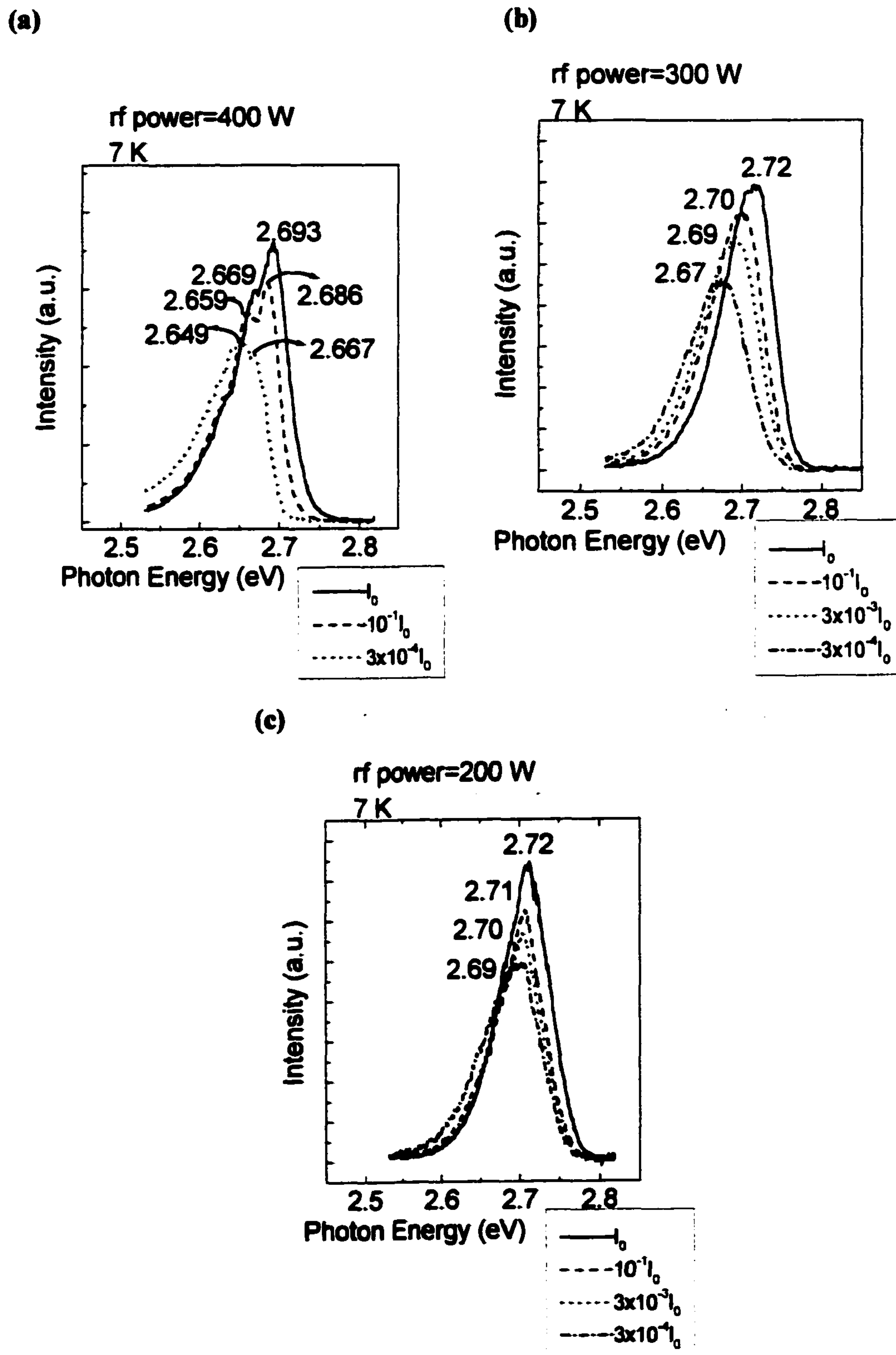

Figure 13 Excitation-dependent PL spectra of the h-ZnSe:N samples with rf powers of 400 W (a), 300 W (b), and 200 W (c). All of the samples show strong blue shifts as the excitation intensity increases.

Reproduced with permission of the copyright owner. Further reproduction prohibited without permission.

increased, a shoulder on the high energy side of the broad band is dramatically growing. At the maximum intensity I_0, the shoulder becomes dominant at 2.693 eV. A similar excitation-dependent behavior, exhibiting competition between two broad peaks, was observed in a highly doped c-ZnSe:N.[21] In that sample the incorporated nitrogen concentration [N] was 1.5×10^{19} cm^{-3} determined by secondary ion mass spectroscopy (SIMS) analysis.[21] Figure 13(b) & (c) represent the PL spectra of the 300 W and 200 W samples as a function of excitation intensity. The 300 W spectrum exhibits about 40 meV blue shift while the 200 W spectrum has a smaller blue shift of 13 meV. Both peaks shift to about the same position (~2.72 eV) at the maximum excitation intensity of I_0. Similar behavior was also observed in heavily doped (or highly compensated) c-ZnSe:N. It has been proposed that the blue shift due to the increase of excitation intensity results from a carrier screening effect of the potential fluctuation. The screening effect becomes more effective as more carriers are photo-generated by optical excitation. Thus, these broad bands were shifted towards a typical D^dAP position as the potential fluctuation effect was reduced by the carrier screening. The position, where both broad bands meet at the maximum excitation intensity I_0, may be close to the typical D^dAP position of h-ZnSe:N. For further identification, temperature-dependent PL measurements

Reproduced with permission of the copyright owner. Further reproduction prohibited without permission.

of the 300 W sample with the maximum excitation intensity I_0 were performed. A slight blue shift (a normal D^dAP behavior) rather than a red shift (a perturbed D^dAP behavior with potential fluctuation) with the increase of sample temperature from 7 K to 30 K was observed.[20] This suggests that these peaks behave more like an unperturbed D^dAP at the maximum excitation I_0 which is consistent with the model of the screening effect. It should be noted that the D^dAP position in h-ZnSe:N (~2.72 eV) is higher than that in c-ZnSe:N (~2.686 eV). The difference, in fact, is consistent with the expected value (~35 meV) of the difference between bandgap energies of h-ZnSe and c-ZnSe. Other optical characteristics such as photoluminescence excitation (PLE) may be used for the measurement of the bandgap energy of h-ZnSe.

The above investigation of PL properties suggests that these h-ZnSe:N samples were excessively-doped (and highly compensated) with nitrogen. The nitrogen conditions used (rf power of 400, 300, and 200 W) produced reasonable nitrogen incorporation exhibiting normal DAP emissions in (001) c-ZnSe:N while they caused potential fluctuation in $(11\bar{2}0)$ h-ZnSe:N. A stronger compensation phenomena observed in h-ZnSe:N under the same nitrogen source conditions may be caused by 1) a higher efficiency of nitrogen incorporation, and/or 2) an easier formation of compensation

Reproduced with permission of the copyright owner. Further reproduction prohibited without permission.

defects during the incorporation of nitrogen. It has been reported by many groups that growing and doping on different surface orientations or crystallographic planes exhibit different efficiencies of dopant incorporation and different possibility of defect formation.[22,23,24] Ohno et al[22] has systematically shown that the nitrogen incorporation in cubic ZnSe is different on different doping surface orientations. For example, the nitrogen incorporation efficiency on (n11) planes (n = integral) can be several times higher than on the (001) plane. On the other hand, Wang et al[23] and others[24] have shown that some dopants such as Si are amphoteric (n-type or p-type) in GaAs, depending on the orientation of doping surface. Thus, the $(11\bar{2}0)$ plane (a non-polar plane) of hexagonal ZnSe, corresponding to the (011) plane of cubic ZnSe, may have higher efficiency of nitrogen incorporation than the (001) plane of c-ZnSe. If too high nitrogen incorporation efficiency is the case in these samples, then the optimum nitrogen source conditions must yet be established for reasonable nitrogen incorporation. On the other hand, if the $(11\bar{2}0)$ plane easily generates compensation centers, then other surface orientations such as the $(10\bar{1}0)$ plane (a cleavage plane) and the (0001) plane (the basal plane) should be explored.

By the above studies, we have confirmed that hexagonal II-VI device structures can be grown on these novel II-VI hexagonal substrates by

Reproduced with permission of the copyright owner. Further reproduction prohibited without permission.

molecular beam epitaxy. For the p-type doping, the PL studies suggest that nitrogen has been incorporated and has introduced acceptor levels in these hexagonal ZnSe epitaxial layers. Evidence from these PL studies also suggests that these samples may be over-doped with nitrogen. For a more reasonable nitrogen incorporation, we have proposed several approaches such as further optimizing the nitrogen doping conditions and/or using different growth planes in order to achieve p-type conductivity in hexagonal ZnSe.

Reproduced with permission of the copyright owner. Further reproduction prohibited without permission.

Publications

Journal Papers

- **Red-green-blue Photo Pumped Lasing from ZnCdMgSe/ZnCdSe Quantum Well Laser Structures Grown on InP**, L. Zeng, B. X. Yang, A. Cavus, W. Lin, Y. Y. Luo, M. C. Tamargo, Y. Guo, and Y. C. Chen, Appl. Phys. Lett., **72**, 3136 (1998). *(Newsbreak paper selected by Laser Focus World)*

- **N-type Doping of Lattice-matched ZnCdSe and $Zn_xCd_yMg_{1-x-y}Se$ Epilayers on InP using $ZnCl_2$**, W. Lin, A. Cavus, L. Zeng, and M. C. Tamargo, J. Appl. Phys. **84**, 1472 (1998)

- **New Materials for Wide Bandgap II-VI Visible Emitters,** (invited paper) M. C. Tamargo, L. Zeng, W. Lin, and Y. Y. Luo, Proc. of the 2nd Intern. Symp. on Blue Lasers and Light Emitting Diodes, Chiba, Japan (1998)

- **Defect Reduction of $Zn_xCd_yMg_{1-x-y}Se$ Based Structures Grown on InP by Using Zn Irradiation of the III-V Surface,** L. Zeng, S. P. Guo, Y. Y. Luo, W. Lin, M. C. Tamargo, H. Xing, and G. S. Cargill III, J.

Reproduced with permission of the copyright owner. Further reproduction prohibited without permission.

Vac. Sci. Technol. **B 17**, 1255 (1999)

- **Molecular Beam Epitaxy Growth and Nitrogen Doping of $ZnSe_{1-x}Te_x$ Alloys on InP Substrates,** W. Lin, B. X. Yang, S. P. Guo, A. Elmoumni, F. Fernandez, and M. C. Tamargo, Appl. Phys. Lett. **75**, 2608 (1999)
- **Full-color Emitting Diodes from ZnCdMgSe/ZnCdSe Quantum Well Structures Grown on InP Substrates,** (invited paper) M. C. Tamargo, W. Lin, S. P. Guo, Y. Y. Luo, Y. Guo, and Y. C. Chen, accepted for publication, J. Cryst. Growth (1999)
- **High Crystalline Quality ZnBeSe Grown by Molecular Beam Epitaxy with Be-Zn Co-irradiation,** S. P. Guo, Y. Y. Luo, W. Lin, O. Maksimov, M. C. Tamargo, I. Kuskovsky, C. Tian, and G. F. Neumark, accepted for publication, J. Cryst. Growth (1999)
- **Growth and Characterization of Hexagonal (Zn,Mg)(S,Se) Bulk Substrates,** W. Lin, J. Steiner, M. C. Tamargo, H. Y. Wei, W. Sarney, L. Salamanca-Riba, and B. J. Fitzpatrick, accepted for publication, J. Cryst. Growth (2000)
- **P-type Doping of (Zn,Mg,Cd)Se Alloys Using an rf-discharge Nitrogen Plasma Source,** W. Lin, S. P. Guo, and M. C. Tamargo,

Reproduced with permission of the copyright owner. Further reproduction prohibited without permission.

accepted for publication, J. Vac. Sci. Technol. (2000)

- **MBE growth and p-type Doping of Hexagonal ZnSe Layers and ZnCdSe/ZnSe QW Structures on Hexagonal (Zn,Mg)(S,Se) Bulk Substrates**, W. Lin, M. C. Tamargo, H. Y. Wei, W. Sarney, L. Salamanca-Riba, and B. J. Fitzpatrick, accepted for publication, J. Vac. Sci. Technol. (2000)
- **Enhancement of p-type Doping of ZnSe Using a Modified (N+Te)δ-doping Technique**, W. Lin, S. P. Guo, M. C. Tamargo, I. Kuskovsky, C. Tian, and G. F. Neumark, accepted for publication, Appl. Phys. Lett. (2000)
- **In-situ Device Processing Using Shadow Mask Selective Area Epitaxy and In Situ Metallization**, Y. Luo, L. Zeng, W. Lin, B. Yang, M.C. Tamargo, Y. M. Strzhemechny, and S. A. Schwarz, submitted to Semicond. Sci. and Technol.

Conference Presentations

- **p-type Doping of ZnCdMgSe using an rf discharge nitrogen source**, the 18th North American Conference on Molecular Beam Epitaxy, Banff,

Reproduced with permission of the copyright owner. Further reproduction prohibited without permission.

Canada, 10-13 October 1999

- **MBE growth of hexagonal ZnSe on novel II-V hexagonal ZnMgSSe substrates**, the 18th North American Conference on Molecular Beam Epitaxy, Banff, Canada, 10-13 October 1999
- **Growth and p-type doping of Zn(Se,Te) Alloys Grown on InP substrates**, the Centennial March Meeting of American Physics Society, Atlanta GA, 21-26 March 1999.
- **Growth of hexagonal ZnSe epilayer and ZnCdSe/ZnSe QW structure on hexagonal (Zn,Mg)(S,Se) bulk substrates**, the 40th Electrical Materials Conference, Charlottesville VA, June 24-26, 1998. *(full scholarship award)*

Reproduced with permission of the copyright owner. Further reproduction prohibited without permission.

References

Chapter 1

1. S. Nakamura, M. Senoh, S. –I. Nagahama, N. Iwasa, T. Yamada, T. Matsushita, Y. Sugimoto and H. Kiyoku, Appl. Phys. Lett. **70**, 1417 (1997)
2. S. Taniguchi, T. Hino, S. Itoh, K. Nakano, N. Nakayama, A. Ishibashi and M. Ikeda, Electron. Lett. **32**, 552 (1996); M. A. Haase, J. Qiu, J. M. DePuydt and H. Cheng, Appl. Phys. Lett. **59**, 1272 (1991).
3. K. Koga and T. Yamaguchi, Prog. Cryst. Growth Charact. **23**, 127 (1991)
4. G. C. Hua, N. Otsuka, D.C. Grillo, Y. Fan, J. Han, M. D. Ringle, R. L. Gunshor, M. Nurmikko and A. V. Nurmikko, Appl. Phys. Lett. **65**, 1331 (1994).
5. Yongming Guo, Gregory Aizin, Y. C. Chen, L. Zeng and M. C. Tamargo, Appl. Phys. Lett. **70**, 1351 (1997).
6. A.Cavus, L. Zeng and M. C. Tamargo, Appl. Phys. Lett. **68**, 3446 (1996).
7. L. Zeng, B.X. Yang, B. Shewareged and M. C. Tamargo, J. Appl. Phys. **82**, 3306 (1997).
8. R. Bhargava, "Properties of Wide Bandgap II-VI Semiconductors", IEE EMIS Datareviews Series No.17 (1998) and references therein
9. L. L. Chao, H. Xing, G. S. Cargill III, L. Zeng and M. C. Tamargo,

Reproduced with permission of the copyright owner. Further reproduction prohibited without permission.

Bulletin of the American Physical Society V. 43 No. 1, 718 (1998). [APS March Meeting , Los Angeles, CA March 16-20 (1998)]

Chapter 2

1. A. Y. Cho, "Molecular Beam Epitaxy", AIP Press, New York (1994); M. A. Herman and H. Sitter, "Molecular Beam Epitaxy, Fundamentals and Current Status", 2nd Edition, Springer, New York (1996); T. Yao, Chapter 10 of "The Technology and Physics of Molecular Beam Epitaxy", edited by E. H. C. Parker, Plenum Press, New York (1987) and references therein
2. A. Y. Cho, J. R. Arthur, Prog. Solid State Chem. **10**, 157 (1975)
3. A. Cavus, L. Zeng, B. X. Yang, N. Dai, M. C. Tamargo, N. Bambha, F. Semendy, J. Cryst. Growth **175/176**, 558 (1997); L. Zeng, A. Cavus, B. X. Yang, M. C. Tamargo, N. Bambha, A. Gray, F. Semendy, J. Cryst. Growth **175/176**, 541 (1997)
4. L. Zeng, B. X. Yang, A. Cavus, W. Lin, Y. Y. Luo, M. C. Tamargo, Y. Guo and Y. C. Chen, Appl. Phys. Lett. **72**, 3136 (1998)
5. L. Zeng, S. P. Guo, Y. Y. Luo, W. Lin, M. C. Tamargo, H. Xing and G. S. Cargill III, J. Vac. Sci. Technol. **B 17(3)**, 1255 (1999)
6. A. N. Wright and C. A. Winkler, "Active Nitrogen", Academic, New York (1968)

Reproduced with permission of the copyright owner. Further reproduction prohibited without permission.

7. R. M. Park, J. Vac. Sci. Technol. A **10**, 701 (1992)

8. W.E. Hoke, P.J. Lemomias and D.G. Weir, J. Cryst. Growth **111**, 1024 (1991)

9. S. M. Sze, "Physics of Semiconductor Devices", 2nd Edition, John Wiley & Sons, New York (1981)

10. D. K. Schroder, "Semiconductor Material and Device Characterization", John Wiley & Sons, New York (1990); L. J. van der Pauw, Phil. Res. Rep. **13**, 1 (1958); L. J. van der Pauw, Phil. Tech. Rev. **20**, 220 (1958).

11. T. Marshall and D. A. Cammack, J. Appl. Phys. **69**, 4149 (1991); P. M. Mensz, S. Herko, K. W. Haberern, J. Gaines and C. Ponzoni, Appl. Phys. Lett. **63**, 2800 (1993).

12. J. S. Blakemore, "Semiconductor Statistics", Dover Publications, New York (1987)

13. T. Marshall, S. Colak and D. A. Cammack J. Appl. Phys. **66**, 1753 (1989)

14. S. Y. Wang, J. Simpson, K, A. Prior and B. C. Cavenett, J. Appl. Phys. **72**, 5311 (1992)

15. B. L. Sharma, "Metal-Semiconductor Schottky Barrier Junctions and Their Applications", Plenum Press, New York (1984)

Reproduced with permission of the copyright owner. Further reproduction prohibited without permission.

Chapter 3

1. Z. Zhu, K. Takebayashi and T. Yao, Jan. J. Appl. Phys. **32**, 654 (1993).

2. A. Cavus, L. Zeng, B. X. Yang, N. Dai, M. C. Tamargo, N. Bambha and F. Semendy, J. Cryst. Growth **175/176**, 558 (1997).

3. L. Zeng, A. Cavus, B. X. Yang, M. C. Tamargo, N. Bambha, A. Gray and F. Semendy, J. Cryst. Growth **175/176**, 541 (1997). L. Zeng, B. X. Yang, M. C. Tamargo, E. Snoeks and L. Zhao, Appl. Phys. Lett. **72**, 1317 (1998)

4. K. Ohkawa, T. Mitsuyu and O. Yamazaki, J. Appl. Phys. **62**, 3216 (1987).

5. S. O. Ferreira and H. Sitter, Appl. Phys. Lett. **66**, 1518 (1995).

6. G. F. Neumark, Phys. Rev. Lett. **62**, 1800 (1989).

7. Y. Mairfaing, Prog. Cryst. Growth Charact. **4**, 317 (1981).

8. S. Y. Ren, J. D. Dow and J. Shen, Phys. Rev. **B 38**, 10 677 (1988).

9. S. O. Ferreira, H. Sitter, W. Faschinger, R. Krump and G. Brunthaler, J. Cryst. Growth **146**, 418 (1995).

10. R. M. Park, M. B. Troffer, C. M. Rouleau, J. M. DePuydt and M. A. Haase, Appl. Phys. Lett. **57**, 2127 (1990)

11. I. W. Tao, M. Jurkovic and W. I. Wang, Appl. Phys. Lett. **64**, 1848 (1994)

12. J. Qiu, J. M. Depuydt, H. Cheng and M. A. Haase, Appl. Phys. Lett. **59**, 2992 (1991)

Reproduced with permission of the copyright owner. Further reproduction prohibited without permission.

13. W. Faschinger, S. Ferreira and H. Sitter, Appl. Phys. Lett. **66**, 2516 (1995)

14. H. Okuyama, Y. Kishita, T. Miyajima, A. Ishibashi and K. Akimoto, Appl. Phys. Lett. **64**, 904 (1994)

15. D. J. Chadi and K. J. Chang, Appl. Phys. Lett. **55**, 575 (1989)

16. T. Yao, Z. Zhu. Y. H. Wu, C. D. Song, F. Nishiyama, K. Kimura, H. Kajiyama, S. Miwa and T. Yahuda, J. Cryst. Growth **159**, 214 (1996)

17. G. Mandel, Phys. Rev. **134**, A1073 (1964)

18. D. B. Laks, C.G. Van de Walle, G. F. Neumark, P. E. Blochl and S. T. Pantelides, Phys. Rev. B **45**, 10965 (1992)

19. I. S. Hauksson, J. Simpson, S. Y. Wang, K. A. Prior and B. C. Cavenett, Appl. Phys. Lett. **61**, 2208 (1992)

20. A. Garcia and J. E. Northrup, Phys. Rev. Lett. **74**, 1131 (1995)

21. T. Baron, K. Saminadayar and N. Magnea, Appl. Phys. Lett. **67**, 2972 (1995)

22. D. J. Chadi and N. Troullier, Physica B **185**, 128 (1993)

23. T. Yao, T. Matsumoto, S. Sasaki, C. K. Chung, Z. Zhu and F. Nishiyama, J. Cryst. Growth **138**, 290 (1994)

24. B. H. Cheong, C. H. Park and K. J. Chang, Phys. Rev. B **51**, 10610

25. D. J. Chadi, Appl. Phys. Lett. **59**, 3589 (1991)

Reproduced with permission of the copyright owner. Further reproduction prohibited without permission.

26. C. H. Park and D. J. Chadi, Phys. Rev. Lett. **75**, 1134 (1995)

27. D. B. Laks, C. G. Van de Walle, G. F. Neumark and S. T. Pantelides, Appl. Phys. Lett. **63**, 1375 (1993)

28. Z. Zhu, G. Horsburg, P. J. Thompson, G. D. Brownlie, S. Y. Wang, K. A. Prior and B. C. Cavenett, Appl. Phys. Lett. **67**, 3927 (1995)

29. K. W. Kwak, R. D. King-Smith and S. Vanderbilt, Phys. Rev. B **48**, 17827 (1993)

30. D. J. Chadi and K. J. Chang, Phys. Rev. Lett. **61**, 873 (1988)

31. W. Walukiewicz, Appl. Phys. Lett. **54**, 2094 (1989)

32. P. J. Dean, W. Stutius, G. F. Neumark, B. J. Fitzpatrick and R. N. Bhargava, Phys. Rev. B **27**, 2419 (1983)

33. R. M. Park, M. B. Troffer, C. M. Rouleau, J. M. DePuydt and M. A. Haase, Appl. Phys. Lett. **57**, 2127 (1990)

34. Z. Zhu, G. D. Brownlie, G. Horsburgh, P. J. Thompson, S. Y. Wang, K. A. Prior and B. C. Cavenett, Appl. Phys. Lett. **67**, 2167 (1995)

35. Z. Zhu, K. Takebayashi, K. Tanaka, T. Ebisutani, J. Kawamata and T. Yao, Appl. Phys. Lett. **64**, 91 (1994)

36. S. Matsumoto, H. Tosaka, T. Yosida, M. Kobayashi and A. Yoshikawa, Jpn. J. Appl. Phys. **32**, L229 (1993)

37. C. E. C. Wood, G. Metze, J.Berry and L. F. Eastman, J. Appl. Phys. **51**,

Reproduced with permission of the copyright owner. Further reproduction prohibited without permission.

383 (1980)

38. K. Ploog, J. Cryst. Growth **81**, 304 (1987)

39. J. L. deMiguel, S. M. Shibli, M. C. Tamargo and B. J. Skromme, Appl. Phys. Lett. **53** 2065 (1988)

40. Y. Fan , J. Han , L. He, R. L. Gunshor, M. S. Brandt, J. Walker, N. M. Johnson and A. V. Nurmikko, Appl. Phys. Lett. **65**, 1001 (1994)

41. W. Lin, B. X. Yang, S. P. Guo, A. Elmoumni, F. Fernandez and M. C. Tamargo, Appl. Phys. Lett. **75**, 2608 (1999)

42. W. Faschinger, S. Ferreira and H. Sitter, Appl. Phys. Lett. **64**, 2682 (1994)

43. Secondary Ion Mass Spectroscopy (SIMS) was performed by Prof. Schwartz's group at Queens College using the Time-of-Flight (TOF) technique.

44. T. Yao, M. Kato, J. J. Davies and H. Tanino, J. Cryst. Growth **86**, 552 (1988)

45. S. O. Ferreira, H. Sitter, W. Faschinger, R. Krump and G. Brunthaler, J. Cryst. Growth **146**, 418 (1995)

46. Y. Fan, J. Han, L. He, J. Saraie, R. L. Gunshor, M. Hagerott, H. Jeon, A. V. Nurmikko, G. C. Hua and N. Otsuka, Appl. Phys. Lett. **61**, 3160 (1992)

47. H. D. Jung, C. D. Song, S. Q. Wang, K. Arai, Y. H. Wu, Z. Zhu and T.

Reproduced with permission of the copyright owner. Further reproduction prohibited without permission.

Yao, Appl. Phys. Lett. **70**, 1143 (1997)

48. D. J. Chadi, Phys. Rev. Lett. **72**, 534 (1994)

49. T. Ohtsuka, J. Kawamata, Z. Zhu and T. Yao, Appl. Phys. Lett. **65**, 466 (1994)

50. P. M. Mensz, S. Herko, K. W. Haberern, J. Gaines and C. Ponzoni, Appl. Phys. Lett. **63**, 2800 (1993)

51. M. Shur, "Physics of Semiconductor Devices", Prentice Hall, Englewood Cliffs (NJ) (1990)

52. O. Madelung, "Physics of III-V Compounds", John Wiley & Sons, New York (1964)

Chapter 4

1. D. J. Chadi, Phys. Rev. Lett. **72**, 534 (1994)

2. W. Faschinger, S. Ferreira and H. Sitter, Appl. Phys. Lett. **64**, 2682 (1994)

3. L. Zeng, B. X. Yang, A. Cavus, W. Lin, Y. Y. Luo M. C. Tamargo, Y. Guo and Y. C. Chen, Appl. Phys. Lett. **72**, 3136 (1998)

4. F. S. Turco-Sandroff, R. E. Nahory, M. J. S. P. Brasil, R. J. Martin, R. Beserman, L. A. Farrow, J. M. Worlock and A. L. Weaver, J. Crystal Growth **111**, 762 (1991)

5. K. Naniwae, H. Iwata, N. Kuroda, K. Yashiki, M. Kuramoto, A. Gomyo

Reproduced with permission of the copyright owner. Further reproduction prohibited without permission.

and T. Suzuki, Proc. of the 1st Intern. Symp. on Blue Lasers and Light Emitting Diodes, Chiba, Japan (1996)

6. M. J. S. P. Brasil, R. E. Nahory, F. S. Turco-Sandroff, H. L. Gilchrist and R. J. Martin, Appl. Phys. Lett. **58**, 2509 (1991)
7. M. J. S. P. Brasil, M. C. Tamargo, R. E. Nahory, H. L. Gilchrist and R. J. Martin, Appl. Phys. Lett. **59**, 1206 (1991)
8. T. Yao, M. Kato, J. J. Davies and H. Tanino, J. Cryst. Growth **86**, 552 (1988)
9. D. Lee, A. Mysyrowicz, A. V. Nurmikko and B. J. Fitzpatrick, Phys. Rev. Lett. **58**, 1475 (1987)
10. G. F. Neumark, Phys. Rev. Lett. **62**, 1800 (1989)
11. I. W. Tao, M. Jurkovic and W. I. Wang, Appl. Phys. Lett. **64**, 1848 (1994)
12. M. C. Tamargo, W. Lin, S. P. Guo, Y. Y. Luo, Y. Guo and Y. C. Chen, accepted for publication, J. Cryst. Growth (2000)
13. S. –H. Wei and A. Zunger, J. Appl. Phys. **78**, 3846 (1995)
14. W. Faschinger, S. Ferreira and H. Sitter, Appl. Phys. Lett. **66**, 2516 (1995)
15. T. Yao, Y. Makita and S. Maekawa, J. Crystal Growth **45**, 309 (1978)

Reproduced with permission of the copyright owner. Further reproduction prohibited without permission.

Chapter 5

1. L. Zeng, B. X. Yang, A. Cavus, W. Lin, Y. Y. Luo, M. C. Tamargo, Y. Guo and Y. C. Chen, Appl. Phys. Lett. **72**, 3136 (1998)

2. L. Zeng, S. P. Guo, Y. Y. Luo, W. Lin, M. C. Tamargo, H. Xing and G. S. Cargill III, J. Vac. Sci. Technol. B **17**, 1255 (1999)

3. W. Xie, D. C. Grillo, R. L. Gunshor, M. Kobayashi, G. C. Hua, N. Otsuka, H. Jeon, J. Ding and A. V. Nurmikko, Appl. Phys. Lett. **60**, 463 (1992)

4. D. B. Eason, Z. Yu, C. Boney, J. Ren, L. E. Churchill, J. W. Cook, Jr., J. F. Schetzina and N. A. El-Masry, J. Cryst. Growth **138**, 703 (1994)

5. B. J. Wu, L. H. Kuo, J. M. DePuydt, G. M. Haugen, M. A. Haase and L. Salamanca-Riba, Appl. Phys. Lett. **68**, 379 (1996)

6. S. Nakamura, J. Cryst. Growth **145**, 911 (1994)

7. M. Bremser, H. Protzmann, B. Wachtendorf, O. Schoen, M. Schwambera, B. Schineller, M. Heuken, E. Woelk, D. Schmitz and H. Juergensen, Proc. of the 2nd Intern. Symp. on Blue Lasers and Light Emitting Diodes, Chiba, Japan 449 (1998)

8. M. J. S. P. Brasil, R. E. Nahory, F. S. Turco-Sandroff, H. L. Gilchrist and R. J. Martin, Appl. Phys. Lett. **59**, 1206 (1991)

9. S. O. Ferreira, H. Sitter, W. Faschinger, R. Krump and G. Brunthaler, J. Cryst. Growth **146**, 418 (1995)

Reproduced with permission of the copyright owner. Further reproduction prohibited without permission.

10. Y. Luo, A. Cavus, M. C. Tamargo, J. Wan and F. H. Pollak, J. Vac. Sci. Technol. **B16**, 1312 (1998)

Chapter 6

1. B. J. Wu, G. M. Haugen, J. M. DePuydt, L. H. Kuo and L. Salamanca-Riba, Appl. Phys. Lett. **68**, 2828 (1996)
2. B. J. Fitzpatrick, Proceedings of the NATO Advanced Research Workshop on the Growth and Optical Properties of Wide-gap Low Dimensional Semiconductors, Regensburg, Germany, Aug. 2-5, 1988. T.C. McGill et al., eds, Plenum, New York (1989), p.67.
3. Cleveland Crystals, commercial literature.
4. B.J. Fitzpatrick, J. Khurgin, P.M. Harnack and D. deLeeuw, Proceedings of the International Electron Devices Meeting, Los Angeles, Dec. 7-10, 1986, p.630.
5. B.J. Fitzpatrick, U.S. Patent #5, 521, 934, May 28, 1996; B.J. Fitzpatrick, ibid., #5, 394, 422, Feb. 28, 1995; B.J. Fitzpatrick, ibid., #5 260, 958, Nov. 9, 1993. These patents only discuss the lattice matching composition (Zn,Mg)(S,Se); an explanation of the hexagonal concept is given in "Growth and Characterization of Hexagonal (Zn,Mg)(S,Se) Bulk Substrates", W. Lin et al, accepted for publication, J. Cryst.

Reproduced with permission of the copyright owner. Further reproduction prohibited without permission.

Growth (2000).

6. B. J. Fitzpatrick, in "Properties of Wide Bandgap II-VI Semiconductors", EMIS Datareview No. 16, R. Bhargava, ed., IEE: INSPEC, London, 1997, p.65.
7. K. Kondo, M. Ukita, H. Yoshida, Y. Kishita, H. Okuyama, S. Itoh, T. Ohata, K. Nakano and A. Ishibashi, J. Appl. Phys. **76**, 2621 (1994)
8. A. S. Nasibov, P. V. Shapkin, J. V. Korostelin, J. A. Vlasov, L. S. Markov, A. I. Maslov and D. L. Federov, Solid State Comm. **78**, 521 (1991)
9. F. Firszt, H. Meczynska, B. Sekulska, J. Szatkowski, W. Paszkowicz and J. Kachniarz, Semicond. Sci. Technol. **10**, 197 (1995)
10. S. -A. Park, H. -J. Song, W. -T. Kim, H. -G. Kim, M. -S. Jin, C. -D. Kim and C. -S. Yoon, J. Appl. Phys. **83**, 3429 (1998)
11. H. Mittendorf, Z. Physik. **183**, 113 (1965)
12. The original calculations and experimental work were done while one of us (B. J. F.) was at Philips Laboratories, before 1990. After the publication of the work of Okuyama et al[13], Philips applied for and received the patents listed in Ref. 5, since U.S. patent law gives precedence to the first to invent, rather than the first to file or publish. Okuyama's reasoning was derived from the use of Pauling's values for

Reproduced with permission of the copyright owner. Further reproduction prohibited without permission.

the tetrahedral covalent radii; their empirical work was done by MBE on GaAs substrates. Values calculated from their data were fairly similar, but they have used a larger amount of S than Mg and we have used an Mg:S ratio of 26:19. Of course, this was used in order to match the lattice constant of ZnSe, not GaAs.

13. H. Okuyama, K. Nakano, T. Miyajima and K. Akimoto, Jpn. J. Appl. Phys. **30,** L1620 (1991)

14. B. J. Fitzpatrick, T. F. McGee III and P.M. Harnack, J. Crystal Growth **78,** 242 (1986)

15. F. D. Bloss, "An Introduction to the Methods of Optical Crystallography", Holt, Rinehart and Winston, Inc., New York (1961)

16. B. J. Fitzpatrick, Proc. of the Society of Photo-optical Instrumentation Engineers (SPIE) **2436,** 192 (1994)

17. C. C. Chu, T. B. Ng, J. Han, G.C. Hua, R. L. Gunshor, E. Ho, E. L. Warlick, L. Kolodjiedski and A. V. Nurmikko, Appl. Phys. Lett. **69,** 602 (1996)

18. A. Kobayashi, O. F. Sankey and J. D. Dow, Phys. Rev. B **28,** 946 (1983)

19. C. Kothandaraman, G. F. Neumark and R. M. Park, Appl. Phys. Lett. **67,** 3307 (1995)

Reproduced with permission of the copyright owner. Further reproduction prohibited without permission.

20.P. Baume, J. Gutowski, D. Wiesmann, R. Heitz, A. Hoffmann, E. Kurtz, D. Hommel and G. Landwehr, Appl. Phys. Lett. **67**, 1914 (1995)

21.M. Moldovan, T. H. Myers and N. C. Giles, J. Appl. Phys. **84**, 5743 (1998)

22.T. Ohno, Y. Kawaguchi, A. Ohki and T. Matsuoka, Jpn. J. Appl. Phys. **33**, 5766 (1994)

23.W. I. Wang, E. E. Mendez, T. S. Kuan and L. Esaki, Appl. Phys. Lett. **47**, 826 (1985)

24.D. L. Miller and P. M. Asbeck, J. Crystal Growth **81**, 368 (1987)

25.S. M. Huang, Y. Nozue and K. Igaki, Jpn. J. Appl. Phys **22**, L420 (1983)

26.Y. Hishida, T. Toda, T. Yoshie, K. Yagi, T. Yamaguchi and T. Niina, App. Phys. Lett. **64**, 3419 (1994)

27.Private communications. The time-resolved PL measurements were performed by Dr. I. Kuskovsky at Columbia University.

Reproduced with permission of the copyright owner. Further reproduction prohibited without permission.